



TECHNISCHE
UNIVERSITÄT
WIEN

DISSERTATION

A holistic approach on real-time analysis of degradation at solid-liquid interfaces

ausgeführt zum Zwecke der Erlangung des akademischen Grades eines
Doktors der technischen Wissenschaften unter der Leitung von

Univ.Prof. Dipl.-Ing. Dr.techn. Markus Valtiner

und

Dr.rer.nat. Hsiu-Wei Cheng

Institut für Angewandte Physik, E134

eingereicht an der Technischen Universität Wien

Fakultät für Physik

von

Dominik Dworschak, MSc.

Matrikelnummer 11717688



Wien, Juni 2021

Ich erkläre an Eides statt, dass ich die vorliegende Dissertation selbstständig und ohne fremde Hilfe unter der Betreuung von Univ. Prof. Dipl.-Ing. Dr.techn. Markus Valtiner verfasst habe. Es wurden keine anderen als die angegebenen Quellen und Hilfsmittel benutzt bzw. die wörtlich oder sinngemäß entnommenen Stellen als solche kenntlich gemacht.

Wien, am 29.06.2021

Wir sollen heiter Raum um Raum durchschreiten,
An keinem wie an einer Heimat hängen,
Der Weltgeist will nicht fesseln uns und engen,
Er will uns Stuf´ um Stufe heben, weiten.

*Serenely let us move to distant places
And let no sentiments of home detain us.
The Cosmic Spirit seeks not to restrain us
But lifts us stage by stage to wider spaces.*

Hermann Hesse, "Stufen"

Contents

Table of contents	iii
Abstract	vi
Kurzfassung	viii
Glossary	x
Abbreviations	x
I Introduction	1
1 Motivation	2
2 Literature Overview on Methodology	8
2.1 Electrochemistry	8
2.2 Electrochemical Atomic Force Microscopy	10
2.2.1 Status Quo	12
2.2.2 Design of an Electrochemical Cell for Atomic Force Microscopes	13
2.3 Inductively Coupled Plasma Mass Spectrometry (ICP-MS) as a tool for stability studies on solid liquid interfaces	17
2.3.1 ICP methods for studies on the stability of solid liquid-interfaces	19
2.3.2 Electrochemical ICP-MS flow cell	23
2.4 Roadmap through Results and Discussion	25

II	Results and Discussion	27
3	Photocorrosion of ZnO Single Crystals during Electrochemical Water Splitting	28
3.1	Introduction - Stability of Zinc Oxide	30
3.2	Experimental section	32
3.3	Results	33
3.4	Discussion	37
3.5	Conclusion	41
4	Comparison of Elemental Resolved non-confined and restricted electrochemical degradation of Nickel Base Alloys	43
4.1	Introduction	44
4.2	Experimental Section	46
4.3	Results	49
4.3.1	Anodic polarisation and elemental resolved dissolution.	49
4.3.2	Repassivation.	51
4.3.3	Surface characterization - XPS.	54
4.3.4	Nano-XRF/SEM characterization of corroded areas.	56
4.4	Discussion and interpretation	57
4.4.1	Comparison of anodic corrosion and elemental dissolution under restricted and non-restricted conditions.	57
4.5	Conclusions	60
5	Stability and quality study of passive films formed on Alloy 600 with in-situ AFM and EC-ICP-MS	62
5.1	Introduction	63
5.2	Experimental Section	66
5.3	Results and Discussion	67
5.3.1	Results of ICP-MS experiments.	67
5.3.2	Results of <i>in situ</i> EC-AFM surface morphology probing	71
5.3.3	Overall discussion of results	74
5.4	Conclusions	76

6	Complementary electrochemical ICP-MS flow cell and in-situ AFM study of the anodic desorption of molecular adhesion promoters	78
6.1	Introduction	80
6.2	Experimental Section	81
6.3	Results and Discussion	82
6.4	Conclusions	88
7	Bottom-up Characterization of Metal-Metal Interaction from Simple Binary alloys to High Entropy Alloys	90
7.1	Introduction	91
7.2	Materials and Methods	93
7.3	Results	94
7.4	Discussion	98
7.5	Conclusion	106
8	Conclusion and Outlook	108
	Bibliography	113
	List of figures	140
	List of tables	142
	Copyright clearances	146
	Curriculum Vitae	149
	Appendices	A1
A.1	Electrochemistry of Zinc Oxide dissolution	A1
A.2	Comparison of non-confined and restricted electrochemical degradation of Nickel Base Alloys	A3
A.3	Anodic dissolution of equimolar alloys of the system (Ni-Co-Cr-Fe-Mn)	A10
A.4	In-situ AFM of SAMs on gold during anodic polarisation	A15

Abstract

Stability of electrified solid|liquid interfaces is decisive for a variety of electrochemical processes ranging from corrosion of structural materials to electrocatalysts. Electrochemical reactions, may they be desired as in catalysis or unintended as for corrosion inevitably lead to degradation of electrodes. Studying those interfaces during electrochemical processes is challenging for classical, vacuum-based methods of surface science.

In this thesis two complementary analytical methods are used to enable *in situ* tracking of the electrochemical processes taking place. Firstly, an electrochemical flow cell was developed, that, in combination with a downstream analysis with inductively coupled plasma mass spectrometry (ICP-MS), enables a time and elemental resolved analysis of material degradation. Analysis of degradation products indirectly give an indication about composition of the degraded surface. Further, a novel design of an electrochemical cell for atomic force microscopy (AFM) complements the knowledge gained with time-resolved topographies of an active electrochemical interface. Here local effects as roughening or delamination of the surface can be observed and therefore lead to a better understanding of the processes during dissolution.

The influence of o-rings on corrosion studies in flow cells is shown exemplary for the corrosion of nickel-based alloys. Further the electrochemical passivation and quality of the formed metal oxide layers on a series of metal alloys were studied in order to establish a material library to decipher the contributions of single alloying elements on the formation of a stable passive film. Also the flow cell was adapted for studying photo-induced corrosion of photoactive semiconductors like zinc oxide.

By this the variety of applications of the complementary methods of electrochemical ICP-MS flow cells and AFM for the investigation of electrified solid|liquid interfaces could be broadened. The developed analytical techniques supplement each other in their explanatory power and pave the way to gain complementary knowledge about fundamental processes on electrochemical active solid|liquid interfaces.

Kurzfassung

Die Stabilität von Fest|Flüssig-Grenzflächen unter Potentialkontrolle ist entscheidend für eine Vielzahl an elektrochemischen Prozessen von Korrosion von Konstruktionswerkstoffen bis hin zur Elektrokatalyse. Elektrochemische Reaktionen, ob erwünscht in der Katalyse oder ungewollt im Falle der Korrosion führen unweigerlich zur Degradierung der Elektroden. Die Untersuchung dieser Grenzflächen während elektrochemischen Prozessen ist eine Herausforderung für die klassischen vakuum-basierten Methoden der Oberflächenwissenschaften.

In vorliegender Dissertation werden zwei komplementäre analytische Methoden eingesetzt, die es ermöglichen *in situ* die ablaufenden elektrochemischen Prozesse zu verfolgen. Zunächst wurde eine elektrochemische Durchflusszelle entwickelt, die kombiniert mit nachgelagerter Detektion mittels Massenspektrometrie mit induktiv gekoppeltem Plasma (ICP-MS) eine elementar und zeitlich aufgelöste Analyse der Materialdegradation ermöglicht. Die Methode ist hochsensitiv Methode und kann, mit einer Auflösung weit unter einzelne Monolagen, Aufschluss bereits im Anfangsstadium der Degradation von Materialien geben. Die Analyse von Degradationsprodukten geben indirekt Aufschluss über die Beschaffenheit der degradierten Oberfläche. Weiters ergänzt eine neuartig designte elektrochemische Zelle für ein Rasterkraftmikroskop (AFM) die gewonnenen Erkenntnisse mit zeitaufgelösten Topographien von einer aktiven elektrochemischen Grenzfläche. Hier können lokale Effekte wie Aufrauung und Delamination der Oberfläche beobachtet werden und damit zu einem besseren Verständnis Prozesse bei der Auflösung führen.

Der Einfluss von O-Ringen auf Korrosionsuntersuchungen in Durchflusszellen wird

beispielhaft anhand der Korrosion von Nickel-basierten Legierungen gezeigt. Weiters wurden die elektrochemische Passivierung und Qualität der gebildeten Metalloxid-Schichten einer Serie von Legierungen untersucht zum Aufbau einer Materialdatenbank zur Entschlüsselung der Beiträge einzelner Legierungsanteile zum Aufbau einer stabilen Passivschicht. Ferner wurde die Durchflusszelle für die Untersuchung von photoinduzierter Korrosion adaptiert zur Untersuchung von photokatalytisch aktiven Halbleitern wie etwa Zinkoxid.

Damit konnte die Breite der Anwendungen für die sich ergänzenden Methoden von elektrochemischen ICP-MS-Flusszellen und AFM für die Untersuchung elektrochemischer Fest-Flüssig-Grenzflächen erweitert werden. Die entwickelten Analysemethoden ergänzen sich in ihrer Aussagekraft und ermöglichen somit komplementäre Erkenntnisse über fundamentale Prozesse an elektrochemisch aktive Fest|Flüssig-Grenzflächen.

Glossary

Abbreviations

AESEC	Atomic Emission Spectroelectrochemistry
AFM	Atomic Force Microscopy
BNC	Bayonet Neill–Concelman (connector for coaxial cable)
CE	Counter Electrode
CV	Cyclic Voltammetry
GDP	Gross Domestic Product
HEA	High Entropy Alloy
HER	Hydrogen evolution reaction
HPLC	High Performance Liquid Chromatography
ICP-MS	Inductively Coupled Plasma Mass Spectrometry
LED	Light Emitting Diode
LSV	Linear Sweep Voltammetry
NBA	Nickel-based Alloy
NPV	Normal Pulse Voltammetry
OER	Oxygen evolution reaction
ORR	Oxygen reduction reaction
PEEK	Polyether Ether Ketone
PTFE	Polytetrafluoroethylene
QCM-D	Quartz Crystal Microbalance with Dissipation
RE	Reference Electrode
SAM	Self-assembled Monolayer
SEM	Scanning Electron Microscopy
SFC	Scanning Flow Cell
SPM	Scanning Probe Microscopy
STM	Scanning Tunneling Microscopy
UV	Ultraviolet Radiation
WE	Working Electrode
XRF	X-Ray Fluorescence

Part I

Introduction

Chapter 1

Motivation

Solid|liquid interfaces Solid|liquid interfaces are ubiquitous on our planet, with more than 70% of the earth's surface being water-covered. Every droplet that comes in contact with a solid surface results in the formation of solid|liquid interfaces, that are important for a multiplicity of processes, such as crystallisation[1], biomineralisation, lubrication[2], wetting[3], condensation, and chemical reactions at interfaces[4].

Any formed solid|liquid interface will result in an equilibrium between the two condensed phases. Solid material will always to some extent dissolve into the covering liquid. Understanding these processes is crucial in the design of stable materials for a variety of applications. External influences like extra energy input by light irradiation or applied potential can significantly change the energy landscape of the surface.

Electrified solid|liquid interfaces Among those interfacial processes many include the transfer of electrons at the interface between solid and liquid which are then usually called electrode and electrolyte. These processes can be divided in two categories, depending on if electron flow occurs deliberately or unintendedly.

For the former case, desired electron transfers on solid-liquid interfaces include many technological important processes from electrocatalysis, electrochemical energy conversion and storage like batteries, but also electroplating and electropol-

ishing.

Conversely also undesirable processes like **material degradation** or **corrosion** take place. While they can be also triggered by high temperatures[5] most relevant corrosion processes are of electrochemical origin. Already traces of condensed water from a humid environment lead to the formation of a local electrochemical cell and can induce corrosion processes. Corrosion and material degradation occur also to some extent as a side effect with the previously mentioned desired processes on electrified solid-liquid interfaces.

Hence, **studying** and **understanding the stability of electrified solid-liquid interfaces** is of enormous interest. It is particularly relevant for several reasons:

Degradation of materials often coincides with severe **safety** risks. As examples one may consider structural materials like in buildings made of steel or steel enforced concrete, transportation ranging from boats to aerospace, chemical power plants or directly in biological systems like the human body as it is true for e.g. implants or pacemakers. All those structures rely on long-lasting mechanical and chemical stability, even in harsh environments.

Besides safety, material degradation also has an **ecologic impact**. Thinking of material release of potentially toxic chemicals to the environment, with subsequent uptake by water organisms. Further any degradation in a technological setting comes with the need of replacement that is related to energy consumption with its own harmful influence.

Ultimately material degradation is also of **economic interest**. Electrocatalyst are often made of very high-priced noble metals. Long-term stability of the catalyst material therefore is essential for economically meaningful operation of those processes. Stability of the material, also under application of an electric potential is therefore required for economically viable operation. Corrosion and other degradation processes in general causes enormous harm to the global economy. Its associated monetary loss is estimated to measure up to 3-4% of the global GDP (gross domestic product) per year.[6] Replacement of corroded/degraded materials is then also energy and resources consuming, and thus comes with an additional

environmental impact.

An understanding of the underlying mechanisms of material degradation hence is essential to consequently develop strategies to counteract corrosion/degradation by different choice of material, material development or coating technology. The used techniques, when applied, should be as close as possible to the processes that would happen under realistic conditions. Therefore, only *in situ* techniques are appropriate.

Techniques to probe stability of electrified solid|liquid interfaces Surface science in its early stages was fully restricted to solid|gas or even solid|vacuum systems. Most techniques even require high vacuum and are not suited to probe solid surfaces covered by a liquid (with the exception of liquids with very low vapor pressure like some molten salts and metals or ionic liquids).

Only *in situ* techniques can fully address a close observation of processes taking place at the solid-liquid interface in a broader sense, without major deviations from realistic conditions. In recent years some approaches have been made to extend classical surface science techniques that before were vacuum-bound. As an example X-ray photoelectron spectroscopy (XPS), just in recent years adapted to be used on solid|liquid interfaces with special experimental arrangements[7]. Still other *in situ* techniques have a much broader application range and less restrictions on the used systems. Aim of the present work was to employ surface sensitive techniques on electrified solid|liquid interfaces to gain information on their stability.

Electrochemistry Throughout this work **electrochemistry** is used to resemble processes like e.g. electrocatalysts under *operando* conditions or the local electrochemical cells that drive the material degradation by corrosion. The information density provided by electrochemistry alone though is for studying stability limited by the plurality of electrochemical processes that can occur beside material dissolution. To start electrochemical interface analysis in a broad sense, thus, two complementary *in situ* methods have been used. Both include electrochemical cells that are implemented into or connected with standard analytical devices:

1) Electrochemical Atomic Force Microscopy The initial stages of degradation are often very localized[8]. Hence it is essential to work with a method that provides a high spatial resolution. This can be achieved with electrochemical Atomic Force Microscopy (EC-AFM). Derived from the scanning tunneling microscope (STM) it is capable of probing both conductive and insulating materials. While already employed for a few decades[9–11], the used commercial cells often come with some drawbacks. We implemented a novel cell design with optimized current and potential distribution in an actual experimental setup. While Atomic Force Microscopy (AFM) is well suited to provide topographies, any chemical information is only very limited accessible[12]. Using EC-AFM for stability studies focusses on the solid phase of the solid|liquid interface. To access the solution side with the dissolved species, another technique needs to be used.

2) Electrochemical flow cell with downstream Inductively Coupled Plasma Mass Spectrometry (EFC-ICP-MS) Inductively Coupled Plasma Mass Spectrometry provides elementally resolved composition of liquid samples. While used predominantly as an *ex situ* technique to access material compositions, it has a vast potential for *in situ* applications[13, 14]. The combination of an electrochemical flow cell (EFC) with ICP-MS provides time and potential-resolved dissolution rates during all kind of electrochemical experiments. With its extremely low limit of detection below the parts per billion (ppb) range[15] it can resolve dissolutions of less than single monolayers.

Both approaches, also in combination, are well-suited to extend interface science into even more complex solid|liquid interfaces.

While already being employed in the corrosion and catalysis community, many material systems and applications of the mentioned methods are still unexplored. The aim of this work was to widen the application of the used techniques. Throughout the work we focused on aqueous systems and electrified solid|liquid interfaces.

The field of material degradation comprises a variety of scientific issues, as depicted in Figure 1.1. Those range from the influence of light irradiation, the composition and growth condition of passive films, protecting coatings and the influence of confinements and contact with neighbouring materials.

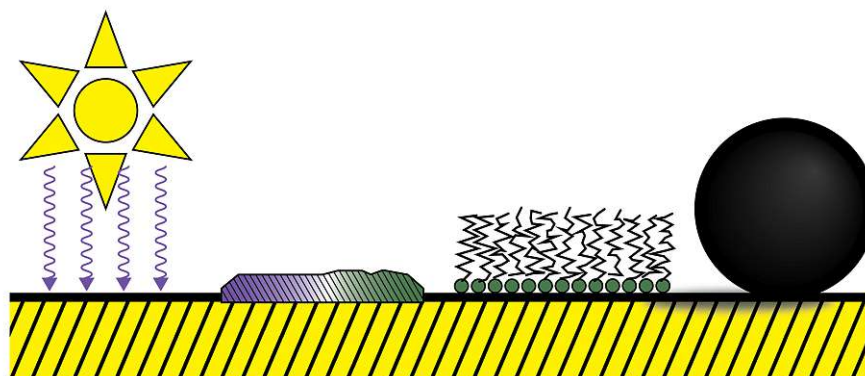


Figure 1.1: Stability-related processes at a solid/liquid interface. light irradiation, passive film formation, organic surface coating, crevice formation, Examples for processes on electrified solid/liquid interfaces

Research questions The aforementioned processes have been chosen as interesting topics to study regarding stability of solid/liquid interfaces. Investigation of those processes with the developed methods hence define the research questions we wanted to answer. The overarching motif of this whole work:

How to probe actively electrified solid/liquid interfaces in real time?

Given this motivation in the present work we aimed at answering the following specific research questions:

- Crevice corrosion is a problem for many technologically relevant materials as stainless steels, nickel based alloys, titanium and aluminium alloys[16]. Flow cells by default use O-rings for sealing and thereby create a crevice environment. What is its significance and how does the crevice that is formed under the O-ring change the stability of the material underneath?
- Since for sealing the flow it is somehow inevitable to use o-rings how can a severe effect of the crevice be counteracted?
- How can ICP-MS flow cell studies been applied to photoelectrocatalysts? It is well known that pH, applied potential and surface orientation influence stability of electrified solid/liquid interfaces. At the begin of this work the effect on the stability of semiconductors has not been studied by employ-

ing the proposed methods, in parallel the methodology was independently developed by other groups as well[17–20].

- So far the approaches are mainly applied to inorganic systems (metals, semiconductors). Can the methodology also be employed for investigating organic ultrathin corrosion inhibiting coatings like self-assembled monolayers on metal substrates?

The developed/further improved techniques expand the toolbox of interface science and complement the classical (*ex situ*) techniques of interface science.

This is accomplished by the novel design of **(1) an electrochemical cell for atomic force microscope** Further the design of **(2) a modular electrochemical flow cell with downstream elementally and time-resolved ICP-MS detection**.

Both setups are applied on their own and also complementary for a variety of systems of relevance in the field of corrosion and (photo)electrocatalysis.

Chapter 2

Literature Overview on Methodology

In this chapter the detailed strategies on how to study electrified solid|liquid interfaces by *in situ* methods will be discussed. In the scope of this work especially two techniques were used to investigate stability of electrified metals and oxides in aqueous electrolytes.

Electrochemistry is used throughout the present work in combination with Atomic Force Microscopy (AFM) and Inductively Coupled Plasma Mass Spectrometry (ICP-MS). The main purpose of electrochemistry hereby is to emulate conditions like in technological applications of electrocatalysis or resemble the local electrochemical cell during corrosion processes.

2.1 Electrochemistry

Electrochemistry covers all reactions involving the transfer of electrons. Thereby the uptake of an electron is called reduction, the counterreaction is oxidation:



The forward reaction with the release of electrons is called oxidation, the backward reaction is the reduction, the sites where these process occur in an electrochemical cell are called anode and cathode, respectively.

Electrochemistry itself is a very valuable tool to probe solid-liquid interfaces. Regarding stability the following chemical equation is the most fundamental one: Dissolution of a metal M to its ionic form is accompanied with the release of z electrons:



To retain charge neutrality in the electrochemical system, any accepted or received electron needs its respective counter-electron. Electrochemical cells thus always consist of two half reactions with anode and cathode. Throughout this work a three electrode setup is used. A potentiostat controls the potential difference between the working (WE) and the reference electrode (RE). The current is passing through the WE and the counter electrode (CE).

Regarding stability of electrified surfaces, a general overview can be gained by thermodynamic equilibrium diagrams, named after Marcel POURBAIX, who established them in the first half of the 20th century[21, 22].

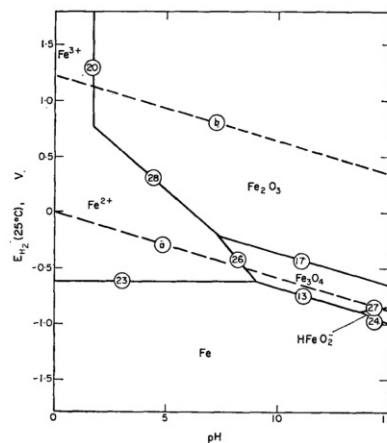


Figure 2.1: POURBAIX diagram of the system $Fe - H_2O$. Reprinted with permission from [23].

POURBAIX diagrams include, with a high information density, thermodynamic

data regarding stability of a given solid-electrolyte system. Analogous to phase diagrams of alloys, they show the thermodynamic most stable species of the pictured material system at a given potential and pH value. As shown in Fig. 2.1 exemplary on iron, its thermodynamically most stable form can be the elemental iron for lower potentials, metal oxides and also ionic species for higher potentials and low pH values. The concept of is mainly applied on simple material systems as pure metals in electrolytes containing maximum one anion species[24], since the variety of possible species is growing extensively with complexity. Still, the approach can also be applied for multi-component systems[25]. Deviations between POURBAIX diagrams and the observed behaviour can arise, besides of higher complexity of the real systems, from kinetics of the underlying reactions, which are not covered in the purely thermodynamic diagrams.

Electrochemists had, before the use of *in situ* techniques became common, to rely for surface characterization on *ex situ* techniques, usually requiring high vacuum, e.g. scanning electron microscopy (SEM), or electron diffraction methods. *In situ* spectroscopic techniques like using e.g. UV or IR detection provide just macroscopic view on the processes on the surface, due to the large analytic spot sizes. Especially for localized reactions this integral view might deviate from the often localized processes to be observed. Further, those are only possible if the specific observed material is interacting with the used wavelengths. Scanning probe techniques can provide both: Measurements *in situ* with the surface being actively polarized as well as very high spatial resolution down to the atomic level[26].

2.2 Electrochemical Atomic Force Microscopy

Since their development in the 1980s by BINNIG *et al.*[27–29] scanning probe microscopy (SPM) has propagated to all fields of surface and interface science[30]. Scanning tunneling microscopy (STM) as the avant-garde technique[27] is able to resolve surface morphology down to the atomic level. Its measurement principle is based on quantum tunnelling of electrons between sample and probe when a bias voltage is applied, which yields a measurable electric current. Therefore with STM only conducting or semiconducting surfaces are accessible. Originally developed

as a technique to be used in vacuum or ambient pressure environment it soon got extended to measurements in liquid. SONNENFELD and HANSMA[31] first successfully transferred the vacuum technique to aqueous systems and already suggested to extend the technique even further with electrochemistry. This then soon was accomplished[32], mostly on metal and graphite substrates[32–34]. Since then it is a standard method and widely applied [35–38]

A prerequisite for *in situ* STM is for the probe to be insulated for large parts since otherwise further faradaic reactions can occur there and interfere with the tunneling current. Also the electrochemical setup requires a bipotentiostat to have both the sample (WE) and the tip controlled relative to the reference electrode (RE)[39]. The limitation to conductive samples[40] led to the development of the atomic force microscopy (AFM)[28] based on a similar principle. Here the measurement method is, decoupled from any conductivity, the repulsive and attractive interaction between the probe and the sample. Interactions include repulsion forces, chemical binding forces, VAN DER WAALS- and electrostatic forces along with hydrophobic and hydrophilic interactions.

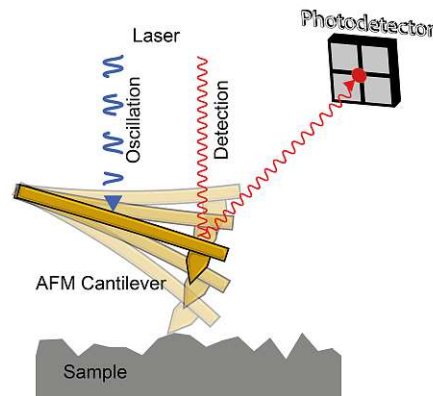


Figure 2.2: Principle of an AFM in tapping mode excited via a pulsed blue laser

The difference between AFM and STM is the principle used to measure the distance between sample and probe. While the threshold in STM is the tunneling current, AFM does not depend on an electric current, but rather the forces existing between sample and the cantilever. This is accomplished by tracking the deflection of a cantilever scanning over the surface. Detection is very sensitive by using a photodetector to track the position of a laser beam reflected from at back-side

of the AFM probe, as shown in **Fig. 2.2**. The schematic illustrates an AFM run in *tapping* or *intermittent contact* mode, where the probe is oscillated (here by thermally induced vibrations from a pulsed blue laser). The oscillation gets damped when the tip is in close proximity to the surface. This damping is measured by a decreased amplitude of the reflected red laser at the photodetector.

2.2.1 Status Quo

As for STM, also AFM was rapidly adapted to measurements in liquid[9]. To run electrochemical AFM (EC-AFM) the precautions are less demanding as for the scanning tunneling technique. First of all, both probe and sample can be insulating when measuring with AFM. An AFM probe usually is made of an inert material such as silicon or silicon nitride and does not undergo any electrochemical reactions. Further, the electrochemical setup can be rather simple with an external potentiostat and a classical three-electrode configuration, with the sample being the working electrode (WE), a bipotentiostat as for STM is not required. Electrochemical AFM was initially used mainly on metal substrates, one of the first works using the technique e.g. looked on the electrodeposition of copper on a gold electrode[41]. Soon this method got employed for many fields relevant to electrified solid|liquid interfaces. While most research was still conducted with the more common STM, AFM slowly found use for studying e.g. adsorption of ions[42], surface reconstructions[43] and corrosion of predominantly metals[10, 44, 45].

Application In corrosion science EC-AFM has become an important technique for complementary studies[46, 47]. Especially for localized phenomena like pitting and the initial stages of passive film formation and breakdown the technique EC-AFM has been proven useful to *in situ* look at actively corroding or passivating surfaces. The structural changes during the processes help to understand the corrosion mechanisms of metals in corrosive media. The advantage of high lateral resolution comes with the limitation of maximum scan size AFM of a few tens to hundreds of micrometers. While being in general a non-destructive technique the AFM tip can also be used to trigger material degradation with friction[48, 49].

Topics covered with EC-AFM span over the whole range of corrosion, from localized[50] and selective dissolution[51, 52], dealloying[53], pitting corrosion[48, 54], over characterisation of coatings[55, 56].

On a similar topic, still concerning stability of materials also catalysts and electrodes under *operando* conditions are accessible to *in situ* AFM. Catalyst stability is an essential property for an economically viable application. With EC-AFM processes like electrocatalytic aging and degradation in general are accessible *in situ*. The spatial resolution enables the observation of e.g. morphology changes[57] and gives hints on mechanical properties[58]. Applications range from metallic electrodes[59], over battery materials[60–62] up to fuel cells[63, 64].

2.2.2 Design of an Electrochemical Cell for Atomic Force Microscopes

Several designs were developed over the years to improve the performance of the electrochemical setup of *in situ* EC-AFM or adapt to the geometries of commercial AFMs. Since the detection principle of AFM relies on the reflected laser beam, it is impractical to have the used liquid openly exposed to the atmosphere. The refraction of the laser at the liquid|gas boundary would be very sensitive to any turbulences. Hence, the liquid usually is enclosed by a transparent window from the top, resulting in a stable optical path for the laser. As a side effect the total liquid volume in AFM cells is usually no bigger than a few mL, since it is restricted by the close distance between the electrochemically active sample and overlying glass window, so the liquid reservoir can be considered as a capillary in the few hundreds of microns wide gap between the two surfaces. This space constraint all designs have in common.

Significant improvements have been made in the last decades on the electrochemical cell designs used with AFM. Inertness of the used materials for the cell design had been already pointed out from the early stages on, so that even aggressive chemicals could be used as electrolyte[65]. The used materials and their chemical compatibility hence limit the chemicals that can be used.

Even if the importance of a large counter electrode has been pointed out from

the beginning[66], still in nowadays commercially available electrochemical cell designs often just a simple wire of gold or platinum is employed as a counter electrode[42, 53, 57, 67]. While being easy to handle, the use of a wire also comes with disadvantages. Especially for impedance spectroscopy it is well-known that geometry of the electrodes is significantly changing the obtained results[68, 69]. Moreover, especially for high currents the electrochemical reaction at the WE can be limited So that the limiting factor for the current through the cell is the WE, not determined by the Therefore a ring-shaped counter electrode has been designed by KRETA *et al.*[70] that also provides a more evenly distributed electric field distribution across the WE . A similar approach is suggested by VALTINER *et al.*[53] with the counter electrode surrounding the WE, while being on the same plane.

To summarize, the key features of an electrochemical cell for AFM should be the following:

- cleanability
- inertness of the used materials
- geometry of the electrodes
- reasonable type and placement of the reference electrode
- stability and usability
- good environmental control (no evaporation, temperature stability)

Nowadays most AFM manufacturer already offer electrochemical cells for their specific setups. Most of those are in their design very basic, and e.g. for the CE just a wire is placed into solution. Another major problem arises from the frequently used O-rings[46] that are used to limit spreading of the electrolyte next to the sample. The O-ring forms a confinement, in which the electrolyte is stagnant. Especially for corrosion research in this crevice like environment corrosive conditions emerge. As it gets addressed later (**Chapter 4**) crevices can significantly change the behaviour of the electrode.

In our cell design that is presented next, we try to avoid those downsides while

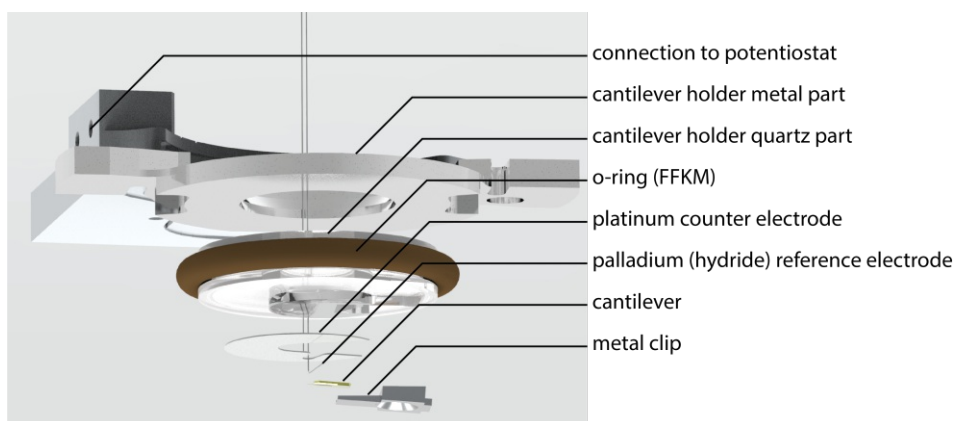


Figure 2.3: Rendering of the exploded view of a modified (perfusion) cantilever holder for electrochemical experiments. The palladium wire can be loaded with hydrogen to form a stable palladium hydride reference electrode of the second kind. Potential stability is poor in presence of dissolved oxygen ($\text{PdH} + 1/2\text{O}_2 \rightleftharpoons \text{Pd} + 1/2\text{H}_2\text{O}$), leaving with the possibility to use it as a quasi-RE or connecting from the outside a micro-RE via a capillary to the cell.

taking into account the previously mentioned key features.

Our Design also comes with some restrictions, but on the other side offers improvements compared to existing commercial versions. Also the aforementioned demands about desired properties of an electrochemical cell for AFM have been considered.

The used Cypher ES (Asylum Research/Oxford Instruments) provides a cell for measuring in liquids. That one is the foundation of the home-built design.

The AFM cantilever-holder itself is to the biggest part made of quartz with an excellent chemical resistance. The clamping mechanism for the cantilever consists of stainless steel holders. The AFM system used provides full control over environmental conditions. The cell when assembled is airtight and can be purged with gas so that e.g. humidity (for measurements in air) or oxygen levels can be concisely adjusted to the needs of the conducted experiment. Furthermore the sample is mounted on a holder capable to heat and cool, so that the temperature can be adjusted within the range of 0°C to 120°C . Since the potential applied on the electrode varies with time to synchronize the data the potential is read in as a separate channel in the AFM. This is accomplished by connection of the decoupled analog

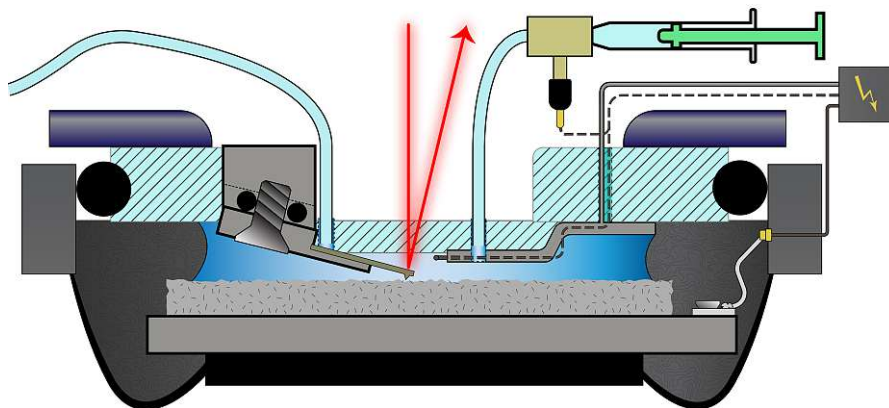
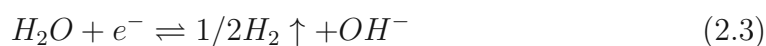


Figure 2.4: Cut section of the electrochemical AFM in operation. The working electrode is mounted on a magnetic disk to allow for automatic movement even in closed condition. Contact is made over a wire with magnetic connector to a feedthrough. Liquid is introduced/removed over one of the two through holes. The RE can be implemented in the connecting tube system or, alternatively the internal Palladium wire (dashed) can be used.

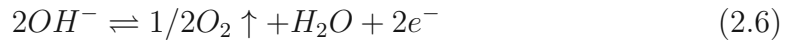
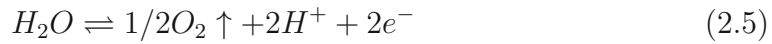
output into a free BNC port of the AFM controller. So every acquired topographic feature of the AFM picture is directly associated with the corresponding potential applied. Since the read-in suffered from a constant offset the recorded potential was corrected by a calibration function to compensate for that.

Usually in electrochemistry the reactions taking place at the counter electrode get neglected. In this particular geometry with the close distance between working and counter electrode it is essential to also consider counter reactions occurring there. Since the electrolytes used in this work are likely to be stable under electrochemical polarization as well as the used Pt is, that leaves the only electrolysis to happen. For high potentials on the working electrode (WE) the cathodic counter reaction is therefore the hydrogen evolution reaction (HER):



A negative potential on the WE results in the opposing reaction on the counter

electrode (CE), namely the oxygen evolution reaction (OER):



All of those reactions result in the formation of gases that 1) partially can adsorb and thereby block the CE or 2) even result in the evolution of gas bubbles. Since the distance between WE and CE is below a few hundred μm this needs to be avoided. With our optimized electrode geometry we accept this downside, since it can be easily balanced by increasing the ratio of the areas CE:WE by decreasing the active area of the WE, e.g. by embedding a cutout of material in a resin.

AFM only provides relative heights, so for degradation processes from topographies itself it is hard to estimate the total volume dissolved. Further, the technique by its high spatial resolution restricted to the small areas probed. Though, another *in situ* technique can help to identify the total dissolved mass both time- and element-resolved and will be presented next.

2.3 Inductively Coupled Plasma Mass Spectrometry (ICP-MS) as a tool for stability studies on solid|liquid interfaces

Mass Spectrometry is an analytical technique quantifying charged particles/ions depending on their mass-to-charge ratio. A very simplified mass spectrometer needs to consist of three parts: 1) the ion generation where the sample is ionized to yield charged particles 2) the mass filter, that is classifying the ions according their charge and 3) the detector to count the filtered ions. The free mean path of ions highly depends on the pressure they are moving at. With atmospheric pressure ions would collide with gas molecules present and immediately lose their charge to them. Therefore mass spectrometry necessarily relies on high vacuum conditions. This of course contradicts with probing a solid-liquid interface. ICP-systems therefore rely on an approach of differential pumping to bridge between

the ambient pressure of the sample and the high vacuum required by the mass spectrometer. An important step to take was the development of the nebulizer. With this approach enabling an easy sample introduction right from a flowing liquid. Pushing the electrolyte through a narrow nozzle a fine mist is produced. A fraction is then introduced into plasma torch where desolvation, evaporation, atomisation and ionisation take place at the high temperatures in the plasma (around 8.000 to 10.000 K)[15]. After passing the differentially pumped cones the ions are consequently electrostatically deflected, the ions are separated according their mass to charge ratio. Usually quadrupoles are used therefore.

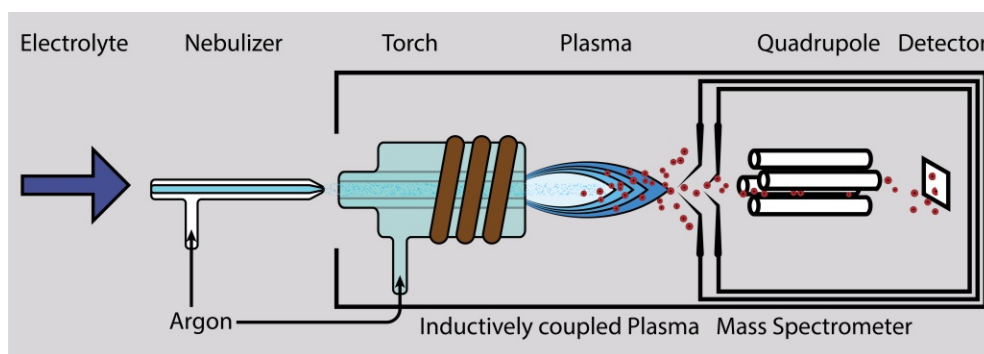


Figure 2.5: Schematic of inductively coupled plasma mass spectrometry with direct transition from electrolyte in ambient pressure to

Nearly all elements of the periodic table can be detected. Starting with light elements as lithium any element up to the heavy actinides are accessible. Since the detection principle bases on positively charged ions it is more applicable for elements with low electronegativity, so mainly metals. For most metals the detection limits of this technique reaches even below nanograms per liters, providing insights in sub-monolayers resolution. Furthermore detection is nearly linear within up to nine orders of magnitude[71]. Hence, it can cover dissolution processes ranging from e.g. growth of pits in micrometer range down below monolayer dissolution. All those advantages have led to a huge variety in applications, since devices got commercially available in the 1980s.

ICP-MS in general is nowadays a widely used standard analytical method for inorganic components in solution. Applications span from trivial water analysis[72], over petrochemical analysis[73] to medicine[74]. Most of those applications are now

standard analytical practice, the measured samples are stationary solutions.

In the last 20 years a growing research community extended the use of ICP-methods on time-resolved study of stability of solid|liquid interfaces which will be discussed in the following section.

2.3.1 ICP methods for studies on the stability of solid|liquid-interfaces

ICP based methods as ICP-MS and inductively coupled plasma optical emission spectroscopy (ICP-OES) are well suited to study stability of solid|liquid interfaces since they provide a time and elementally resolved signal of the solution side. Both ICP-MS and ICP-OES are used extensively for studies on corrosion and degradation of solids in contact with a liquid[13, 14].

As a side note, the principle of ICP-OES is similar to IPC-MS, though the detection principle is of optical nature and does not require a vacuum system. The concentration of the present ions are determined by analyzing the spectrum of the emitted light with a spectrometer. Therefore the system is less restricted regarding the used electrolyte, it can quite easily handle organic liquids as well as very high salt concentrations. On the other hand ICP-MS is more sensitive to very low concentrations, with an detection limit of about two orders of magnitude smaller.

Nevertheless both techniques are very suitable for stability studies of the solid|liquid interface. First applications of ICP-based techniques towards that direction have already been made in the early 80s to detect trace amounts of metals using ICP-OES by SNOOK *et al.*[75, 76]. An early spectrophotometer was used by BERGAMIN *et al.*[77] to quantify steel components that chemically dissolved by streaming liquids over it.

One of the first uses of ICP-MS on stability of metallic samples was conducted by CASTLE *et al.*[78, 79]. While treating metals in acidic solutions, samples were taken at different exposure times and consequently analyzed for dissolved metal species. Time-resolution with this very fundamental way of analysing corrosion

products was limited by the manual sampling frequency. With the evolution of the analytical technique and the availability of commercial devices soon more sophisticated applications in studying stability of surfaces followed.

Cell Designs and Applications Recent publications on the use of ICP-methods in combination with electrochemistry by research groups of OGLE[13], CHEREVKO and MAYRHOFER[14] provide a good summary on that topic. Those also cover considerations regarding the design of the used flow cells. Here just a short overview is given on the different approaches and applications.

Most electrochemical cells in use operate in a flow mode. An extensively used design with a stationary working electrode (WE) by the group of OGLE is shown in **Fig. 2.6**. It is referred to as atomic emission spectroelectrochemistry (AESEC). The electrolyte divides up to two compartments, one in contact with the WE and with the flowing electrolyte. The other compartment is separated by a membrane and hosts both the CE and the RE, making it very flexible towards used electrodes and their dimensions.

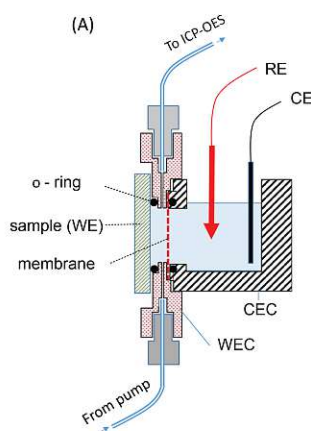


Figure 2.6: Schematic diagram of an electrochemical flow cell for AESEC measurements with the working electrode (WEC) and counter electrode compartment (CEC), modified after SHKIRKIY and OGLE[80] under CC-BY licence.

In this setup the WE is fixed by an O-ring and held in position during the experiment. This so called stationary flow cell type is limited in its spatial resolution. In contrast, the scanning flow cell (SFC) approach can provide localized information

as well. The group of HOMAZAVA[81–83] developed a micro-flow-capillary system for solution probing with ICP-MS with high spatial resolution. Based on a concept of HASSEL *et al.*[84] the design includes a capillary containing the corrosive media that can be scanned over different spots of the sample to locally probe the corrosion performance. The concept was then further improved and applied by OTT[85–87] and KLEMM[88–91].

Till date the developed methods have been employed on a large variety of solid|liquid interfaces. Applications here span from stability of *operando* catalysts to classical corrosion research. The developed methods have already dealt with a variety of material systems and topics related to stability and corrosion: Common steels and alloys[92–96] were as well as new material classes like high-entropy alloys (HEAs)[97, 98] covered. Also coatings and corrosion inhibitors are being tested by this technique[99, 100]. Another topic involves the field of energy materials, where the stability is essential for long-term operation electrocatalysts[101–107]. Just recently the method was further adapted to non-aqueous systems[105], which opens research to even broader fields of applications such as battery, capacitor and electrocatalytic materials used with organic or ionic liquids.

Data acquisition and treatment Data acquisition with ICP-MS yields time- and mass-resolved data of the recorded ions. The sensitivity, or factor between the real concentration in the electrolyte and the detected signal with ICP-MS, relies on a variety of parameters: First of all it depends on the first ionization energy of the single elements. The lower this energy is, the higher the likelihood of conversion of the respective atom into its onefold positively charged ion. Further the condition of the plasma and the composition and concentration of the electrolyte (matrix) and the dilution in the argon stream change which proportion of the analyte within the electrolyte arrives the detector in its ionic form. Therefore any element in need of quantification needs to be calibrated individually. Calibration involves the measurement of a dilution series of solutions with known analyte concentrations, preferentially in the expected concentration range of the latter dissolution experiment. To further adapt for changes of the sensitivity of the instrument, e.g. by alterations of the plasma, an internal standard is mixed with the test solution.

This is chosen according to the analytes to be measured and should have similar mass and ionization energy to be best comparable with the analytes. Calibration should give a linear relationship between the concentrations injected into the system and the resulting counts detected by the ICP-MS. The counts are recorded by integration over all arriving ions in a short period of time, usually a few hundreds of milliseconds. This results in a time dependent signal, namely *Counts per second*. The slope of a linear regression of the calibration is then used to convert the recorded data into a mass flow of analyte j in the electrolyte solution \dot{c}_j [$\frac{ng_{analyte}}{g_{solution}} \cdot \frac{1}{s}$]. This needs to be multiplied with the flow measured gravimetrically. About 99% of the electrolyte flowing through the cell end up at the waste container. Only the remaining fraction is introduced into the plasma torch. Therefore the collected waste is an appropriate estimate for the total electrolyte flow $\dot{m}_{solution}$ [g/s].

$$\dot{c}_j \cdot \dot{m}_{solution} = \dot{m}_j \quad (2.7)$$

In a simplified approach the application of the FARADAY law of electrolysis can be used to convert the dissolution currents \dot{m}_j of single elements j to an electrical current i and relate this to the recorded electrochemical signal:

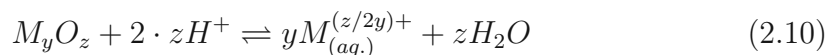
$$i_{m,j} = \frac{\dot{m}_j \cdot F \cdot \nu_j}{M_j} \quad (2.8)$$

F is the FARADAY constant, ν_j stands for the number of exchanged electrons according to equation (2.2) and M_j equals the molar mass of the analyte j . The total dissolution current is the sum of the single dissolution currents $i_{m,j}$.

$$i_m = \sum_{j=1}^n i_{m,j} \quad (2.9)$$

Thereby electrochemical and ICP-signals can be related to each other. Those calculations of course can only be considered as a rough estimate, since electrochemistry just provides information about the net exchanged electrons. Those can involve besides electrochemical dissolution as in equation (2.2) other side reactions. Some of those can not be directly tracked by the ICP-MS like e.g. gas evolution or passive film growth on the interface. Also charging currents are not resulting

in a with ICP methods detectable signal. Further, dissolution not involving any transfer of electrons is detected by mass spectrometry while not being recorded electrochemically. An example is the dissolution of oxides which does not involve a change of oxidation state of any species:



Still the information content of the method is very insightful. E.g. with a few assumptions the changes in surface composition can be tracked, while not being probed directly[108].

2.3.2 Design of the used Electrochemical Flow Cell

One main goal of this work was to modify the designs known from other working groups[92, 109] to specific needs. During the course of this work the cell design was constantly improved.

Big volumes included in the flow system would lead to a dilution of the analytes released from the WE, which in light of the small amounts might even make detection impossible. As **Fig. 2.7** shows for a theoretical experiment of a pulsed material release into a laminar flow. Undirected diffusion, as in any chromatographic method, leads to a broadening of the signal and a log-normal-like distribution of the detected signal, as shown in **Fig. 2.7**. To compensate for the broadening, a method for deconvolution of the recorded data has been suggested by the group of OGLE[80]. Not only the time resolution is negatively influenced, also increasing amounts of the dissolved species are, at the time of detection, dropping below the limit of detection of the ICP-MS. Hence the cell needs to be designed for a low internal volume to avoid extensive dilution of analytes, further the distance between cell and detection should be as short as possible to keep the broadening limited.

As base material for the ICP-MS flow cell (shown in **Fig. 2.8**) Polyether ether ketone (PEEK) was chosen for its excellent chemical resistance to almost all aqueous media as well as for its good machinability. A stamp of polytetrafluoroethylene (PTFE) introduced from the top leaves only small channels open for the elec-

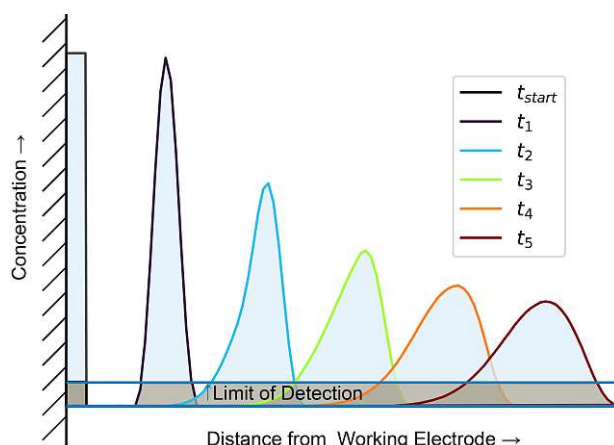


Figure 2.7: Effect of electrolyte volume between working electrode and detection in the ICP-MS on the time resolution of the method. Diffusion causes broadening of the signal with elapsing residence time in the tube system.

trolyte flow above the WE and leaves the internal volume restricted. Connectors were borrowed from standard HPLC-applications. These are designed for high chemical compatibility and low dead volume.

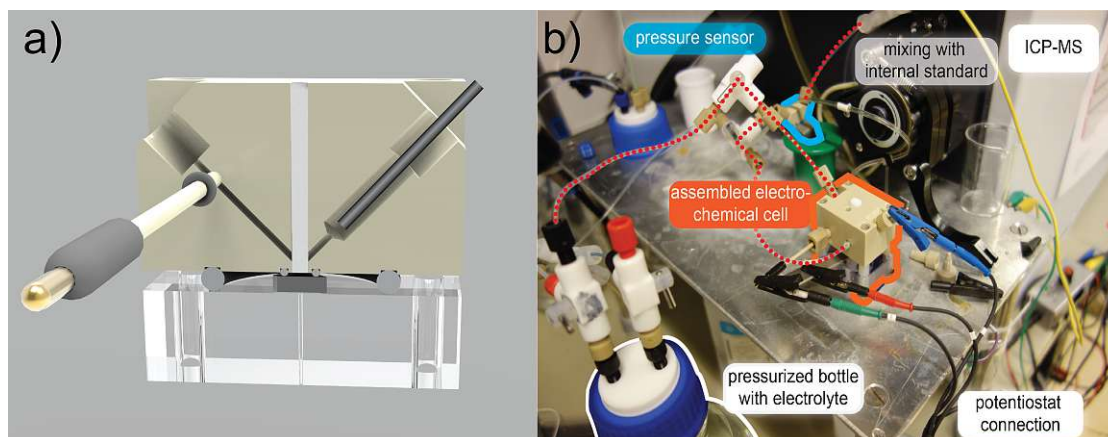


Figure 2.8: a) Cross section of the electrochemical flow cell used. Micro-reference electrode is introduced from the side of the inlet-channel, the counter electrode is in the stream of the outlet. The working electrode is clamped between the top and bottom part of the cell, sealed with an O-ring. b) Overall experimental setup with overpressure pumping system, electrochemical cell, potentiostat, pressure sensor and internal standard mixing. The red dotted line indicates the flow of the electrolyte.

The overall setup of a general setup is shown in **Fig. 2.8 b**. Pressurized air is used

to pump the electrolyte with a stable and pulsation-free laminar flow. The rate of flow was monitored by measuring with an in-flow pressure sensor and by weighing the collected waste electrolyte. The flow is set to 6 ± 0.4 mg of solution per second. Before each experiment the electrolyte was purged with compressed and filtered air for at least 30 minutes to guarantee the same concentration of dissolved oxygen. All electrochemical experiments were done using a Ag|AgCl-electrode as reference and presented data throughout this work is referenced to that potential. The used O-ring to seal the electrolyte flow between the flow cell body and the WE has an inner diameter of 3 mm and is made of inert EPDM (ethylene propylene diene monomer) or FKM (fluoro elastomer).

Measurements were performed using an Agilent 7900 ICP-MS (Agilent Technologies, US). The ICP-MS uses a collision cell with 5 mL/min flow of helium as cell gas. External calibration was performed with multi-element standard solutions provided by Agilent and Inorganic Ventures. Downstream of the electrochemical cell the analyte was mixed with internal standard solution, mostly cobalt is used (chapters 3,4,5), unless for the more heavy gold (chapter 6), where thallium was employed, for chapter 7 gallium is used, since cobalt is one of the analytes.

2.4 Roadmap through Results and Discussion

In the following chapters the developed electrochemical cells are used on different current issues concerning stability of the solid|liquid interface. The table below displays the key features and studied material system.

System	ICP-MS elements	AFM	specific feature
ZnO	Zn	pH-dependent	Photocorrosion
Nickel based Alloys (NBAs)	NiCrFeMo	-/-	Crevice corrosion
Nickel based Alloys (NBAs)	NiCrFe	<i>in situ</i> EC	Combination AFM&ICP
Au-SAM	Au	<i>in situ</i> EC	Interface/Adhesion
Binary to High Entropy Alloys (HEAs)	NiCrFeCoMn	-/-	Materials Library (Characterization)

Part II

Results and Discussion

Chapter 3

Photocorrosion of ZnO Single Crystals during Electrochemical Water Splitting

The following chapter is based on the article that appeared under the same title in ACS: Applied Materials & Interfaces (see [110]), reproduced under the corresponding copyright agreement. The concept of using a photoelectrochemical cell with down-stream degradation product analysis was at the time of the start of this work not established yet. In the interim that idea was realized by other working groups independently in parallel [17–20]. Working principle is to have not only the choice of electrolyte solution and potential applied to the working electrode but also the possibility to emit light onto the active surface.

Some of the shown ICP-MS measurements were conducted by Carina Brunnhofer in the course of a project work supervised by the author.

Degradation and dissolution of transparent semiconducting oxides is central to various areas, including designing of catalysts and catalysis conditions, as well as passivation of metal surfaces. In particular, photocorrosion can

be significant and plays a central role during photoelectrochemical activity of transparent semiconducting oxides. Here, we utilize an electrochemical flow cell combined with an inductively-coupled plasma mass spectrometer (ICP-MS) to enable the in-situ study of the time-resolved release of zinc into solution under simultaneous radiation of UV-light. With this system we study the dissolution of zinc oxide single crystals with (0001) and (10 $\bar{1}$ 0) orientations. At acidic and alkaline pH we characterized potential dependent dissolution rates into both the oxygen and the hydrogen evolving conditions. A significant influence of the UV radiation and the pH of the electrolyte was observed. The observed dissolution behaviour agrees well with the surface chemistry and stabilization mechanism of ZnO surfaces. In particular, polar ZnO(0001) shows ideal stability at low potentials and under hydrogen evolution conditions. Whereas ZnO(10 $\bar{1}$ 0) sustains higher dissolution rates, while it is inactive for water splitting. Our data demonstrates that surface design and fundamental understanding of surface chemistry provides an effective path to rendering electroactive surfaces stable under operating conditions.

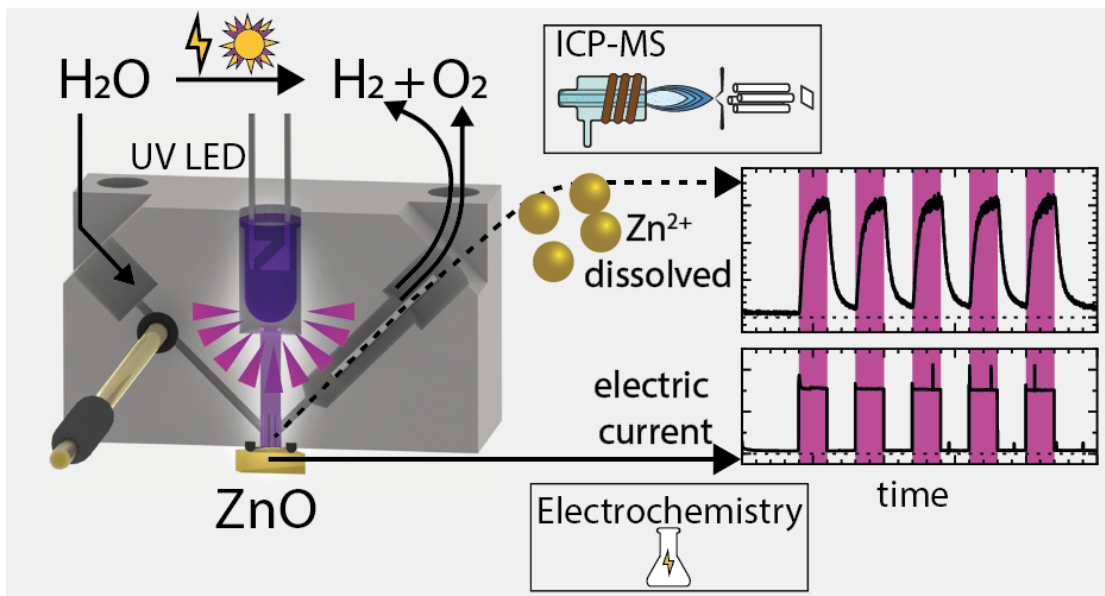
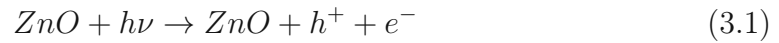


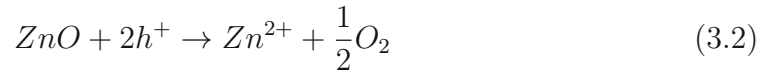
Figure 3.1: Studying Photocorrosion with an electrochemical flow cell with downstream ICP-MS detection

3.1 Introduction - Stability of Zinc Oxide

Degradation and dissolution of oxide materials plays a central role in the kinetics of degradation of structural as well as functional materials. For instance, in photo-electrochemical cells transparent semiconducting oxides create electron-hole pairs which can trigger electro-catalytic processes such as water splitting. Zinc oxide (ZnO) is considered as a promising material carrier as well as reactive material for water splitting and other catalytic processes.[111–113] With a bandgap of 3.3 eV[114] - close to the wavelength of visible light - ZnO can also effectively harvest energy from sunlight.[111, 115–120] Specifically, photon absorption can generate electron(e^-)/hole(h^+) pairs as follows:



These electron/hole pairs function as driving force for photocatalytic processes, however they also render ZnO prone to photocorrosion according to the following equation:



Yet, stability under catalytic/reactive conditions is of enormous importance for efficient catalytic action. Degradation of catalysts can render them useless within a few cycles during operation. In addition to photocatalytic stability, ZnO is a central protective oxide in the field of corrosion protection.[121] Sacrificial metallic zinc coatings are typically used as cathodic protection and the topmost layer is passivated, i.e. rendered stable by a ZnO layer.[122, 123]

Consequently, stability of ZnO has been studied in great detail under various conditions, and for various surface orientations such as the polar[124–131] and non-polar[129, 132], i.e. stoichiometric, surfaces.

The polar surfaces of ZnO are particularly interesting in terms of their stabilization mechanisms. Several experimental and theoretical studies showed that polar surfaces can stabilize by adsorption of OH and oxygen adatoms[124, 125, 127], as well as by formation of triangular reconstructions[128, 131] that realize a stabilizing

coverage by oxygen step-atoms.

The stability of nonpolar ZnO (*e.g.* $10\bar{1}0$) was not studied in great detail so far. High resolved atomic force microscopy imaging showed that dissolution of non-polar surfaces results in dissolution topographies that favour again the formation of polar surfaces. [129] Specifically, ZnO ($10\bar{1}0$) has been found to reconstruct under formation of stable ZnO (0001) and ($10\bar{1}\bar{1}$) surfaces.[129, 133] Further, some calculations identified point defects and oxygen vacancies as stabilizing features of these surfaces.[134, 135]

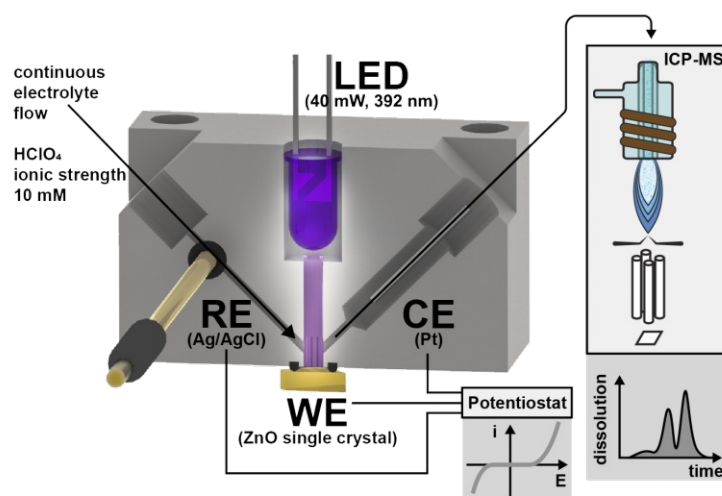


Figure 3.2: Schematic of the flow cell used. A quartz rod allows transmission of UV light. Overpressure pumping is used for establishing laminar flow across the working electrode. The reference electrode (Ag|AgCl) is placed up-stream and the counter electrode (Pt) is placed downstream to avoid contamination of Platinum at the WE. Standard HPLC fittings are used for all tubings.

In recent years there has been growing interest in stability of ZnO during photocatalysis. Here, indirect effects such as reduced photocatalytic activity [136–138] as an indicator for photocorrosion rather than dissolution were studied.

The aim of our work is to directly trace down the potential dependent stability of zinc oxide for various surface orientations particularly also during photocatalytic water splitting conditions by quantifying dissolving zinc in the electrolyte in real time.

Therefore, and as shown in **Fig. 3.2**, we use a photo-electrochemical flow cell with a subsequent downstream electrolyte analysis to determine the rate of degradation by inductively coupled plasma mass spectrometry (ICP-MS). With its very low (essentially monolayer sensitive) limit of detection ICP-MS is a powerful technique for time-resolved analysis of degradation products. Hence, a number of electrochemical ICP-MS flow cells have been developed for studying general metallic corrosion[13, 92]. Recently, this technique was adapted and tested for quantifying the photocorrosion of $BiVO_4$ [19] and WO_3 [17] as well as iridium oxide.[18]

As such electrochemical ICP-MS flow cells are well established for characterizing the stability of materials that are prone to corrosion under various conditions.

Here, we use this technique to tune reaction parameters as pH-value and applied potential regarding their influence on ZnO degradation rates. For the first time, we use this technique with oxide single crystals and we are able to connect ZnO surface orientation chemistry with observed stability and water splitting rates. Specifically, we study the photocatalytic stability of low-index ZnO surfaces (0001 and $10\bar{1}0$) in aqueous perchlorate solutions for both the oxygen evolution reaction (OER) and the hydrogen evolution reaction (HER). We show which surface is catalytically more active (higher water splitting current) and how stable the surfaces are under these conditions. The approach and the specific results offer a strategy for making ZnO most stable and reactive, or vice versa.

3.2 Experimental section

Chemicals and Materials. A 10 mM solution was prepared from sodium perchlorate (98+%, Alpha Aesar). pH was adjusted using sodium hydroxide (technical, VWR) and perchloric acid (p.a. grade, Carl Roth) while maintaining the concentration of the perchlorate anion constant. Milli-Q water (resistivity >18 M Ω ·cm, total organic carbon <4 ppb) was used for making electrolyte solutions. ZnO single crystals (MaTeck GmbH) of orientations (0001) and ($10\bar{1}0$) were prepared by hand polishing using diamond paste down to 0.05 μm

Inductively Coupled Plasma Mass Spectrometry (ICP-MS) Cobalt was used as internal standard, having a similar mass as zinc. A scheme of the setup is shown in **Figure 3.2**. The inhouse built electrochemical flow cell was made out of PTFE. The cell is illuminated by a UV LED (UV5TZ-390-15, Bivar, Inc.) shining through a quartz rod from the top on the active working electrode area. The illuminated area is at least 3.14 mm^2 (2mm diameter rod) neglecting any scattering of UV light. Total electrode area is about 7 mm^2 (3 mm diameter O-ring).

Atomic Force Microscopy (AFM) AFM topography (JPK) experiments were performed using contact mode cantilevers (Budget Sensor CONT). Using a custom-made cell for liquids of PEEK, electrolyte was exchanged with a syringe pump.

3.3 Results

The key question we want to address in this work is at which potential does ZnO degrade and how is this influenced by the surface chemistry, i.e. termination of the surface? In this work we hence focus on the nonpolar $(10\bar{1}0)$ and the polar zinc-terminated (0001) -Zn surfaces of ZnO, for which we already studied stabilization mechanism and surface chemistry extensively in our previous work. [124–127]

We designed a home-built UV-sensitized electrochemical flow-cell (see again **Fig. 3.2**) and combine this flow cell with a subsequent quantitative analysis of dissolved zinc in the electrolyte in an ICP-MS. Briefly, electrolyte solution is constantly fed through a standard three electrode electrochemical cell, where a ZnO single crystal acts as working electrode. UV light illuminates the surface from the top. Any dissolved zinc species are carried with the electrolyte flow towards detection in the ICP-MS. A detailed description of the cell is given in the experimental section and in previous work.[17–19]

Two different pH values, acidic at pH 5 and weakly alkaline at pH 8, were chosen as operating conditions. Given the experimental and calculated Pourbaix diagram of zinc [139, 140] these conditions suggest Zn^{2+} and $Zn(OH)_2$ as dissolving/stable species. At pH 8 the surfaces are considered stabilized, while higher dissolution

rates are expected for lower pH values. Experiments always started at a potential of 0.0 V vs Ag|AgCl, where no water splitting and stable surfaces are expected. We vary the potentials with a scan rate of 1 mV/s from (1) 0 V to +3.0 V, i.e. into the OER region, and (2) from 0 V to -1.5 V, which is into the region of the HER, respectively.

Fig. 3.3 shows the dissolution of ZnO during linear sweep voltammetry for non-polar ZnO (10 $\bar{1}$ 0) and polar ZnO (0001). Blue lines indicate the dissolution during UV illumination, whereas the black data shows dissolution under dark conditions. The electric currents corresponding to the data shown in **Fig. 3.3** are displayed in the appendix **Fig. A.1.2**. The figures indicate a number of interesting details as follows.

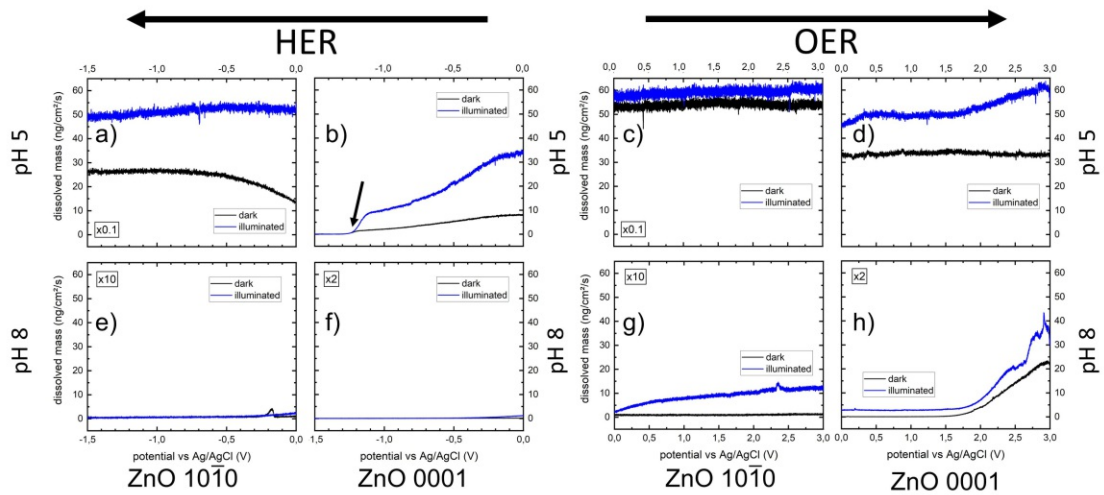


*Figure 3.3: Dissolution rates of ZnO 0001 and 10 $\bar{1}$ 0 face in 10 mM ClO_4^- solutions during Linear Sweep Voltammetry (1 mV/s). Please note that all panels are similarly scaled, but some of the data is multiplied by a constant to be visible in the plotted range, as indicated. Arrows indicate scan directions. Significantly higher dissolution rates can be observed with lower pH (**a**) and **b**). Illumination results in higher dissolution rates (c.f. text for details).*

First, the effect of pH is very evident. When performed at pH = 5 both surface orientations show 1-2 orders of magnitude higher dissolution rates compared to pH = 8. This is consistent with the expected dissolution tendencies derived from Pourbaix diagrams. ZnO is considered stable from pH 8 to pH 6 and around 0 V vs Ag|AgCl. Below pH 5 thermodynamic instability drives the dissolution. Further,

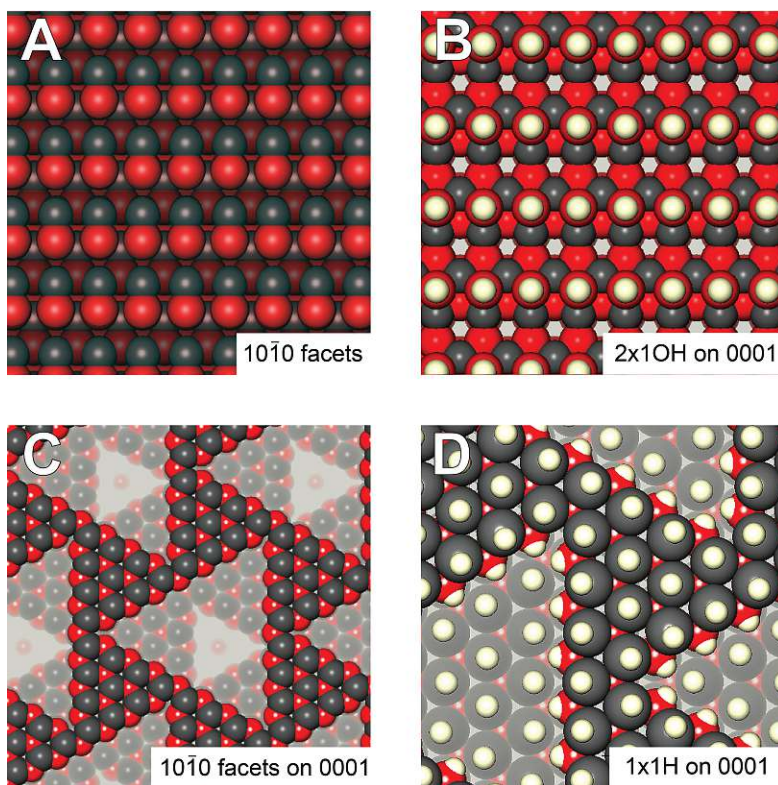


Figure 3.4: (A) ideal non-polar ZnO ($10\bar{1}0$ surface (B) half coverage by hydroxide (C) Triangular reconstruction on ZnO(0001) (D) Stabilization by formation of triangles of $10\bar{1}0$ orientation and additional coverage with a hydrogen layer. Oxygen: red, zinc: black, hydrogen: beige

(Fig. 3.3 a, c, e, g) also show that non-polar ZnO($10\bar{1}0$) surfaces exhibit very high dissolution rates at pH 5 at both, HER and OER conditions, when compared to the polar ZnO (0001) shown in (Fig. 3.4 b, d, f, h). As emphasized, the rates for the non-polar surface are in general about 1 order of magnitude larger compared to the polar surface, while water splitting currents are insignificant within the scanned regions towards HER and OER (see again Fig. A.1.2).

Also, both surfaces show a rather constant or increasing dissolution rate when polarizing towards OER at pH = 5. Surprisingly, at pH = 5 the polar surface shows a very significant decrease of the dissolution rate towards HER conditions (marked by arrow in Fig. 3.3b)). As soon as hydrogen evolution starts the polar surface shows insignificant dissolution rates (see Fig. 3.3 b) in acidic conditions.

At pH 8 shown in **Fig. 3.3 e/f**, both surface orientations show low dissolution rates towards the HER, which get even lower with increasing negative polarization.

Interestingly, as soon as the OER initiates at pH 8 the polar surface shows an approximately one order or magnitude higher dissolution rate (**Fig. 3.3 h**) compared to the non-polar surface (**Fig. 3.3 g**). Again the non-polar surface shows no significant OER current at the applied potential, while the polar surface can split water effectively, yet at a high corrosion rate (see again **Fig. A.1.2**).

Second, illumination with UV light in general results in higher amount of dissolved zinc for both surface orientations. The relative increase of dissolution rates under illuminated conditions varies strongly with the pH, applied potential and surface orientation. In the acidic case in the HER direction, for ZnO(10 $\bar{1}$ 0) (**Fig. 3.3 a**) illumination almost doubles the amount of dissolved ZnO. Also, under illumination degradation seems to be constant while decreasing the potential, while it increases in the dark. Moreover, the same applies for the OER (**Fig 3.3 c**) at pH 5. Here the dissolution reaches very high rates. Also the difference between illuminated and dark case is still about 10-50%, for each surface respectively, at an already very high level.

For the OER scan at pH 8 (**Fig. 3.3 d**) a significant effect of illumination was observed for both orientations. Specifically, under illumination the ZnO dissolution rate is growing at a low level for the ZnO(10 $\bar{1}$ 0) as the potential rises (see **Fig 3.3 g**), while it is considerably higher for the polar surface. No significant oxygen evolution accompanies the dissolution of the non-polar surface, while the polar surface evolves oxygen. In contrast, under dark conditions at pH 8 dissolution remains negligible over the whole potential window. As already pointed out above, for the polar surface (**Fig 3.3 d, h**) the dissolution rate is considerably higher compared to the non-polar surface at positive polarization, also during illumination.

At negative polarization at pH = 8 the effect of illumination is insignificant for both surface orientations (**Fig. 3.3 e, f**) and the Zn dissolution drops below the limit of detection at HER evolution.

3.4 Discussion

The key to understanding the observed behaviour of the different ZnO facets is to consider the stabilization and dissolution mechanism of the facets.

Considering the wurtzite structure of ZnO, along its c-axis ZnO is made up of alternating layers of hexagonal close-packed Zn^{2+} and O^{2-} resulting in a O-terminated surface on one and a Zn-terminated on the opposing side. This generates a diverging dipole across a crystal, and will render the polar ZnO(0001)-Zn prone stabilizing reconstructions.[125, 131] Specifically, the dipole through the crystal has to be eliminated by triangular reconstruction of, or adsorption of ad-atoms on the surface[125, 131, 141]. In contrast other low index surface orientations have stoichiometric ZnO terminations, and do not exhibit complex reconstructions.

The resulting surface structures for the polar and the non-polar surface are shown in Fig. 3.4. As displayed, **A)** the ideal non-polar ZnO($10\bar{1}0$) surface consists of rows of ZnO pairs, hence displaying both under-coordinated yet stoichiometric Zn and O ad-atoms at the surface. Panel **B)** shows a possible (2x1)OH adsorption layer, that can stabilize the polar Zn-terminated surface in alkaline[125] and water-rich media[124, 126], and **C)** shows an alternative possibility to stabilize the polar surface[131]. Here, triangular features are formed, which also offer oxygen atoms in a stoichiometric concentration to stabilize the surface. Panel **D)** shows a similar surface reconstruction but triangles and step-edge oxygen atoms are covered with a hydrogen layer. The latter structure is thermodynamically stable under hydrogen rich conditions. [127]

In our previous work[124] and in **Fig. 3.5** we now show how a ZnO(0001) surface dissolves when lowering the pH from 8 to acidic conditions. The in-situ AFM series, recorded with two different single crystals, in **Fig. 3.5 A-D** shows persistence of 0001 terraces, where degradation/dissolution occurs along the step edges, which are non-polar surfaces. This confirms, that the non-polar step edge surfaces are considerably more unstable compared to the stabilized polar surface. This is consistent with the observed higher dissolution rate of the non-polar surface at low pH and all potentials.

Fig. 3.5 E shows the polar surface after extensive etching in acidic conditions. Here a surface reconstruction with triangular features on the (0001) surface becomes visible. This is what we previously observed and indicates a kinetic stabilization of the surface by formation of triangular features, which have no kink sites.[124] This slows down dissolution rates significantly.

These triangular features are hence the reason for the lower dissolution rates at $\text{pH} = 5$ of the polar surface when compared to the non-polar surface, as observed for the potential dependent data above. The non-polar surface is not stabilized, and indicates dissolution rates that are at least one order of magnitude higher at $\text{pH} 5$.

Interestingly, for the polar surface **Fig. 3.5 D** also shows that lowering the pH results in holes (marked) before typical triangular features appear. These holes indicate that the stabilizing OH/O ad-layer dissolves at lower pH , which effectively forces the polar surface into a different stabilization mechanism shown in **Fig. 3.5 E**.

Furthermore, the sudden drop of dissolution of the polar surface during negative polarisation in acidic conditions in **Fig. 3.4 b** suggests a protecting adsorption of hydrogen on the (0001) surface structure as indicated in **Fig. 3.4 D**. Here, under active HER conditions, where hydrogen must adsorb on the surface, the proposed 1H (1x1) adsorption layer [127, 142] on ZnO(0001)-Zn does lead to a stabilisation of the surface under active and hydrogen rich conditions. Indeed, also our previous theoretical investigations showed that 1x1H coverage can be an effective surface stabilisation at hydrogen-rich conditions.[127] Hence, correlation of phase diagrams and experimentally observed stability with ICP-MS flow cells proves to be beneficial for designing stable materials.

Specifically, the data suggests that hydrogen effectively stabilizes ZnO(0001) by a theoretically predicted 1x1H adsorption on Zn and step edge atoms of the typical triangular reconstructions. A direct evidencing of 1x1H adsorption on polar ZnO at solid/liquid interfaces is currently not feasible, however in future studies we aim to utilize AFM/STM imaging at the solid/liquid interface to provide a direct experimental evidence. The applied overpotential in the experiment suggests that



Figure 3.5: In-situ AFM topographies indicate preferential dissolution of $10\bar{1}0$ step edge surfaces on a (0001) surface (marked by arrows) upon decrease of the pH values from (A/B) pH 8 to 6, and (C/D) pH 8 to pH 3. (E) shows an ex-situ topography after immersion into a pH 3 solution, indicating stabilization by formation of triangles with step edges of $(10\bar{1}0)$ orientation on (0001) surfaces (c.f. text for details).

the conditions in this work are capable to achieve conditions, where ZnO(0001)-Zn is indeed stabilised by this 1×1 H adlayer, which is stable in extended ab initio phase diagrams under reactive conditions.[127] Consequently, the sudden drop of the dissolution rate may coincide with the theoretically predicted 1×1 H hydrogen adsorption. This suggests an operating condition on the ZnO(0001) surface where hydrogen evolution proceeds under conditions that thermodynamically stabilize the surface by 1×1 H coverage, while water is beyond its thermodynamic stability. This effectively renders the surface inert against degradation under reactive water splitting conditions. This is an interesting mechanistic insight and may prove useful for designing other stable surfaces under operating conditions.

Conversely, in the alkaline case the low dissolution rate (seen in **Fig. 3.3f**) correlates well with the expected OH coverage of the ZnO(0001)-Zn surface (**Fig. 3.4 B**) and the general thermodynamic stability of ZnO.

A very interesting aspect at pH 8 is that the polar ZnO(0001) surface is less stable compared to the non polar surface under oxygen evolving conditions. This is unexpected, as one would expect that oxygen rich conditions stabilize triangular reconstructions on the polar surfaces. This has two reasons.

First, oxygen evolution on polar ZnO(0001) may proceed via a direct reaction of water with step edge oxygen atoms or stabilizing OH ad-atoms. As such, the stabilizing features will dissolve during oxygen evolution, which makes the surface less stable and prone to corrosion under reactive conditions. Why dissolution is

less significant for the non-polar surface is then evident. On this surface the oxygen evolution does not proceed at a significant rate at all, the observed dissolution is solely due to the applied potential for the intrinsically thermodynamically stable non-polar surface at $\text{pH} = 8$.

Second, UV irradiation also triggers dissolution of the polar ZnO surface at $\text{pH} 8$, under any condition above about 0 V, while the non-polar is significantly less prone to photo-corrosion. For the polar surface this is also well visible in UV on/off experiments recorded at $\text{pH} 8$ at 1.5V, which are shown in **Fig. 3.6**. This is interesting, as ZnO is in principle thermodynamically stable at $\text{pH} = 8$. Hence, holes h^+ can apparently interact with the stabilizing electronic surface states of the ZnO(0001) surface, forcing it into dissolution via equation 3.2.

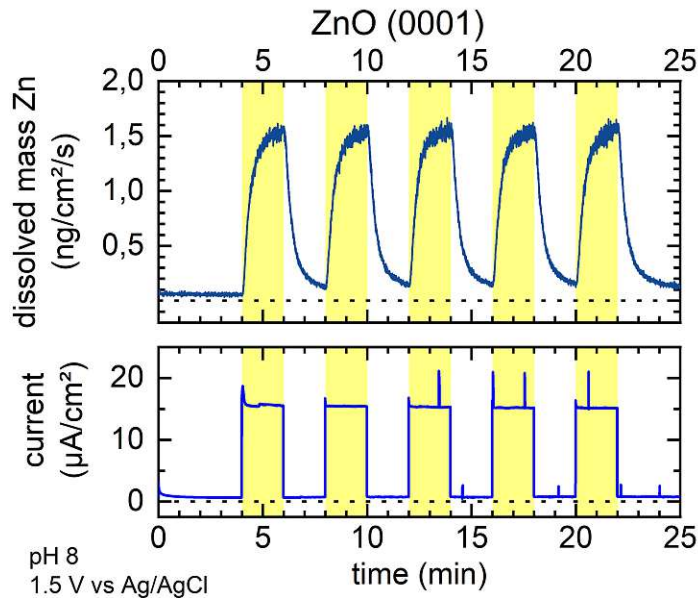


Figure 3.6: Dissolution and electric current of a ZnO (0001) surface held at 1.5 V vs Ag|AgCl in perchlorate solution at pH 8 while UV light is switched on (yellow areas) and off. Dissolution and current response on UV exposure is clearly visible.

UV irradiation was generally found to increase the rate of dissolution. This is likely via amplification of equation (3.2). Generated holes can oxidize the oxygen in the semiconductor to its molecular form while releasing zinc ions into solution. This process competes with the desired water splitting reactions, and drives the disso-

lution under all conditions, with the exception of ZnO(0001) under hydrogen rich conditions at low potentials. This is again in line with the stabilization mechanism of the polar surface via hydrogen adsorption on terraces and step edges.[127]

Interestingly, the stabilization of hydrogen on the polar surface also results in the highest rate of hydrogen evolution (see currents in **Fig. A.1.2**), yet at the lowest dissolution rate under both illuminated and dark conditions. As such these results strongly support the idea that *hydrogen stabilized polar surface structures on semiconducting oxides* can effectively moderate hydrogen evolution under stable conditions. As such, combined with transition metal coverage, ZnO(0001) or other polar surfaces may be an interesting candidate for a stable hydrogen evolution catalyst.

In contrast oxygen evolving conditions render ZnO(0001) unstable, with the ongoing OER the dissolution rate of ZnO increases in concert at pH 5 and pH 8. This again indicates a mechanism that proceeds via dissolution of oxygen step atoms. Interestingly, at pH 8 under OER conditions the non-polar surface appears more stable but oxygen evolution rates are insignificant at the tested potentials, indicating a large overpotential for the OER on the non-polar surface.

3.5 Conclusion

In summary, stabilization of the ZnO(0001)-Zn surface in both acidic and alkaline aqueous electrolytes was studied by means of a photoelectrochemical flow cell with consecutive detection of degradation products via ICP-MS. The well-known polar surface stabilisation mechanisms [124, 126, 128, 131] seem to also apply for photoelectrochemical conditions. The time and potential-resolved dissolution study on polar and nonpolar zinc oxide revealed the following conclusions:

- ZnO is prone to photocorrosion by ultraviolet light to different extents depending on their orientation.
- However, polar ZnO(0001) can stabilize during HER via formation of protective (1x1)-H layer in acidic and (2x1)-OH in alkaline electrolyte. This structure also support highest measured hydrogen evolution currents, yet

under very stable conditions. In contrast, non-polar ZnO shows no significant hydrogen evolution, yet high dissolution at HER potentials.

- Nonpolar ZnO is in general less stable compared to polar ZnO for all pH values and potentials probed. The exception to this is oxygen evolution at pH 8. Under these conditions the non-polar surface is more stable, but also evolves no oxygen. This may make this surface orientation interesting for a carrier material under these conditions.
- Extended ab initio phase diagrams correlate well with experimentally observed stabilities beyond the stability of the water phase, suggesting that phase diagrams are an ideal tool for screening stable candidate surfaces outside the water stability window. This region is not typically evaluated in this type of simulations.

Our approach for testing photocatalysts during operation on its photocorrosion might prove useful for further, and more complex systems. In addition, our results highlight that surface design (facet preferences and stabilisation mechanism of oxides) can provide an effective path to making (photo)electrocatalytic (support) surfaces more stable during reactive conditions. Stabilisation mechanisms of polar surfaces may provide an effective path to tuning stability of transition metal oxides under electrochemical and photoelectrochemical conditions.

Chapter 4

Comparison of Elemental Resolved non-confined and restricted electrochemical degradation of Nickel Base Alloys

This chapter is based on the article published under the same title at Corrosion Science (in press[143]). It focuses on the challenge any flow cell has. To define the flow profile the electrolyte has to be channeled, mostly by using O-rings. These necessarily induce the formation of a crevice underneath the O-ring. Exemplarily on various Nickel based alloys (NBAs) the influence of the crevice created under the O-ring is examined for the resulting corrosion mechanism.

The majority of the experiments were conducted by the author, only the XRF measurement was done by Claudia Merola and and Hsiu-Wei Cheng. Flow simulations were supplied by Lukas Kalchgruber.

Passive film properties of nickel base alloys (NBAs) have been studied extensively, yet elemental resolved dissolution currents under corrosive conditions are less well studied. Here, we compare elemental dissolution currents during

anodic polarisation and repassivation under crevice and freely-exposed conditions for various NBAs using an ICP-MS flow-cell approach. With a new sample design we can track communication of a crevice environment with the electrolyte, providing insight into crevice solution chemistry and solubility of passive film-forming elements. Data indicates Mo can only form stable precipitate layers under openly corroding conditions. Local elemental depletion was further examined by XPS and nanometer resolved XRF.

4.1 Introduction

Compared to stainless steels nickel base alloys (NBAs) are considerably more corrosion resistant making them a preferred industrial choice in demanding environments, including chemical and food processing, aerospace as well as energy applications[144–147]. NBAs are typically alloyed with >10% chromium and 1-5% molybdenum which are key alloying elements for providing an excellent corrosion resistance in extreme environments[148–151]. The pronounced corrosion resistance in anodic and acidic environments suggests the formation of a very stable and well adhering passivating thin film, which is formed and/or stabilized mainly by these alloying elements[151–154]. It has been suggested that molybdenum and chromium may segregate to the alloy surface[108, 149, 152, 154, 155].

The thickness of the passive films is estimated at about 2 nm[149, 156] and the chromium content is known to strongly influence the breakdown of the passive film. This suggests a key role of chromium in the passive film chemistry, formation kinetics and stability[152, 156]. The mechanism of molybdenum inhibition is less well understood. Increasing molybdenum content results in lower passive currents, and it was suggested that MoO_4^{2-} ions (molybdates) accumulate at the outer interface of the passive film[155]. This may stabilize the passive film against chloride ingress and hence dissolution, resulting in lower corrosive currents[149, 157].

It was further suggested that molybdenum forms insoluble molybdate species after anodic dissolution from the matrix, building up passivating precipitate films which in turn lowers anodic dissolution rates[108].

JAKUPI *et al.*[158] suggested that molybdenum may accumulate at defect sites, which may also trigger lower anodic dissolution rates at defect sites.

While passive films and passivity have been studied extensively for NBAs, the elemental resolved dissolution during and after breakdown of the oxide, specifically under crevice and pitting conditions, is less well studied. Material dissolution is a central aspect of an ongoing localized corrosion, and industrial cleaning procedures involve pickling, where a complete oxide breakdown is desired, which is particularly demanding for NBAs[159].

Recent studies by OGLE *et al.*[108] investigated the transpassive dissolution in high salt environments, and NBA passivation in acidic solutions[160] using spectroelectrochemistry in flow-cells coupled to ICP-OES analysis.

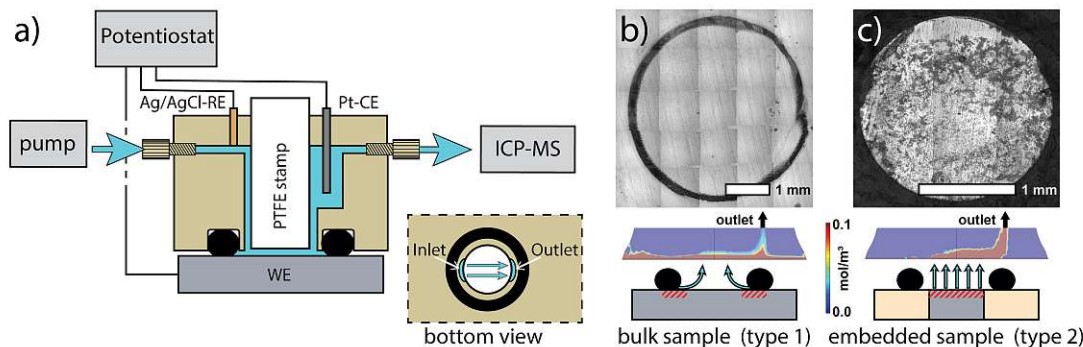


Figure 4.1: a) Schematic of the flow cell used. A PTFE cylinder is used for establishing laminar flow across the working electrode. The counter electrode (Pt) is placed up-stream and the reference electrode (Ag/AgCl) is placed downstream to avoid contamination of the WE. Standard HPLC fittings are used for all tubings. Corrosion patterns for different types of experiments are shown schematically and as microscope pictures for b) crevice corrosion and c) embedded samples, as well as a finite element method simulation (see methods) of the concentration distribution after 1.5 sec of material release at the electrode surface.

Here, we use a similar approach in a newly designed ICP-MS flow cell[88, 161] shown in **Fig. 4.1a**. This cell allows us to measure and compare elemental dissolution rates and faradaic currents under crevice and pitting conditions (see **Fig. 4.1b/c**), depending on the sample design respectively. Similar to classic flow-cell designs a crevice is formed with the sealing O-ring, if a bulk sample (type 1) is mounted. **Fig. 4.1b**) also shows a finite element simulated concentration profile

of corroding species in the flowing electrolyte, demonstrating significant dissolution in the crevice region under the O-ring. In contrast, as shown in **Fig. 4.1c**, an embedded sample (type 2) can be mounted without crevice formation under the O-ring. The well adhering glue limits crevice formation at the embedded glue/sample edge during experimental duration, as demonstrated by comparison of the visual corrosive damage after experiments (**Fig. 4.1c**). Also, finite element simulations, shown as insets, indicate that the dissolving species originate from the exposed area. The flow is also guided well into the exit for both sample settings, ensuring limited convective broadening of the ICP-MS signal. This is ensured by the design of the flow channels, which enter and exit as circular openings between O-ring and a PTFE stamp. This ensures a stable channel height and laminar flow.

Table 4.1: Bulk composition (weight ratios) and abbreviations for all NBAs used.

Alloy composition	abbreviation	Ni	Cr	Fe	Mo	minor components
Ni ₈₆ Cr ₅ Fe ₉	Cr5	86	5	9	-	-
Ni ₇₅ Cr ₁₆ Fe ₉	600	72	15.5	8	-	Mn(1) Si(0.5)
Ni ₇₄ Cr ₁₆ Fe ₉ Mo	Mo1	74	16	9	1	-

Using this setup, we study the elemental dissolution behaviour of a series of commercial and model NBAs under crevice and non-crevice conditions. The alloy compositions and abbreviations used in this work are given in **Table 4.1**. The compositions were selected for evaluating the influence of the total chromium content (5% and 16% Cr) and the impact of trace/minor amounts of molybdenum (1% Mo) on initial corrosion and subsequent repassivation.

4.2 Experimental Section

Chemicals and Materials Sodium chloride (Carl Roth, p.a.), HNO_3 (VWR Chemicals, Normatom), Milli-Q water (resistivity $>18 M\Omega \cdot cm$, total organic carbon < 4 ppb) was used for making electrolyte solutions. Alloy 600 was obtained

from VDM-Metals, and Cr5 and Mo1 were provided by Hauke Springer (MPI f. Eisenforschung, Düsseldorf). For embedded samples a 2 mm diameter cylinder was turned. The removed material was replaced with EPON 1009F epoxy resin (Hexion). The metal blocks were ground with sand paper of decreasing grain size (from P80 to P2500), then polished with diamond paste down to $0.05 \mu\text{m}$. Prior to electrochemical transcritical dissolution at $\phi_{TP} = 1.0 \text{ V}$ the metals were preconditioned *in situ* in the ICP-MS flow cell by (1) 5 minutes potentiostatic polarisation at -0.2V vs OCP, (2) followed by stepping into the passive regime at $\phi_1 = 0.2 \text{ V}$ for another 5 minutes. We also compared results after preconditioning at -1.0 V and subsequent oxidation in the passive regime at 0.2 V and found no quantitative differences.

Inductively Coupled Plasma Mass Spectrometry (ICP-MS) Cobalt was chosen as internal standard due to its similar mass with most of the alloy components. **Fig. 4.1** shows the flow-cell ICP-MS coupling used in this work, including flow simulations that confirm the laminar flow inside.

Optical Microscopy Optical Microscope images were taken using a μsurf explorer (NanoFocus AG) and analyzed with μsoft metrology software. A 20x magnifying lens was used.

Scanning Electron microscopy (SEM) SEM imaging was performed at the USTEM facility at Vienna University of Technology, working on a FEI Quanta 250 FEG with a beam energy of 5 keV .

X-ray Photoelectron Spectroscopy (XPS) XPS Chemical composition and chemical states of the surface were determined using the Axis Supra (Kratos Analytical) spectrometer. No charge neutralization was used. XPS spectra were shifted with respect to adventitious carbon at 284.8 eV . Spectra were taken with a resolution of 0.1 eV and a pass-energy of 160 eV . All spectra were fitted using reference compounds from the NIST database (Ni, Fe, Cr, Mo)[162–165]. No positional shifts of the components were necessary to fit the measured spectra well, except for an 0.2 eV shift for $\text{Ni}(\text{OH})_2$ and 0.5 eV shift for NiO reference compo-

nents. Elements with unpaired electrons (Cr, Fe) were fitted with fixed multi-peak envelopes[163, 166]. Samples were during active potential application pulled out of electrolyte to 'freeze' the electric double layer. Afterwards they were dried in a N_2 stream.

X-ray fluorescence (XRF) High resolution X-ray fluorescence (XRF) experiments were performed at the Taiwan Photon Source (TPS) Beamline 21A at the National Synchrotron Radiation Research Center (NSRRC), Taiwan. This beamline is dedicated to white-light nano Laue diffraction for structural analysis and high spatial resolution fluorescence imaging. The spatial resolution can regularly reach 80×80 nm at this beamline. In XRF application, the beamline utilizes a pre-shaped Kirkpatrick-Baez mirror pair to focus the Monochromatic X-ray beam with energies 9.6 keV to generate fluorescence signal. XRF was collected by an in-plane detector with an take-off angle of 7 degree to increase the sensitivity to the surface fluorescence signal. Due to the fact that absolute XRF signal intensity is also influenced by the surface morphology, we normalize the fluorescence imaging and analyze intensity ratio between individual elemental signals as following, revealing relative local variation of elemental ratio on the surface:

$$P_{Me}(\%) = I_{Me}/(I_{Ni} + I_{Cr} + I_{Fe}) \cdot 100\%$$

The sampling depth of XRF technique is related to the photon energy of fluorescence, which is characteristic for individual elements. A rough estimation of the sampling depth from the XRF energies for Ni, Cr and Fe suggests 2.36, 0.96 and 1.53 μm sampling depths in this sampling geometry.

Finite Elements Methods Simulations Simulations for the concentration profiles shown in **Fig. 4.1 b) and c)** were conducted with COMSOL Multiphysics. The initial material release is set to be evenly distributed over the whole WE area. Electrolyte mass flow was set to 3 mg/s as measured for the experiments conducted.

4.3 Results

Here, we first quantify elemental dissolution currents i_{MS} during polarisation at different anodic polarisation for crevice and non-crevice type samples in the ICP-MS (see again **Fig. 4.1**). We characterize extended corrosive dissolution and the subsequent repassivation of the materials, to obtain insight into the crevice chemistry. As a side note, in this work we do not study freely corroding crevices under OCP conditions, we rather accelerate the degradation reaction by application of anodic potentials, in the transpassive regime.

We then further characterize the surface chemistry of corroded and repassivated alloys with X-ray photo-electron spectroscopy (XPS) and discuss the passivating film chemistry and structure before and after corrosive dissolution. Finally, high-resolution X-ray fluorescence spectroscopy was performed on corroded samples, to further visualize local elemental surface depletion at corroding sites.

4.3.1 Anodic polarisation and elemental resolved dissolution.

Fig. 4.2 displays representative data of elemental dissolution currents i_{MS} recorded during 40 minute active corrosion with a type 1 (electrochemically triggered degradation under confined conditions) and type 2 (open area electrochemical degradation) samples at $\phi_{TP} = 1.0$ V for, Ni₈₆Cr₅Fe₉ (Cr5), Alloy 600, and Ni₇₄Cr₁₆Fe₉Mo in aerated 1 mM NaCl solution at unbuffered pH of 7, respectively.

First, based on absolute dissolution currents, these three samples indicate increasing corrosion resistance from Cr5 < Mo1 ~ Alloy 600 for the electrochemically triggered degradation under confined conditions (CC), and Cr5 < Alloy 600 < Mo1 for open area corrosion.

Second, under crevice condition **Fig. 4.2 a-c**, stepping from 0.2 V to 1.0 V, *i.e.* results in an immediate and steep increase of nickel dissolution rates over more than one order of magnitude for all alloys. Alloys 600 and Mo1 further indicate a peak dissolution of nickel after 30 seconds, followed by a steady decay of the dissolution rate during ongoing corrosion at 1.0 V. In contrast, for the Cr5 alloy Cr dissolution

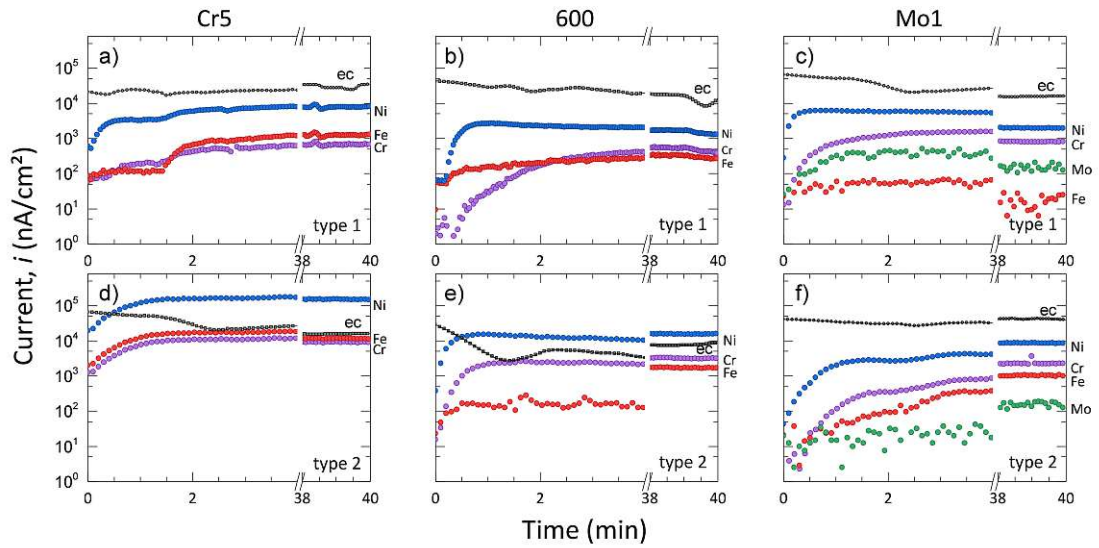


Figure 4.2: Comparison of anodic dissolution at bulk $pH = 7$ in 1 mM NaCl of Cr5, alloy 600 and Mo1. Multiple repetitive measurements provided similar quantitative results. Rates are normalized to the electrode area, which is estimated at the circumference and width of the observed crevice for type 1, and the embedded area for type 2 samples.

shortly plateaus after 30 seconds, and after 90 seconds the dissolution rate of all elements increases further. **Fig. 4.2 a** also shows that for Cr5 the second increase of $i_{MS(Ni)}$ after 90 seconds is accompanied by a step increase of the iron dissolution rate over more than one order of magnitude. The dissolution ratios (D_R) after 40 minutes active corrosion shown in **Fig. 4.3** indicate that Cr5 reaches close to bulk dissolution ratios, while Alloy 600 and Mo1 exhibit comparatively higher Cr, as well as considerably enhanced Mo dissolution ratios, respectively, with a clearly retarded Fe dissolution under crevice conditions.

Under openly corroding conditions of embedded samples **Fig. 4.2 d-f**, stepping from 0.2 V to 1.0 V , *i.e.* indicates a similar pattern with a very steep increase of Ni-dissolution. In contrast to the CC type and shown in **Fig. 4.3**, open corrosion establishes a near bulk-ratio dissolution after 40 minutes, with moderately higher Ni, and hence lower Fe and Cr dissolution rates, compared to the bulk composition.

For the open corrosion we also see that the electrochemical current (ec) is lower

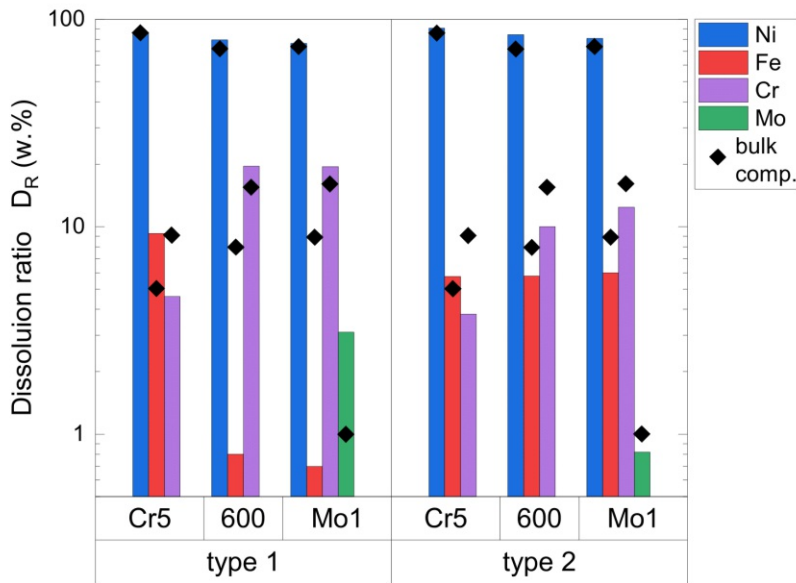


Figure 4.3: Extended anodic dissolution ratios D_R for all n elements after 40 minutes of corrosion for all NBAs under different conditions of anodic polarisation calculated as $D_R = \frac{i_{MS(j)}}{\sum_{j=1}^n i_{MS(j)}}$. Bulk values are indicated by black diamonds.

compared to measured dissolution current for Cr5 and Alloy 600. In contrast, Mo1 shows a generally very low corrosion rate, with a second increase of rates after an initial 2-3 minutes of anodic corrosion.

4.3.2 Repassivation.

Fig. 4.4 compares elemental dissolution currents for all alloys and sample types during repassivation after 5 and 40 minutes of corrosive polarisation, respectively.

Due to diffusion broadening[92], all samples show that the dissolution currents for all alloys drop to a lower base level within 60-100 seconds after stepping into the repassivating region at $\phi_1 = 0.2$ V. This results from the retention time of the dissolved material in the tubes between the electrochemical cell and the detection in the ICP-MS.

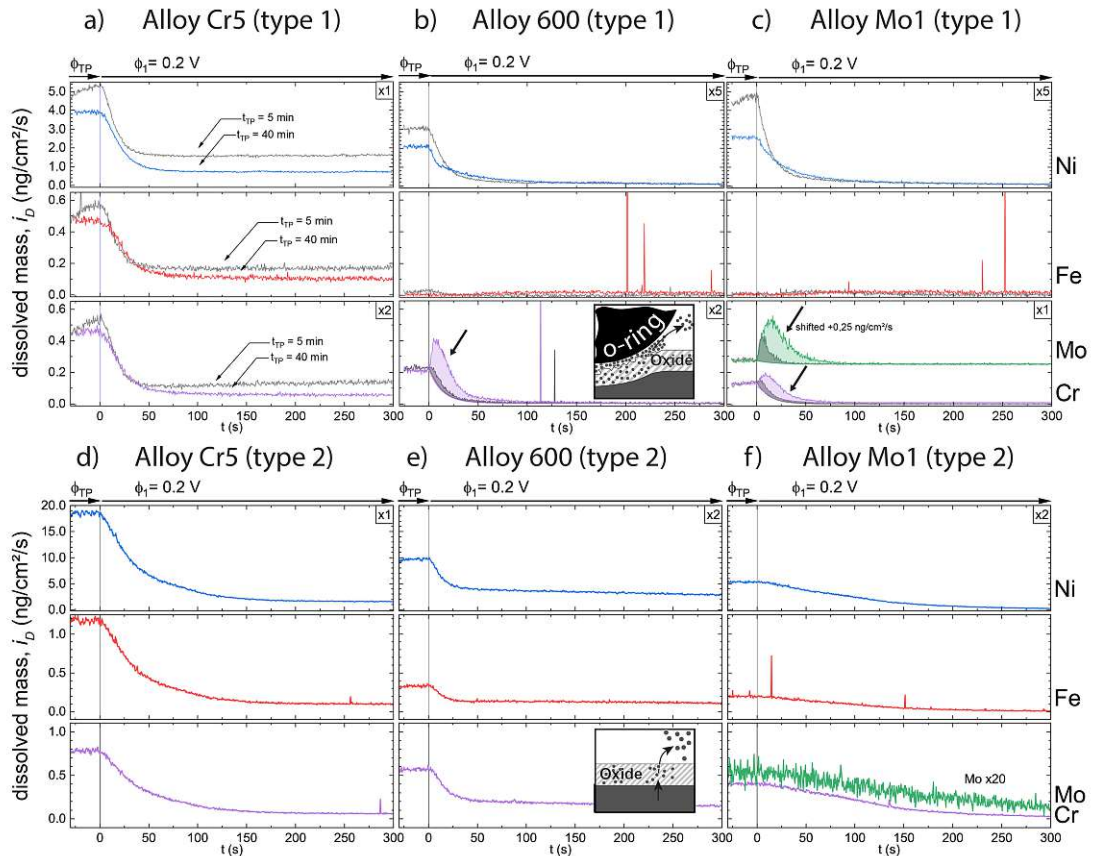


Figure 4.4: Elemental dissolution rates during repassivation after 5 and 40 minutes polarisation in the anodic region (grey: 5 min, colored: 40 min). **a)+c)** $Ni_{86}Cr_5Fe_9$ **b)+d)** $Ni_{75}Cr_{16}Fe_9$ and **c)+e)** $Ni_{74}Cr_{16}Fe_9Mo$. Notice: For **b)** and **c)** Ni-rates are multiplied by 5 for **e)** and **f)** by 2, and Cr-rates of **a)** and **b)** are multiplied by 2 to be at scale for all alloys, respectively. **a)-c)** show samples with crevice (type 1). Insets show schematically the mechanism of dissolution for type 1 & 2.

Type 1 samples: **Fig. 4.4a-c** shows type 1 samples, indicating that the base level for the Cr5 alloy is almost half an order of magnitude higher compared to alloys 600 and Mo1. This is in line with the polarisation curves, shown in appendix **Fig. A.2.1**. For Cr5 the passive current level also depends on the transpassive polarisation time. After 5 minutes of the resulting passive dissolution the current of all elements is about 20-30% higher compared to longer polarisation times. In contrast, both alloy 600 and alloy Mo1 show no pronounced difference of dissolution currents after 5 or 40 minute anodic corrosion followed by repassivation.

During repassivation the iron dissolution remains negligible for alloys 600 and Mo1, and remains at a significantly higher level for the Cr5 alloys.

In contrast to the Cr5 alloy both, alloys 600 and Mo1, indicate a significant initial peak of the dissolution rate of Cr and Mo during repassivation (marked by arrow), which increases with the time of preceding anodic polarisation. The dissolution rates for Cr and Mo peaks are considerably above the value measured during corrosive dissolution, indicating a significant material release during repassivation.

Fig. A.2.2 in the appendix compares the integrated amount of dissolved chromium and molybdenum during repassivation as a function of the transpassive polarisation time. Data indicates a saturation after about 20 minutes of transpassive polarisation. Furthermore, comparing the integrated Cr and Mo dissolution currents for alloys Mo1 and 600 (**Fig. A.2.2**) during repassivation indicates that the Mo content in Mo1 results in a smaller dissolution current for the Cr during repassivation for up to 20 minutes of corrosive polarisation. During this initial period a considerably larger amount of Mo peak dissolution occurs during repassivation, while only limited chromium dissolution emerges. After 20 minutes of corrosive dissolution the dissolved amount of chromium is again similar compared to alloy 600 that is polarised at 1.0 V.

Type 2 samples: For type 2 samples shown in **Fig. 4.4d-f** no such peaks were observed, and for Cr5 and Alloy 600 a decay of the dissolution currents consistent with diffusion broadening was observed. In contrast, Mo1 shows a prolonged dissolution time for all elements during repassivation.

4.3.3 Surface characterization - XPS.

XPS was further used to compare passive films formed during passivation and after corrosion and repassivation. Therefore spectra were collected at openly corroded and at crevice corroded regions, using a small spot XPS. For these XPS measurements the surfaces were pulled out from the electrolyte at the given potential and they were washed afterwards with minute amounts of Milli-Q water, to avoid significant changes of the surface chemistry due to washing (see experimental details for more information). We want to emphasize, that this procedure allows us to closely resemble, or "freeze"[167], the conditions in the electrolyte. But clearly, *ex-situ* XPS is only an approximation for the state during active aqueous degradation. In future work, one may expect further insight from high pressure XPS[168, 169].

The full set of core level spectra for all alloys and elements are shown in the supporting information for all materials studied for openly corroded areas (**Fig. A.2.3-A.2.5**), and crevice corroded areas (**Figures A.2.6-A.2.7**) respectively. Peak fitting was applied as shown in the spectra, and resulting XPS surface ratios for metallic and oxide components of fitted compounds are summarized in **Fig. 4.5a**.

Survey spectra indicated no further elements other than atmospheric carbon. We first summarize the results of the spectra for the major elements, while Mo is discussed separately, as it indicates most pronounced differences.

Cr, Fe, Ni spectra after non-crevice passivation. After 40 minutes of open crevice free passive polarisation at 0.2 V 600 and Mo1 indicate a Cr_2O_3 and Fe(III) enriched passive film, while oxidized Ni appears to be insignificant, and mostly metallic Ni is observed. In contrast, Cr5 shows a considerably more Ni-rich (60%) and the Cr content in the passive film is still two-fold above bulk level concentration.

Cr, Fe, Ni spectra after open corrosion. XPS spectra recorded after corrosion (**Figures A.2.3-A.2.5**) indicate significant differences of the passive film content. First, the Ni-signal indicates a more pronounced oxide/hydroxide component after reprecipitation, which is in line with a reprecipitated outer layer of

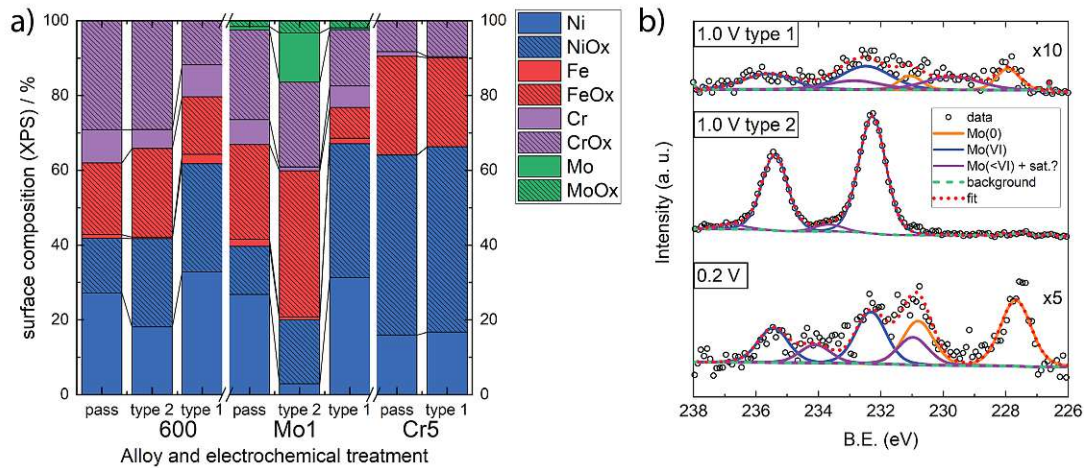


Figure 4.5: a) Surface composition of the alloys according to XPS analysis. Type 1 and 2 were polarised at 1.0 V for 40 min, pass indicates passivation at 0.2 V for 40 min. Type 1 is measured at the area of the crevice, type 2 represents the data taken from spots in the inner part of the metal sample. b) Molybdenum 3p core level spectra after 40 minutes of polarisation in the (bottom) passive regime at 0.2V, and (top) the anodic regime at 1.0 V for type 1 and type 2 polarisation. (c.f. text for details).

nickel oxide/hydroxide. Also, the metallic signals for both alloy 600 and Cr5 show a considerably lower intensity of metallic Cr and Fe relative to the oxidized species, indicating a thicker passive film.

Cr, Fe, Ni spectra after crevice corrosion. Spectra under crevice condition (Figures A.2.6-A.2.7) clearly indicate a thinner oxide in the crevice corrosion. Specifically, relative comparison of the metallic and the oxide peaks indicates a relatively higher metal signal for all alloys. Further, Ni(II) shows no hydroxide signals for all alloys.

Comparison of Mo spectra. As shown in Fig. 4.5b, for Mo1 the elemental ratios of the Mo oxides strongly differ for the openly exposed, crevice and passive film surface chemistry.

First for open non-crevice corrosion (type 2), after passivation molybdenum at 0.2 V is chemically present as Mo(VI) and lower oxidized species Mo(<VI). Also, metallic Mo is clearly detectable indicating a thin passive film.

Second, and in contrast, Mo core level spectra in **Fig. 4.5** after corrosion at 1.0 V and repassivation indicate a fully oxidized and highly enriched Mo(VI) species in the passive film. The data indicates a nearly exclusive Mo(VI) content, with a minor ($\sim 6\%$) possibly defect (e.g. oxygen interstitial) related peak at even higher binding energies after transpassive dissolution and subsequent repassivation. This small peak is shifted to very high binding energies, which in our view supports an interpretation of an interstitial site, which is highly coordinated by lattice oxygen (defect). Other secondary effects such as shake ups are unlikely in this case, as the highly oxidized form is expected to be diamagnetic[170]. The total Mo content in this passive film is at 7-8%, which is considerably above the 1% bulk concentration. This indicates a thick molybdate precipitate overlayer, which is also consistent with the disappearance of the metallic Mo peak, and significantly weaker metallic peaks in all other elemental spectra (**Fig. A.2.4**).

Finally, the spectra in the crevice corroded area (type 1, 1.0 V) indicate fully oxidized species, and only minor lower oxidation states (in the noise limit). In general, the considerably smaller signal levels again indicate a lower film thickness, in particular considering that the metallic Mo signal is still visible.

4.3.4 Nano-XRF/SEM characterization of corroded areas.

Fig. 4.6 shows electron microscopy images and corresponding high resolution (500 nm spatial resolution) XRF elemental mappings for representative areas showing corrosive damage after polarisation in the ICP-MS cell. The elemental mappings show a relative distribution of elements over the probed location (see methods for details), and indicate that nickel depletes locally, while iron and chromium maps indicate a local enrichment compared to bulk level at corroded sites, which is consistent with XPS data. For Mo1 it was not possible to achieve sufficient signal intensity for mapping local changes.

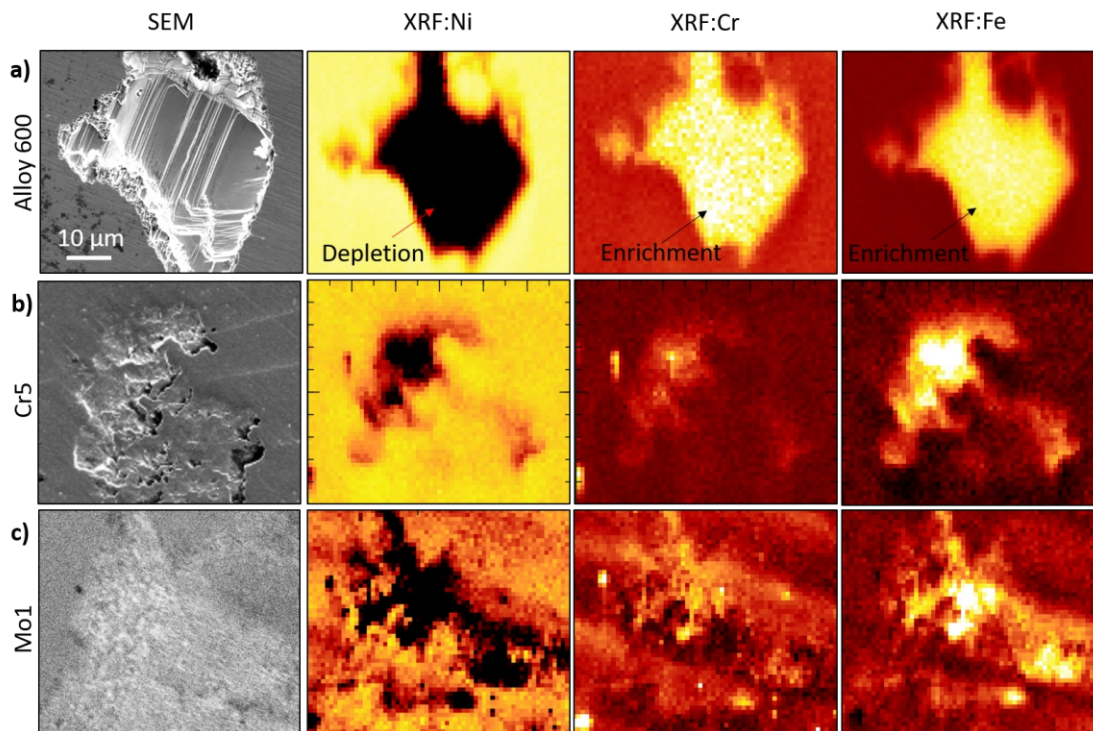


Figure 4.6: High resolution XRF characterisation of corroded areas of **a)** Alloy 600, **b)** Cr5 and **c)** Mo1 alloys. The left column shows an SEM image, followed by a column showing Ni, Cr and Fe depletion/enrichment respectively (cf. text for details).

4.4 Discussion and interpretation

4.4.1 Comparison of anodic corrosion and elemental dissolution under restricted and non-restricted conditions.

Our data indicates that we can follow both a freely exposed corrosion of an embedded sample, or preferential confined condition-type degradation (CC) underneath the O-ring using targeted ICP-MS flow cell/ sample design concepts. CC establishes a direct communication of the crevice electrolyte with the bulk electrolyte flowing through the ICP-MS flow cell.

First, the open corrosion of type 2 samples results in a preferential dissolution of Ni, while Cr as well as Fe dissolve at ratios below bulk level metal concentrations at both passivating and anodic corrosion conditions. Under passive conditions,

at 0.2 V, the Ni-hydroxide and oxide peaks in XPS almost disappear, which is in line with the observed dissolution behaviour in ICP-MS. This suggests, Ni dissolves through an intact chromium oxide layer, and any initially present oxidized Ni species dissolve as well, as expected for a high field mechanism[171–173]. I.e. the potential gradient drives the Nickel dissolution through the formed passive layer. At 1.0 V anodic corrosion we see a preferential and also localized dissolution (see also **Fig. 4.1c** photograph after corrosion), which is further evident from the XRF data, which shows depletion of Ni and enrichment of the other alloying elements locally. Localized corrosion is likely triggered by the local breakdown of the passive film. Further, for Mo1 repassivation leads to the formation of an expected passivating Mo(VI)-rich precipitate. This interpretation is consistent with previous work[108, 160], and suggests high oxidation states in the Mo-precipitate formed at 1.0 V. This precipitate dissolves slowly after repassivation, as evidenced by the slow transient ICP-MS dissolution profile of Mo in **Fig. 4.3f**. Based on the XPS data, the Mo content of the passive film increases 7-fold compared to the bulk concentration, and the film thickness is above 3-4 nm, but below 10 nm, based on the relative intensities of the metallic signals from underneath the passive film. Under different conditions e.g. OGLE *et al.*[108] found a similar enrichment of Mo at the interface, as it is also known for Mo-containing stainless steels[174].

For crevice type samples the ICP-MS repassivation data show two interesting aspects: First, and as discussed above we see clear and time dependent peaks of the Cr and Cr/Mo dissolution, for alloy 600 and Mo1 respectively. These peaks were only found for type 1 samples. Hence, these are clearly related to the communication of the crevice solution with the flowing electrolyte. Upon lowering of the potential, the crevice environment, which established over the extended degradation period, dissipates by peaking, i.e. injecting, the crevice solution into the flowing electrolyte. Hence, the crevice solution at pH 7 base-level unbuffered pH is highly enriched in Cr and Mo containing soluble species, while Fe remains largely insoluble within the crevice. Based on the time dependent evolution of this dissolution peak, shown in **Fig. A.2.2**, the crevice environment reaches saturation after 20 minutes of constant polarisation under the applied conditions [169]. The here studied approach deviates from realistic crevice corrosion since an exter-

nal potential is applied, that likely results in an overestimation of the exchanged currents[175]. Nevertheless the processes taking place in the crevice environment are comparable. The here reported enrichment in soluble species in the crevice is also found for crevice corrosion[176, 177]. Interestingly, for Mo1 data indicates a delayed Cr dissolution, while Mo preferentially dissolves initially. After 20 minutes, similarly, a saturation level is reached.

Further the observed Fe retardation for both alloys indicates that the crevice is enriched with iron oxide, while Cr-oxide and Mo have lower effective protection levels in the crevice. The resulting oxide/ transient protection layer is non-well adhering and does not passivate the active crevice surface well. This is consistent with 1) the observed current spikes in the Fe signal. The observed spikes indicate nano-to-micro level Fe-oxide detachment from the repassivating areas, and 2) XPS of the crevice region also indicates Fe enrichment, and overall thinner oxide.

When comparing the surface composition of non-confined with the crevice corroded samples, data clearly suggests an acidification of the crevice area, which drives localized corrosion, while inhibiting passive film formation[177–180]. For the openly corroding samples, a similar breakdown of the oxides appears locally, as can be seen from the visual corrosive damage, which showed localized attacks. The fact that the dissolution current of Cr5 and alloy 600 was consistently higher compared to the electrochemical current (**Fig. 4.2d/e**) further supports that oxygen reduction (from aerated solutions) occurred simultaneously at the bare metal/solution interface, indicating a localized decomposition of the passive film.

In contrast, for Mo1 both the ICP-MS data and the XPS data presented here further confirm the formation of a passivating layer of fully oxidized molybdenum oxide at 0.2 V (see again XPS), which is still quite stable at 1.0 V. Both the increasing Mo dissolution over time during corrosion at 1.0 V (**Fig. 4.2f**), and the observed transient extended dissolution during repassivation (**Fig. 4.4f**) suggest a solution side based repassivation mechanisms (reprecipitation mechanism) of the passive film during corrosion and during step down into the passive region for Mo1. At different conditions, OGLE *et al.*[108] also observed Mo precipitation based on chemical molybdate dissolution after transpassive polarisation.

This is consistent with current interpretation of the effect of Mo. Precipitation of molybdates passivates the surface for an openly corroding system[108, 181, 182].

However, under crevice conditions, we clearly see a lower protective effect, and no pronounced precipitation of molybdates. XPS and ICP-MS data for crevice type samples indicate a lower oxide thickness and soluble molybdate species. Within the crevice region no highly oxidized molybdate based passive film can hence form, probably resulting from the acidification in the crevice and therefore increased solubility of the molybdates[108].

4.5 Conclusions

In conclusion, we can show that our sample design allows a comparative study of open and crevice type corrosion within the same ICP-MS flow cell. The communication of a crevice environment with the bulk electrolyte can be reproducibly tracked, providing insight into the crevice chemistry. Together with modelling, backtracking the exact chemistry and pH may become possible in the future.

Regarding the characterized systems, our findings are in line with the current understanding of NBA corrosion behaviour, and can be summarized as follows:

- During passivation the passive films are mainly consisting of Fe and Cr oxides, while Ni establishes a passive current by dissolution across the intact passive film.
- Under open corrosion we see a clear preferential dealloying of Ni at localized corroding areas.
- Consistent with ICP-MS dissolution currents, nanometer resolved XRF was utilized to confirm localized selective dissolution of Ni, and enrichment of the other alloying elements.
- The formation of a passive film with $>7-8\%$ MoO_3 confirmed a selective enrichment of Mo after corrosive dissolution and consequent repassivation for Mo1.

- In the crevice region oxides are thinner, and iron oxide enriches significantly, while the other alloying elements, including Cr, dissolve at higher rates and above bulk level concentration in the crevice.
- Under crevice condition Mo(VI) can hence not precipitate an effective protective layer, likely due to the low pH level that establishes in the crevice environment.

Chapter 5

Stability and quality study of passive films formed on Alloy 600 with in-situ AFM and EC-ICP-MS

In the following chapter EC-ICP-MS dissolution currents are compared with AFM topographies to form a complementary view on the formation and breaking of passive layers on Alloy 600.

Most AFM pictures shown in this chapter have been acquired in the course of a project work of Marina Bishara titled "In-situ Electrochemical AFM corrosion study of Nickel based alloy 600" under supervision of the author.

Understanding elemental corrosion currents and visualizing corroding topographies provide a detailed insight into corrosion mechanisms at the nano-scale. Here, we develop a strategy to understand the elemental composition, corrosion resistivity and local stability of passive materials. Specifically, we utilize a pulse voltammetry approach in a novel electrochemical AFM cell and complement this data by real-time dissolution currents based on spectro-

electrochemical online analysis in an ICP-MS flow cell. We study the oxide properties and their protective behaviour, when formed under different applied potentials using alloy 600 as model sample. Both AFM and ICP-MS data show that passive films formed on alloy 600 at around +0.3 to +0.4 V in neutral 1 mM NaCl solution are most stable during anodic corrosion at +1.0 V, while AFM further demonstrates that local dissolution occurs, indicating locally varying defect levels in the passive film. In combination of both techniques, our approach provides real-time elementally resolved and localized information of passive film quality under corrosive conditions, and it may prove useful for other corroding materials.

5.1 Introduction

Nickel-based alloys (NBAs) show outstanding corrosion resistance under many extreme environments enabling them to be used in broad applications such as steam reactors, aerospace and chemical processing[146, 183–186]. It is well-established that the unique corrosion resistance of NBAs such as alloy 600 can only be achieved when the chromium content is more than 10%[148, 149, 187, 188], which is necessary for the formation of a stable passive/chemically inert chromium oxide enriched thin film (typically 1-2 nm[189]) on the alloy surface. With their outstanding corrosion inhibition property, such thin films have attracted great attention from researchers[183, 190] to study their passivation mechanism, as well as to characterize their physical structure, chemical composition and electronic properties[191–193]. While alloy 600 is prone to pitting corrosion[179], under mild conditions passive film breakdown is considered to be the critical step[8] leading to corrosive failure. Hence, understanding the properties and anti-corrosion mechanism of the passive film are central for predicting corrosion tendency of NBAs in mild environments.

Up to now, the formation of passive films have been described using models such as the High Field Mechanism (HFM)[171], or the Point Defect Model (PDM)[194], which can be used to explain growth kinetics as well as their chemical composition.

These models suggest that changing the conditions under which the passive layer is formed can influence the formation kinetics that lead to grow distinct passive films, and therefore, result in varying corrosion resistance.

The passivity of the chromium oxide thin film is often understood as formation of a dense physical barrier that is limiting the permeability of ions across the film[16] or a change of the electronic structure (band gap) that creates a higher energy barrier for charge exchange at the interface[195]. It is easy to picture when growing passive films under different potentiostatic polarization, the created potential drop across the oxide film can result in a different degree of ion migration/permeability, which directly influences the passive film structure.

However, due to the nature of its extremely small film thickness, characterizing its physicochemical properties during a corrosive process remains challenging. Most of the surface sensitive analytical methods are *ex situ* techniques and very often require operating in specific environment such as under ultra high vacuum. In this aspect, obtained results from these techniques do not directly reflect on the *in situ* passive film composition and behaviour.

Consequently, techniques capable of performing real-time studies such as scanning probe techniques e.g. Atomic Force Microscopy (AFM) and Scanning Tunneling Microscopy (STM) are more suitable in studying actively corroding surfaces, which has increasingly gained more impact in recent years[46, 189, 196–198].

Most of the conducted research observed the growth behaviour of passive films e.g. during linear sweep voltammetry (LSV). In this perspective, the created oxide films are not well-defined and the composition may vary with the altering potential. I.e. properties of a passive oxide from a LSV may be influenced by the scan rate and applied solution conditions.

It is therefore crucial to develop a strategy to understand the elemental composition, corrosion resistivity and stability of oxide films that formed under *in situ* conditions. We considered passive films grown under constant polarisation as most controlled conditions to systematically study their behaviour. In this work, we utilize a pulse voltammetry approach in a novel EC-AFM cell (**Fig. 5.1 b, c**) as well as in a flow cell connected to an inductively coupled plasma mass spectroscopy

(ICP-MS) online analysis (inset in **Fig. 5.1 a**) to study the oxide properties and their protective behaviour, when formed under different applied potentials. Both techniques provide time-resolved information about the surface condition with the ICP-MS having the focus on elemental composition and the AFM providing topographic/structural information of the material during corrosive breakdown of alloy 600 as model system. Both AFM and ICP-MS data show that passive films formed at around +0.3 - +0.4 V in neutral 1 mM NaCl solution are most stable during anodic corrosion at +1.0 V, while AFM further demonstrates that local dissolution occurs, indicating locally varying defect levels in the passive film.

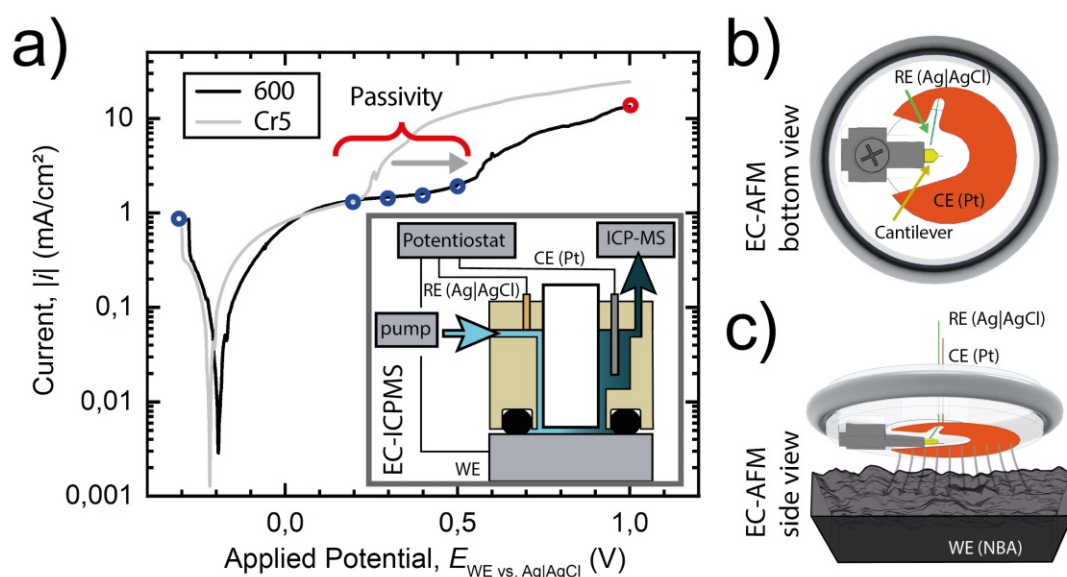


Figure 5.1: **a)** Tafel characteristic curve of the examined alloy: NBA 600 ($Ni_{72}Fe_8Cr_{15.5}$) and Cr5 ($Ni_{86}Fe_9Cr_5$) for comparison. The blue circles mark the regions of interest in this study. Inset shows a schematic of the home-designed ICP-MS coupled electrochemical flow cell. A stamp is used for establishing laminar flow across the surface of working electrode (WE, studied alloy). The counter electrode (CE, Pt) and reference electrode (RE, Ag|AgCl) are arranged in a way to avoid WE being contaminated by the reaction products from CE (hydronium or hydroxide that may vary the pH near WE surface). **b)** Design principle of the home-designed three-electrode system equipped AFM liquid cell, bottom view. A platinum foil forms the CE directly at the optical window of the used cantilever holder. Only a small section is left out for the AFM laser. Reference electrode (Ag|AgCl) is located outside the cell with a connecting tubing (green). **c)** Side view of the assembly with the sample (WE) at the bottom in parallel with the CE, resulting in a even electric field distribution.

5.2 Experimental Section

Chemicals and Materials. Sodium chloride (Carl Roth, p.a.) and Milli-Q water (resistivity $>18 \text{ M}\Omega \cdot \text{cm}$, total organic carbon $< 4 \text{ ppb}$) was used for making electrolyte solutions. Alloy 600 was obtained from VDM-Metals, Cr5 was provided by Hauke Springer (MPI f. Eisenforschung, Düsseldorf). The metals were ground with sand paper of decreasing grain size (from P80 to P2500), then polished with diamond paste down to $0.05 \mu\text{m}$. Prior to electrochemical experiments the metals were maximum 5 min *in situ* in the ICP-MS flow cell by 5 minutes potentiostatic polarization at -0.2V vs OCP.

Atomic Force Microscopy (AFM) AFM topographies were taken on with AM-mode Cypher ES (Asylum Research, Oxford Instruments, Santa Barbara, CA) using ArrowTM UHFAuD (NanoWorld, CH) and SCOUT 350 RAu (NuNano, UK) probes. blueDrive was used to oscillate the probes. Embedded NBA samples were contacted with silver glue. For embedded samples a rectangular piece of metal of about 5 mm side length was used. The block material was embedded in methylmethacrylate based VariDur 200 (Buehler). A PalmSens 4 potentiostat (PalmSens, Netherlands) was used.

Image processing Prior drift correction and further analysis images were only processed by applying flattening of first order. For alignment in z-direction a minimum of 10 line profiles were chosen per time-series and adapted in height to match significant - and non-changing - features of the images, e.g. deep scratches from polishing or distinct peak features that remain over time.

Cell design of the electrochemical AFM (EC-AFM) Our home-built electrochemical cell design (see schematics in **Fig. 5.1 b**) & **c**) is inspired by concepts of VALTINER *et al.*[53] and derives from a standard Perfusion Cantilever Holder (Asylum Research). We modified it by placing a platinum foil as a counter electrode (CE) at the bottom side of the cantilever holder. When assembled the working electrode (WE) and the platinum CE form a parallel plate geometry resulting in a very evenly distributed electrical field. A majority of the upper surface

is covered with the platinum foil to provide a high area, hence avoiding any rate limitation from reactions at the CE. Only the optical path for the laser of the AFM and a feed trough to connect the reference electrode remain cleared. A commercial silver/silver chloride reference electrode is connected with the cell via a capillary. For compensation of the expected high electrical current especially during anodic dissolution and given that the CE is in close vicinity to the sample a reduction of the WE size is limiting the possibility of disturbance through reactions happening at the CE (e.g. hydrogen evolution and bubble formation). The size ration of WE to CE is at least 5:1.

5.3 Results and Discussion

Corrosion resistance of NBA increases with increasing chromium content. Exemplary, a Tafel analysis shown in **Fig. 5.1 a)** for an NBA with 5% and 15.5% chromium concentration demonstrates the effect of chromium on the window of passivity. When comparing the polarization curves, alloy 600 exhibits a well defined region of passivity from -0.1 to +0.5 V shown as the flat plateau in the Tafel plot (indicated by grey arrow), whereas the Cr5 is showing an earlier break-down (light grey) around +0.2 V.

5.3.1 Results of ICP-MS experiments.

The linear polarization shown in **Fig. 5.1 a)** changes the passive film properties continuously, our interest is however to study potential dependent passive film properties and their protective characteristics. Hence, in order to approach the passive film formation under thermodynamic equilibrium, we introduced a multi-step chronoamperometry sequence (see inset figure of **Fig. 5.2 c)**) to perform step-wise surface oxide growth, corrosion resistance test and reconditioning as shown in **Fig. 5.2**. Specifically, freshly polished alloy 600 was first polarised at a passivation potential of $E_{(pre)cond}$ over 5 minutes for growing a passive layer. Subsequently, the polarization jumped to $E_{diss} = +1.0$ V for another 5 minutes for testing the corrosion resistance of the material after passive film formation at the given $E_{(pre)cond}$. At the end of the corrosion test, polarization switched back to

reconditioning at $E_{recond} = -0.3$ V for 2 minutes to remove the remaining surface oxides, which resets the alloys' surface chemical state for the coming repetition sequences.

This approach can therefore provide a clear insight into protective characteristics of passive films prepared under different electrochemical potentials. Based on the Tafel analysis shown in **Fig. 5.1 a)** we selected five potentials of interest: $E_{(pre)cond} = -0.3, +0.2, +0.3, +0.4$ and $+0.5$ V, where -0.3 V was chosen as reference region. There we expect no or only minor oxide film formation as it is located at the cathodic branch of the Tafel plot and as is estimated from Pourbaix diagrams.[199] The other potentials are well in the passive region.

We used ICP-MS and EC-AFM (see setup in **Fig. 5.1 b)** and **c)**) to identify the alloy's potential-dependent elemental dissolution tendency and surface morphology change, respectively. The advantage of such flow-cell coupled ICP-MS arrangement is that it provides online corrosion product analysis at trace levels, which can directly be correlated to the applied electrochemical polarization during a real-time process. In combination with EC-AFM, we may further understand local and micro structure effects.

Fig. 5.2 a) shows integrated dissolved mass of nickel, chromium and iron marked in blue, purple and red, respectively, from ICP-MS during polarization at $+1.0$ V averaged over four repetitions (see **Fig. 5.2 c)**). Among all the examined potentials, we surprisingly found that alloy 600 treated with passivation potentials around $+0.3$ V to $+0.4$ V shows a statistically relevant decrease in material loss during active corrosion at $+1.0$ V. Comparing to the amount of measured dissolved mass at $E_{(pre)cond} = -0.3$ V, where no passivation is expected, the passivity at $E_{(pre)cond} = +0.3$ V shows an expected reduction of the mass-loss by around 50 %. In the case of anodic dissolution of the metal surface after $E_{(pre)cond} = +0.5$ V, the measured dissolved mass at $+1.0$ V increased again compared to passivation at $+0.3$ V. Hence, the corrosion resistance of the passive film formed at this potential is again reduced, which agrees well with the observed passivity range and the increasing passive current in the Tafel plot.

Further examination of the ratios of dissolved mass surprisingly revealed that

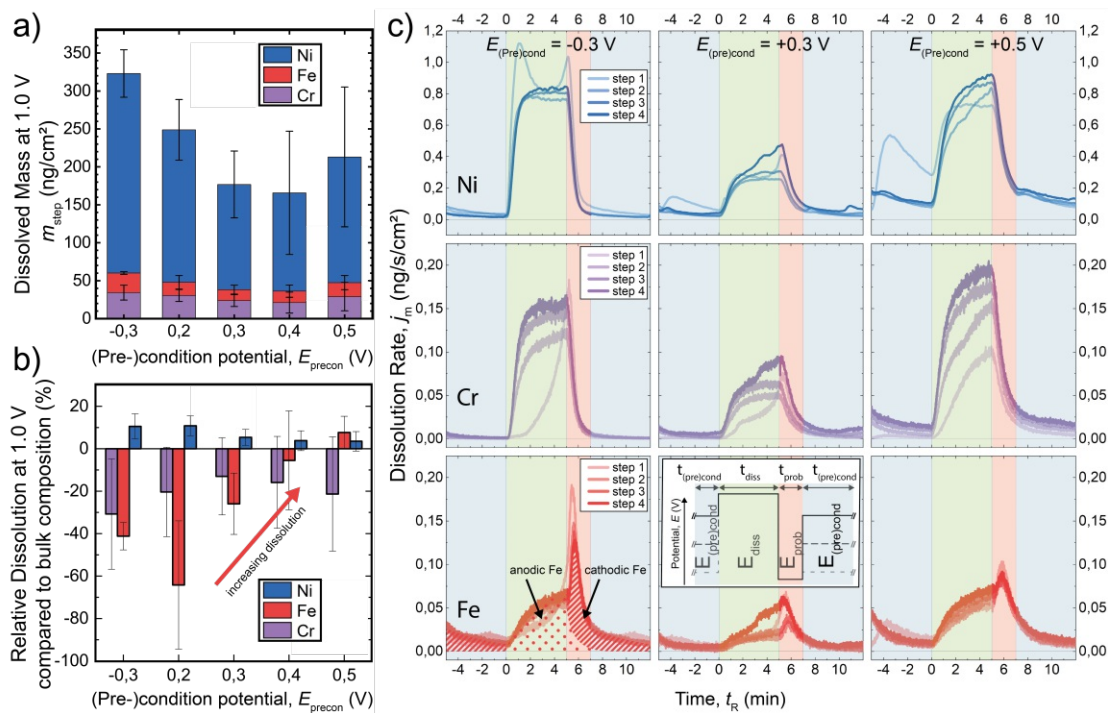


Figure 5.2: **a)** Integration of collected mass during corrosion at 1.0 V over the course of single sequences (4 pulse periods), resolved per elemental contribution. Error whiskers show standard deviation of value over three repetitions of the experiment with >4 pulse sequences. **b)** Relative dissolution during anodic polarization per element **c)** Overlap of 4 consecutive pulse periods of recorded ICP-MS mass-time profiles for all elements during one full sequence. Please note that the scale for nickel is about 1 order of magnitude higher. Inset shows the schematic of the designed applied electrochemical pulse profile in multi-step amperometry.

nickel, chromium and iron were demonstrating entirely different dissolution trends depending on the passivation potential. Specifically, **Fig. 5.2 b)** shows the relative elemental ratio of dissolved mass of individual alloy elements normalized by their bulk ratio, where zero, positive and negative values indicate equivalent, more and less dissolved mass compared to the bulk composition, respectively.

Comparing the trend of dissolution for the elements, nickel exhibited a higher dissolution rate compared to its bulk ratio at all passivation potentials, with a clear reduction by about 50% in the passive region above +0.3 V. This is also associated to the main reduction of the total mass loss observed in **Fig. 5.2 a)**. In contrast to nickel, chromium shows a weakly passivation potential-independent dissolution below bulk concentration. However, iron is showing a very clear passivation-dependent dissolution trend. Iron dissolved less compared to bulk ratio at lower potentials but gradually shifted into over-stoichiometric dissolution at higher passivation potential of +0.5 V.

The dissolution profile of iron shown in **Fig. 5.2 c)** reveals another key feature, which may be relevant for understanding the underlying mechanism: As indicated in the figure, the detected iron release exhibited a two-step mechanism - anodic dissolution at +1.0 V and cathodic dissolution when jumping from +1.0 V to -0.3 V, indicated by red dotted and shaded areas, respectively. This observation suggests that the iron in the passive film undergoes at least two types of dissolution mechanisms, occurring under different polarization potentials. Based on Pourbaix diagrams the detected iron species at anodic polarization potential of +1.0 V may originate from the release of ferrate anion (FeO_4^{2-}). The additional peak upon jumping cathodically back from +1.0 V to -0.3 V, indicates dissolution of a surface bound excess iron species formed during anodic corrosion.

In contrast to the two-step dissolution pattern of iron, nickel shows a well reproducible profile over several repetitions, which is characterised by a ~ 1 order of magnitude dissolution rate increase, above bulk ratio, at +1.0 V. Similar reproducibility of dissolution profiles is observed for Cr. For this element the first sequence in a repetitive set shows a delayed dissolution kinetic, which may relate to an effect of the initial native oxide, adapting to flow cell environment after the

first cycle.

5.3.2 Results of *in situ* EC-AFM surface morphology probing

Potential	RMS [nm] (relative to OCP)		
$E_{precon} =$	-0.3 V	+0.3 V	+0.5 V
OCP	0.83 (1.0)	2.32 (1.0)	3.05 (1.0)
precon	0.84 (1.0)	2.36 (1.0)	3.27 (1.1)
+1.0 V	2.37 (2.8)	2.57 (1.1)	4.12 (1.4)
-0.3 V	2.09 (2.5)	2.86 (1.2)	4.98 (1.6)

Table 5.1: Root mean square (RMS) values and their relative change of images shown in Fig. 5.3

To complement integral ICP-MS data, we further visualised the (local) evolution of the surface morphology upon passivisation using electrochemically modulated AFM measurements.

Fig. 5.3 a) shows representative real-time changes in surface topography of alloy 600 during corrosion after different conditioning potentials $E_{(pre)cond}$ where applied (similar to ICP-MS). The red dashed lines indicated in the OCP (open circuit potential) topograms show line profiles that are compared in **Fig. 5.3 b)**, for $E_{(pre)cond}$ (blue), $E_{diss} = +1.0$ V (green) and $E_{prob} = -0.3$ V (red), respectively.

As a side note, for better visualisation height changes were overlaid on the recorded images. Increase in height is indicated by green shading, while dissolution from the surface is shown in magenta. Further, AFM topography does not provide information of absolute but only relative heights. Hence, consecutively measured topographies were shifted during post-processing, using a referencing protocol described in the methods section, in order to approximate the absolute change in topography during corrosion. The selected images summarise recurring patterns and characteristics seen in repeat experiments.

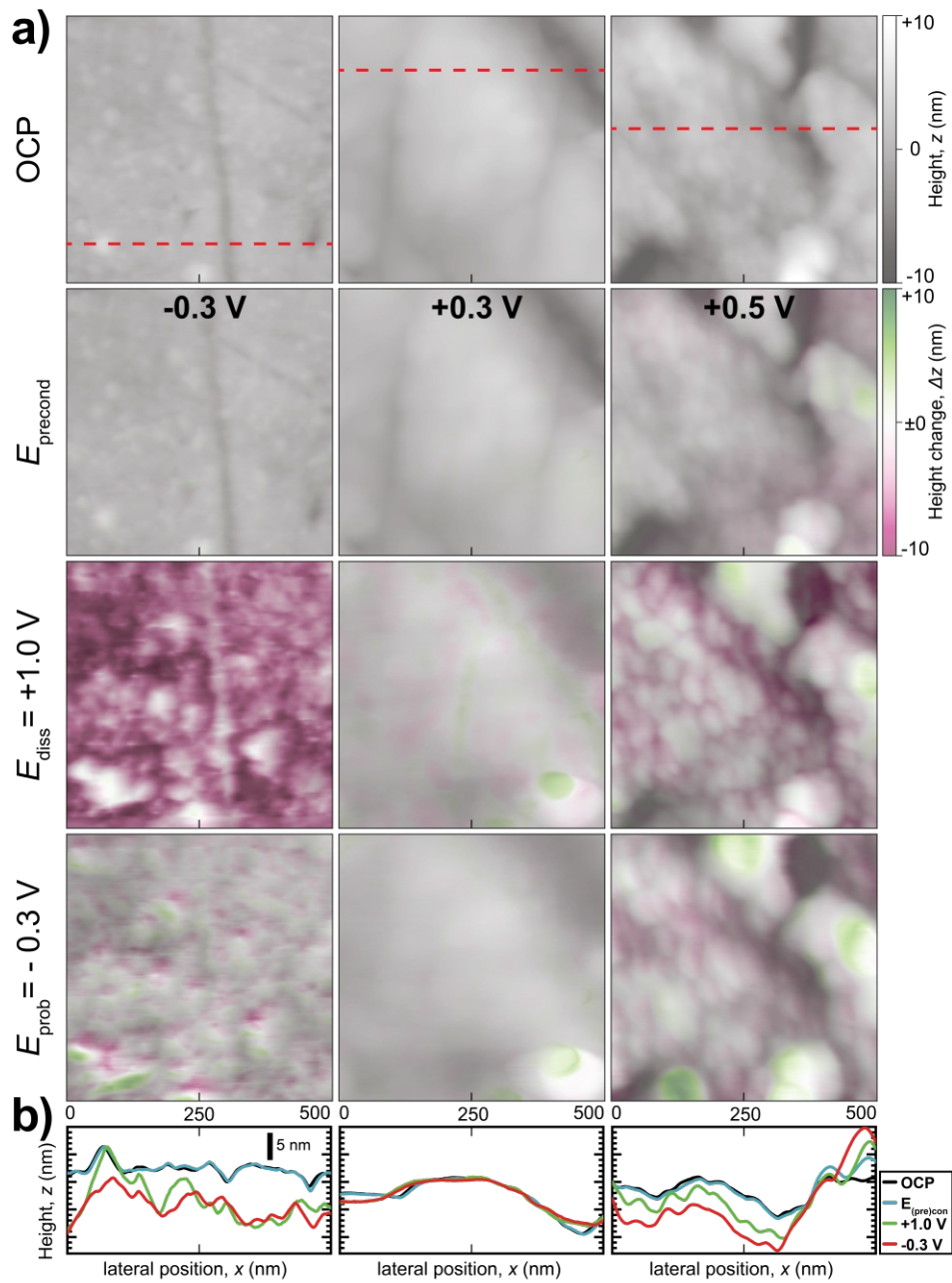


Figure 5.3: AFM topography during different stages ($E_{(pre)cond}$, E_{diss} , E_{prob}) of multiple step voltammetry with different (pre-)conditioning potentials $E_{(pre)cond} = -0.3$, $+0.3$ and $+0.5$ V. Red dashed lines indicate the position of the line sections shown in b). RMS of each picture and relative change compared to the initial OCP-topography can be found in Tab. 5.1.

The potential-dependent EC-AFM images reveal a number of interesting details as described in the following.

First, during the passive film formation (preconditioning) the surface morphology of all three examined precondition potentials show no significant changes compared to OCP. Only very minor height variations are observed. Jumping from precondition potential to dissolution potential, the alloy treated at $E_{(pre)cond} = -0.3$ V shows a very vigorous dissolution. The RMS roughness increases significantly (see **Tab. 5.1**), and most of the pronounced features (polishing scratches, etc.) become indistinguishable, while only few areas remained stable for referencing the corrosive height loss.

Second, and in a sharp contrast, the surface morphology during anodic corrosion has no significant change when the passive film was grown under polarization of +0.3 V. Obviously, the surface oxide film does protect the surface very effectively, and dissolution occurs homogeneously along preexisting features such as scratches.

Third, surfaces passivated at +0.5 V again show more pronounced corrosive degradation at +1.0 V. Here, the surface morphology did not undergo a similarly massive dissolution as seen for preconditioning at -0.3 V. However, significant dissolution preferentially occurred along the edges of the nano-granular features. Additionally, in some areas measurable material growth was observed, indicating possible local re-precipitation reactions.

Fourth, upon switching the polarization from +1.0 V to -0.3 V, the dissolution reactions stopped and only minor topographic changes were observed for preconditioning at +0.3 V and +0.5 V. However, for samples pretreated at -0.3 V dissolution was still observed at the top of particles. This correlates well with the observed significant cathodic iron dissolution peak (see **Fig. 5.2c**), which further supports that the surface enriches in iron oxide during active corrosion, if corrosion starts without a significant passive film presence.

5.3.3 Overall discussion of results

In summary, the AFM topography analysis agrees very well with the ICP-MS online analysis results, which reveals that the passivation potential, i.e. the conditions during passive film formation are directly influencing the behaviour during active corrosion. Together with the transition of the ICP-MS dissolution pattern our data suggests that the quantitative elemental dissolution during active corrosion is highly dependent on the passive film properties. In the following, we want to discuss several interesting aspects of our data.

First, if the material is directly corroded after polarization at -0.3 V, ICP-MS and AFM data suggested a massive material loss. Given the Pourbaix diagram, one may expect a pure chromium oxide layer, as the most stable chromium phase is chromium oxide at -0.3 V at the experimental pH. Further, the passive film might be much thinner, or even defect rich, or not complete. As a consequence, any protective effect is limited or not even present.

Second, in line with this thought we find clear and pronounced cathodic iron dissolution only after corrosion starting directly from -0.3 V. This suggests that a steady state surface film evolves during anodic breakdown, which is significantly enriched in iron, and presumably iron oxide. This is consistent with the Pourbaix diagram suggesting that Chromium oxide is not stable at corrosive conditions at 1.0 V. Our data may hence indicate that iron oxide forms as a transient oxide during corrosion, which is specifically growing at defects or areas that are not covered by a stable chromium oxide. Further, during corrosion, this oxide is not sufficient to suppress the material loss as effectively as a proper passive film grown at passivation potentials within the passive region. This iron oxide enrichment is evident from the significant iron dissolution peak during repassivation, after corrosion at 1.0 V.

Third, and along the same line, passivation at $\geq +0.3$ V establishes a passive film, which can significantly decrease the material loss during active corrosion. Still, we find a small but detectable cathodic iron peak after active corrosion. This may suggest that the passive film breaks down locally, presumably at defect rich sites, and/or iron oxide accumulates at the outside of the passivating chromium

oxide.

Considering the AFM data at +0.3 V, which shows a rather uniform material loss at defect rich areas (i.e. preexisting polishing defects, etc.), our findings appear more consistent with an increased iron dissolution across the defect rich areas of the passive film. Further, as seen in **Fig. 5.2b**) relative iron dissolution also increases significantly if a passive film is grown between +0.3 - 0.5 V. Hence, iron may accumulate at the oxide|water interface and/or gets transported through the passive film at a higher ratio during corrosive dissolution. This suggests a change in the passive film chemistry.

Fourth, after passivation at +0.5 V the again increasing iron content during cathodic polarization after corrosion, suggests a decisive role of defect levels on the transport across the passive film during corrosion. As such, the growth conditions apparently render the passive film with different defect levels. Together with the increase in iron ratio during corrosion (see again **Fig. 5.2b**)) this suggest a structural change in the oxide that accelerated iron diffusion across the existing passive film in a high-field condition applied during corrosion at +1.0 V. This is further supported by AFM, where we see increased dissolution at areas that are defect rich. The high field model (HFM)[171, 195] describing the built up of the passive film during $E_{(pre)cond}$ provides an explanation for the differences in density of defects, and hence, corrosion resistance.

Also, during the cathodic jump AFM data at +0.5 V shows further material loss at the preexisting grain boundaries. The passive film grown at +0.5 V may hence trigger faster oxide growth, due to an increase of defect rich areas, as indicated by the localised loss seen in AFM topography.

We refrain from interpreting too much into the apparent material growth areas at this point in time, as AFM is not an absolute technique, and post-processing shifts may not truly reflect any growth areas, while material loss is clearly distinguishable. Along this line, one important aspect to consider when comparing the processes observed in both the AFM and the ICP-MS flow cell is their general differences: While the ICP-MS requires a constant flow of electrolyte the AFM measurements are conducted in a stagnant solution. Quantitative comparison also

indicates that corrosion is more severe in AFM, where for instance after preconditioning at +0.3 V a few nm of material are lost during corrosion at 1.0 V, while ICP-MS indicates only a monolayer material loss per cycle ($300 \text{ ng/cm}^2 \cong 0.35 \text{ nm}$). This discrepancy is considerably lower when the material corrodes less.

Hence, the dissolution in AFM is also accelerated due to typical surface confinement in an AFM (typically the AFM cantilever holder is separated by less than $200 \mu\text{m}$ from the probed surfaces), which renders this experiment more effectively "crevice like", where electrolyte of the dissolving species may render the interface at a different pH. This needs to be considered for AFM and scanning probe techniques in general when studying corrosion, and may become a feature, if properly controlled. How scanning probe conditions can even compare to flow-cell experiments, and other electrochemical cells, is in our view an aspect that will need further attention, e.g. by directly coupling AFM and ICP-MS, and by further comparative studies with model systems.

5.4 Conclusions

In this work, we successfully used two complementary analytical techniques to study the influence of passivation potential on the formed metal oxide film quality in real-time. We designed an AFM cell that performs very well during corrosion. The, for scanning probe techniques, novel plate-plate geometry provides an idealized field distribution. Using an ICP-MS flow cell and EC-AFM, passivation and anodic dissolution was tracked with both time resolved elemental dissolution rates during chronoamperometric pulse experiments and complementary changes in morphology, respectively. Regarding the characterised passivation potentials on alloy 600 we could find an optimum at around +0.3 - +0.4 V in neutral NaCl solution exhibiting lowest dissolution and therefore forming the most stable passive film during anodic corrosion at +1.0 V.

Our results suggest the following specific conclusions:

- Quality of the passive film depends on the potential at which it is grown.
- The passivation potential controls the defect density and ion-conducting

properties of the passive film during active corrosion.

- Combination of *in situ* techniques provide information about stability, indirectly composition and local stability of the passive film.

With the ICP-MS flow cell and the EC-AFM it is hence possible to relate two *in situ* techniques to consistently describe the quality and stability of a passive film. In combination both techniques provide real-time and localized information under operating conditions, and are much closer to realistic corrosion conditions, compared to other surface sensitive analytical methods.

Chapter 6

Complementary electrochemical ICP-MS flow cell and in-situ AFM study of the anodic desorption of molecular adhesion promoters

This chapter is based on the manuscript with the same title submitted to Applied Surface Science. The methods ICP-MS and EC-AFM are now also extended on the studying of organic coatings at the solid|liquid interface. Surface Preparation and ICP-MS measurements of the present chapter were conducted in the course of the Master thesis of Carina Brunnhofer titled "Method development for characterizing corrosion and corrosion protection using an electrochemical ICP-MS flow cell approach". This work was supervised by Dr. Hsiu-Wei Chang along with the author of the present thesis.

Molecular adhesion promoters are a central component of modern coating systems for the corrosion protection of structural materials. They are interface active and form ultrathin corrosion inhibiting and adhesion-promoting

layers. Here we utilize thiol-based self-assembled monolayers (SAMs) as model system for demonstrating a comprehensive combinatorial approach to understand molecular level corrosion protection mechanisms under anodic polarization. Specifically, we compare hydrophilic 11-Mercapto-1-undecanol and hydrophobic 1-Undecanethiol SAMs and their gold-dissolution inhibiting properties. We can show that the intermolecular forces (hydrophobic vs hydrophilic effects) control how SAM layers perform under oxidative conditions. Specifically, using *in situ* electrochemical AFM and a scanning-flow cell coupled to an ICP-MS a complementary view on both corrosion resistance, as well as on changes in surface morphology/adhesion of the SAM is possible. Protection from oxidative dissolution is higher with hydrophobic SAMs, which detach under micelle formation, while the hydrophilic SAM exhibits lower protective effects on gold dissolution rates, although it stays intact as highly mobile layer under anodic polarization. The developed multi-technique approach will prove useful for studying the interfacial activity and corrosion suppression mechanism of inhibiting molecules on other metals and alloys.

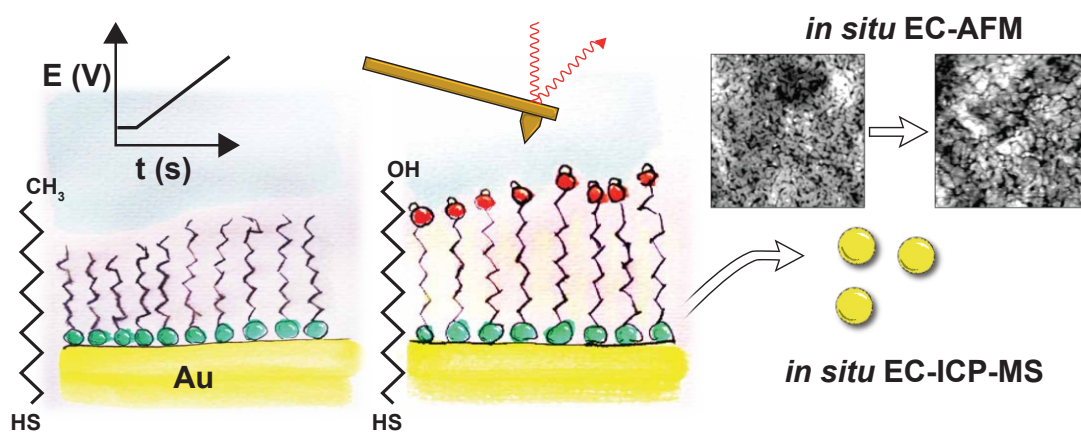


Figure 6.1: Testing of self assembled monolayers (SAMs) for corrosion inhibition with EC-AFM and ICP-MS electrochemical flow cells

6.1 Introduction

Organic coatings are widely used as corrosion protecting layers on metals[200]. Coatings protect from corrosion by a physical barrier effect for water between the metal and its surrounding, and are therefore up to a few micrometer in thickness[16]. Still, the most crucial part of the coating is at the boundary of the organic top coating with the metal(oxide) underneath[201]. Additionally, molecules such as silanes, or phosphonates[202] which can form self assembling molecular thin films/ monolayers (SAM) at an interface, are typical reactive additives for coating formulations. Specifically, SAMs have been proven to be suitable as molecular adhesion promoters for long-term corrosion protection[203]. Further, the covalent character of the head-group to metal(oxide) bond stabilizes as a linking layer between the metal(oxide) and the further covalent attachment of polymer layers on metallic substrates.

In particular, the system of gold and thiol-based self-assembled monolayers (SAMs) is well studied as model system due to its ease of preparation, stability and quality of the layers[204, 205]. For thiol-based SAMs the bond strength[206] between the sulfur of the thiol and the gold determines the stability of the formed monolayer. Potential dependent SAM formation has been measured *ex situ* with Scanning tunneling microscopy (STM)[203], but not yet under operating conditions at oxidative/anodic potentials. Further, weakening of the bond for removal of the formed SAM by cathodic desorption (stripping) is a well established process[207–211].

Though electrochemical anodic detachment already finds application in formation of mixed SAM layers by partial electrochemically induced desorption of a SAM in a thiol solution[212], the oxidative desorption on the contrary is less studied[213].

Further, polarization of the surface can enhance the adsorption kinetics of molecular thin films[207]. How molecular adhesion promoters act, and to which degree they suppress metal dissolution. When the underlying substrate is electrochemically polarized into anodic polarization is still unclear.

In recent years, elementally resolved electrochemical techniques such as combinations of flow cells with downstream inductively coupled plasma mass spectrometry (ICP-MS) or optical emission spectrometry (ICP-OES) analysis, proved to be useful for understanding molecular dissolution mechanisms at electroactive interfaces[13, 92, 109, 110]. These techniques have been applied to study the dissolution of Zn coatings on steel[95, 214], the dissolution of electrocatalysts under operating conditions[90, 109], or to the study of the potential dependent stability of photo-electrocatalytic materials[17, 110]. Here, we extend this technique to understand corrosion inhibiting effects of molecular adhesion promoters under anodic polarization, as a model system for more complex alloys and inhibitors.

Specifically, we report results on the *in situ* anodic polarization of SAM covered gold in sodium perchlorate solution. We compare Linear Sweep Voltammetry in hand with *in situ* electrochemical topography scanning with an atomic force microscope (EC-AFM) and elementally resolved ICP-MS dissolution currents of hydrophobic and hydrophilic SAMs. We demonstrated a significant corrosion-inhibiting effect of SAMs at anodic potentials, and show how interfacial hydrophobic forces can result in a micelle formation at the interface. This comprehensive approach combines complementary interface sensitive techniques for providing a detailed insight into molecular level protection mechanisms of molecular adhesion promoters during anodic polarization.

6.2 Experimental Section

Chemicals and Sample preparation

Electrolyte solutions were prepared from $NaClO_4$ (98%, Alfa Aesar) and Milli-Q water (resistivity $>18\text{ M}\Omega\cdot\text{cm}$, total organic carbon $< 4\text{ ppb}$). 11-Mercapto-1-undecanol (97%, Sigma Aldrich), 1-Undecanthiol (98%, Sigma Aldrich) were diluted to 1 mM solutions in Ethanol (chromatography grade, Carl Roth) for coating of the substrates. Molecularly smooth gold surfaces of 70-100 nm thickness were prepared by template stripping from mica using an established protocol[215, 216]. Samples are contacted with 0.125 mm diameter gold wire (99.99%, Goodfellow

Cambridge Ltd.), and immersed for min. 12 h in ethanolic SAM solution. To remove excess thiols surfaces are rinsed thoroughly with ethanol, hexane and ethanol and dried with a gentle N_2 stream.

Atomic Force Microscopy

AFM topographies were taken with a Cypher ES (Asylum Research, Oxford Instruments, Santa Barbara, US) using ArrowTM UHF AuD (NanoWorld, CH) and SCOUT 350 RAu (NuNano, GB) probes. Photothermal excitation is used with amplitude modulation (blueDrive) as driving mode. The electrochemical cell is a home-built modification with a platinum foil as a counter electrode and the reference electrode being connected via a capillary to the enclosed cell.

Electrochemistry

A Biologic VSP-300 potentiostat (Biologic, France) or a PalmSens 4 (PalmSens BV, NL) were used for electrochemical measurements. All electrochemical experiments were performed with a Ag|AgCl-Electrode (Multichannel Systems, DE) as reference electrode. All presented data is referenced to that potential. Platinum is forming the counter electrode. Freshly prepared SAMs on gold are - after a short equilibrating time in the electrolyte (10 mM $NaClO_4$ for AFM, 100 mM for ICP-MS) - polarized from 0.0 to 1.5 V vs. Ag|AgCl with a scan rate of 5 mV/s.

6.3 Results and Discussion

In this work we experimentally characterized the corrosion inhibition properties of hydrophilic and hydrophobic self-assembled monolayers (SAMs) on gold under potential control. As shown in **Fig. 6.2**, we selected a hydrophobic and a hydrophilic head group termination, in order to study the effect of the wettability of the substrate.

Therefore, the used SAMs are characterized by their same length of the hydrocarbon chain, but a major difference in interaction with water due to the selected head group. *11-Mercapto-1-undecanol* (OH-SAM) with its hydroxyl-terminated

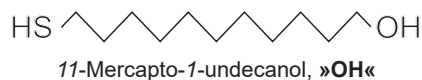


Figure 6.2: Thiols used for self-assembled monolayer films

tail is hydrophilic, whereas 1-Undecanethiol (CH₃-SAM) creates a hydrophobic layer on the gold. As Fig. 6.3 A₁ & B₁ show, the preparation produced - as expected from literature[208, 217–219] - an uniform and smooth film with typical defect patterns at domain boundaries of the formed SAMs.

These SAMs were consequently anodically polarized to 1.5 V in order to characterize their corrosion inhibiting behaviour during anodic polarization using Linear Sweep Voltammetry (LSV). The data was further complemented by *in situ* and *ex situ* AFM topography scanning, as well as by online ICP-MS flow cell analysis of the anodically dissolving gold. The results of these analyses can be summarized as follows:

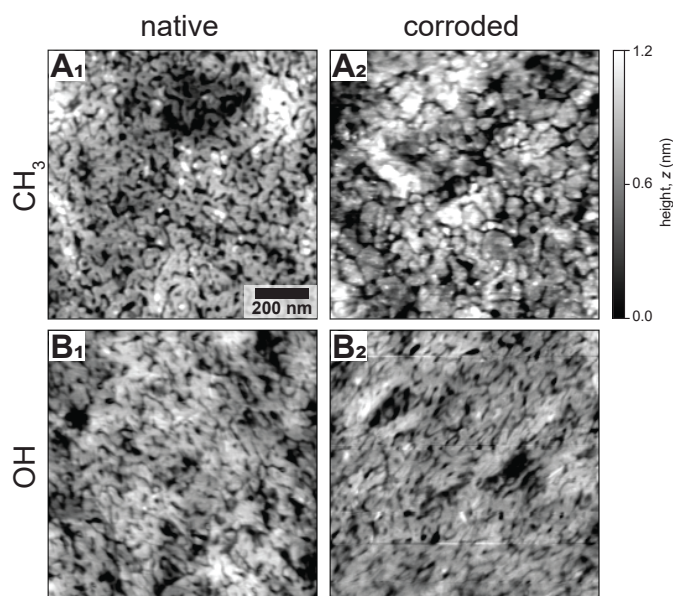


Figure 6.3: *Ex situ* AFM topographies of self assembled monolayers on gold before (1) and after (2) polarisation to 1.5 V for CH₃- (A) and OH- (B) SAMs.

First, *ex situ* topographies (**Fig. 6.3**) compare the initial conditions of the surfaces modified with the respective SAMs (indicated by subscript ₁) with a topography after polarization. For the hydrophobic CH_3 -SAM the surface after polarization (A_2) shows two topographic features, which are (1) globular residues likely formed by disintegrated SAM, as well as (2) nano-scaled grains as expected for a neat template stripped gold surface. This behaviour suggests that the CH_3 -SAM disintegrates completely during anodic oxidation. In contrast, the hydrophilic SAM still shows similar structures before and after polarisation, indicating an almost unaltered and likely intact SAM.

Hence, the head group directly determines how the SAM behaves during polarization. It appears likely, that the thiol|gold bond is weakened by the growth of an underlying oxide film, which in turn can cause a disintegration of the hydrophobic SAM. This disintegration can be driven by the head group effect as follows: Weakening of the surface bond can trigger the formation of bilayer structures, or can even drive micelle/particle formation as observed for weak binding of phosphonate SAMs on alumina [202], if the hydrophobic interaction of the head groups overpowers the thiol|gold binding. In contrast, if the SAM molecules are terminated by hydrophilic head groups there is no direct driving force for a disintegration of the SAM, and the intramolecular hydrophobic interactions within the SAM can withstand the "rolling up"/ lift-off of the SAM. As such, for the OH -SAM, the weakening of the thiol bond may result in a "flying carpet like" situation during anodic polarization.

To further support this interpretation, we performed *in situ* AFM under potential control. **Fig. 6.4** shows an image of the representative scan, when a significant change of the surface topography was observed during anodic polarization. More topographies of the changing surfaces can be found in the appendix **Fig. A.4.1**.

In detail, the hydrophobic SAM (**Fig. 6.4 A**) is showing a roughening of the surface starting at 0.75 V, in terms of formation of particulate residues (marked by arrows in figure). This is consistent with the interpretation of a weakening of the thiol|gold bond and a consequent triggering of a SAM lift-off due to formation

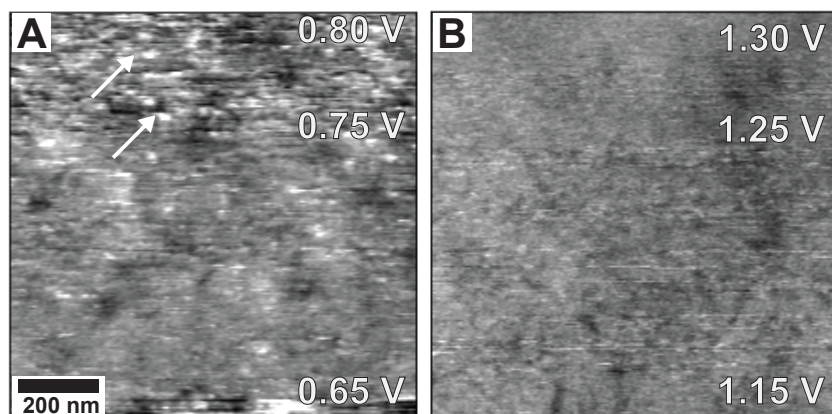


Figure 6.4: *In situ* AFM topographies of A) CH_3 - and B) OH -SAM on gold during linear polarization.

of micellar structures, which is driven by the hydrophobicity of the molecules. The roughening of the CH_3 -SAM hence indicates the initial detachment of the thiols accompanied by micelle formation. In contrast, the hydrophilic SAM appears intact up to more than 1.2 V where we see considerable flattening of the surface. This flattening is indicative of a lift-off of the SAM as a "flying carpet", i.e. the thiol-gold bond is weakening, and as a result a more mobile, less defect rich SAM structure forms, and does also not impregnate the underlying granular structure of the gold. As seen in the *ex situ* data (see again **Fig. 6.3 B₂**) the SAM remains then intact and reforms after polarization, without lifting off from the surface.

Based on this nanoscopic understanding of the SAM behaviour during polarisation we performed additional *in situ* spectroelectrochemical analysis [92, 109, 110], to understand how these SAM structures inhibit or enhance gold dissolution during oxidative polarization.

Fig. 6.5 shows (a) the measured current during electrochemical polarization as well as (b) the elementally resolved dissolution current of the gold dissolution (ICP-MS) displayed as a function of the linearly increasing potential. For both, data of more than 8 independent measurements are compiled for each SAM sample (OH and CH_3) and are further compared to the data obtained for bare gold. For the elemental dissolution current (ICP-MS) shown in panel **B** the observed range

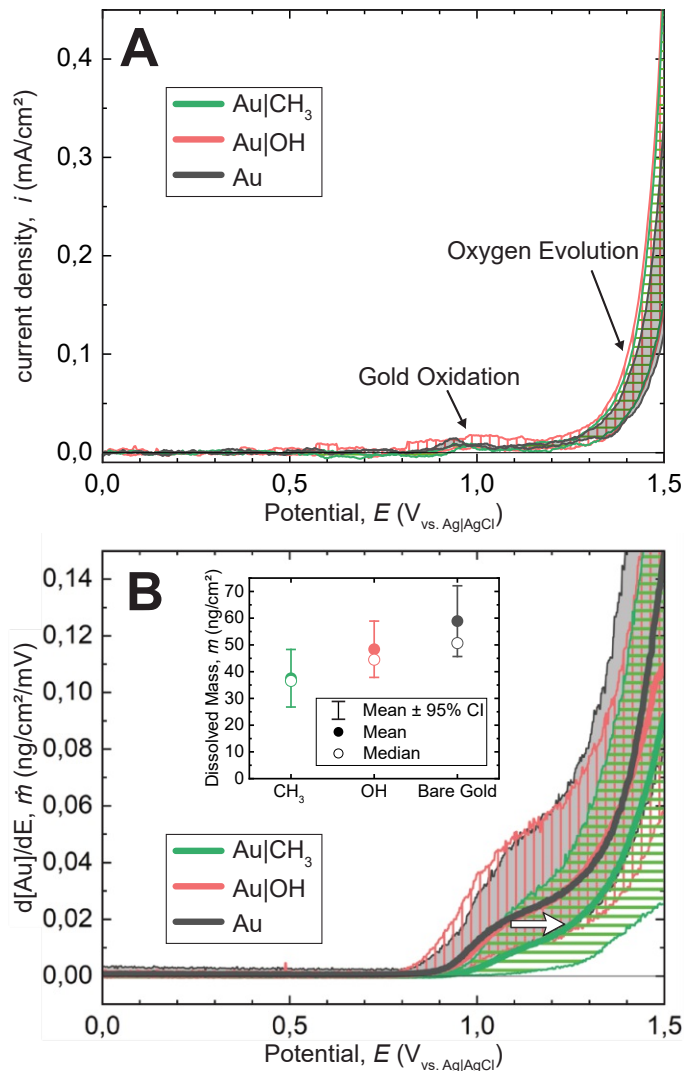


Figure 6.5: Linear Sweep Voltammetry (LSV) of bare gold (black), gold covered with a hydrophilic (red) and hydrophobic (green) self-assembled monolayer. Shaded areas indicate the range of observed dissolution profiles over at least nine experiments. **A**) Electrochemical Polarization Curves. **B**) Dissolved Gold during LSV. Solid lines represent the average curves over all of one type. Inset shows total integrated dissolved mass of gold during LSV, whiskers indicate the confidence interval (CI) of 95%.

(shaded areas) as well as the mean dissolution current are displayed (solid lines). For the current two examples are shown, as less variation is observed.

The electrochemical current shown and marked in panel **A** indicates the initial gold oxidation at the expected potential, as well as the increasing current at higher polarizations due to water splitting. Statistically, there is no large difference in the absolute observed currents.

However, the ICP-MS dissolution currents of gold exhibit clear changes, and an inhibition of the anodic dissolution of gold for the CH_3 -SAM and the OH -SAM (shown in **Fig. 6.5 B**) compared to unmodified gold is obvious. In detail, both SAMs statistically shift the onset of rapid gold dissolution to higher potentials. It is worth noting that the recorded dissolution rates show a significant variation although preparation remains the same, indicating an influence of defects formed during SAM formation. Nonetheless, statistical trends hold over a large set of >8 experiments for each sample.

All of the curves have in common a two-step dissolution profile with a small shoulder of comparatively little dissolution starting with the gold oxidation, followed by a steep increase in amount of gold released to solution during water splitting. Previous work by Cherevko et al. [109] traced this behaviour back to initial small dissolution from formation of gold oxide and later on more drastic degradation during water splitting, which is consistent with our data of SAM coated substrates.

The inset in **Fig. 6.5 B** shows the integrated amount of dissolved gold, further confirming this trend. Dissolution for all of the systems tested correspond to only a fraction of a single layer of gold which would result in a total of $\approx 450 \text{ ng/cm}^2$ gold dissolution. As expected the uncoated gold shows the highest dissolved mass, OH - as well as CH_3 -SAM modified gold show a decreasing trend to about 30% lower overall gold dissolution. The SAM coating can hence significantly suppress gold dissolution, likely by a barrier effects, and potentially also by stabilisation of the surface atoms at the SAM|oxide interface.

Surprisingly, the least gold is released from the CH_3 -coated surface, although the SAM lift-off is observed at the lowest potentials in AFM and the SAM indicates

a significant roughening. Further, looking at the ranges of dissolution recorded (indicated by the shaded areas) the hydrophobic SAM (green) clearly shows an onset of gold dissolution at higher potentials compared to hydrophilized and bare gold. Bare gold and *OH* coated gold overlap over most of the potentials, just for very high potentials at above 1.4 V gold with *OH*-SAM seems to be slightly less dissolving. The average dissolution curve for the *CH*₃-SAM rises later and for the whole potential range stays well below the dissolution rates of the other systems tested. As such, and in agreement with our interpretation, the hydrophobic *CH*₃-SAM may form micelles, which may lead to a trapping of gold within micelles, hence lowering the total dissolved ion count initially. This initial low count is followed by the steepest rise of the dissolution, at higher potentials, where trapped micelles may desorb.

This is an interesting behaviour, which we can interpret as a potentially important fundamental step during technical processes such as interphase formation during polymer coating (gluing/ coating for corrosion protection, etc.) of a metal in an oxidative environment. Interphases are considered boundary layers of a metal|polymer interphase where it has been speculated that metal ions dissolve and stabilize into the polymer matrix due to their interaction with the functional groups of the polymer. Our data demonstrates that such a metal dissolution mechanism is possible, and appears to be favoured by intermolecular interactions that drive micelle formation, or in other words the enclosure of metal ions in an functional organic matrix that is in contact with the metal during oxidation.

6.4 Conclusions

We successfully compared AFM imaging and ICP-MS flow cell studies of the anodic detachment of protective thin films on gold. We demonstrate their corrosion-inhibiting effect at anodic potentials. The morphological changes of two SAMs (11-Mercapto-1-undecanol and 11-Undecanethiol) on gold during anodic polarization show a strong effect of the head group in *in situ* AFM. Quantification of the dissolved gold with a scanning-flow cell coupled to an ICP-MS certainly adds information gain to the pure electrochemical data and might prove useful for the

study of further coatings on metals.

Our results suggest the following specific conclusions:

- Hydrophobic molecules may immobilize dissolving metal ions in micelles, which may enclose metallic (or oxidic) nanoparticles formed during anodic oxidation.
- During this process the SAM disintegrates and dewetting from the oxidized gold interface occurs.
- This data may show initial fundamental steps which occur during interphase formation when a coating or glue is applied to a metallic substrate.
- Hydrophilic molecules tend to not detach, but form a weakly adhering and highly mobile layer without significant micelle formation. This results in lower initial retardation of metal dissolution.

This combinatorial multi-technique approach will prove useful for studying the interfacial activity and corrosion suppression mechanism of inhibiting molecules on other metals and alloys.

Chapter 7

Bottom-up Characterization of Metal-Metal Interaction from Simple Binary alloys to High Entropy Alloys

A material library with alloys containing Ni, Co, Cr, Fe and Mn was characterized for their passive film stability and the single contributions of the elements.

Multi-principal element alloys (MPEAs) are an emerging class of metallic alloys with the capability of customized unique material properties. A high corrosion resistance is an intended characteristic for structural alloys, for traditional alloys usually achieved by the addition of e.g. Ni or Cr. For MPEAs the interplay of alloying elements on the corrosion resistance of the resulting material is less clear. Here we demonstrate a bottom-up systematic approach to study the electrochemical activity of a library of alloys spanning from equimolar binary alloys up to the High Entropy Alloy (HEA) NiCoCrFeMn. Using this approach we can show that chromium oxide does not form an effective passive film at potentials over 1.2 V, where Fe replaces Cr as passivation element. Further, Cr does not generally result in a stable

passive film, addition of Mn can significantly weaken the passivity. This and our approach provides useful insight for developing new MPEAs with simultaneously tailored corrosion resistance and mechanical properties.

7.1 Introduction

Fundamental metal-metal interactions govern physics, chemical reactions as well as mechanical performance of alloys. Properties of alloys/metal oxides can be tailored towards specific applications by using an increasing number of functional elements and tuning their composition. Newly emerged material classes as high entropy alloys (HEAs)[220–222], high entropy oxides (HEOs)[223–225] and superconductors[226] provide a variety of such possibilities. However, the drastic growth of material complexity creates new problems for design engineering, where the overall material behaviour is simply not a linear superposition of individual compositing elements[227].

In many alloy design strategies, corrosion resistance under extreme environments is a highly desirable property in a wide range of applications that is usually achieved by the addition of e.g. Cr. A critical concentration of Cr in an alloy is believed to be the key to reinforce the corrosion resistance of the alloy. It is suggested that more than 5% of Cr content is needed in an alloy to be highly corrosion-resistant, such as for nickel-based alloys (NBAs)[148–151].

However this general rule seems to be only valid for conventional alloys with the simple composition of one main and several co-alloyed minor components, such as NBAs or stainless steels. For more complex materials like multi-principal element alloys (MPEAs) and high entropy alloys (HEAs), the corrosion resistance built up by Cr might not be correlated to its stoichiometry anymore. Particularly, this effect gets even more pronounced when looking at HEAs, where more than five principal components come in play[228].

NiCoCrFeMn, as an example, is a well-known HEA containing Ni, Cr and Fe alike NBAs or stainless steels. Based on the experience with NBAs, over 20% Cr content

in NiCoCrFeMn should provide considerable corrosion resistance. Addition of Co and Mn can further provide flexibility in tuning the mechanical performance[229] as well as its electric conductivity[230]. However, it has been shown that the corrosion resistance of NiCoCrFeMn deviates from the prediction. It is considerably deteriorated compared to 304 stainless steel in aqueous 3.5 w.t.% NaCl, even though the Cr content is higher[231, 232]. This observation indicates the passivity constructed from Cr is weakened by other added principal metals. Therefore, it is crucial to understand the electrochemical correlation across different alloyed functional elements.

The addition of single elements to an otherwise static system is done in a series of studies: Mn has been shown to have a deleterious effect on similar HEAs by a recent study of Panindre et al.[233]. Increasing the concentrations of Co has been shown to improve passivity and lower the corrosion rate of Mn-containing steels in sulfuric acid[234]. These findings point out that the alloy composition and the consequential passive film is more critical than the amount of added Cr to its corrosion properties. Generally speaking, the concepts of passivity constructed by single functional element are valid for simple alloys, but may not be directly applied to MPEAs[235].

To decipher the influence of single alloyed elements as well as the synergy of combination on the electrochemical performance of MPEAs - in our case the corrosion resistance - a material library is capable to provide a large spectrum of property change of different combinations[236, 237].

In this work, we designed a bottom-up approach with studying the electrochemical activity starting from simple equimolar binary nickel based alloy: NiCo, NiMn, NiCr and NiFe to step-by-step constructing three (NiCoFe, NiCoCr, NiCoMn, NiCrFe, NiCrMn, NiMnFe), four (NiCoCrFe, NiCoCrMn, NiCoFeMn) element mixing and eventually the five element mixed HEA (NiCoCrFeMn). This series allows us to break down the contribution of individual elements to the passivity of the alloys.

To access the single element contribution on the stability of the alloys, ICP-MS is employed, a technique that is capable to elementally resolve the released materials

from the alloys. We use a home-designed electrochemical flow cell[110] coupled with downstream ICP-MS detection.

We use normal pulse voltammetry (NPV) to potential-dependent probe the degradation of alloys. NPV is, in contrast to other electrochemical techniques like linear sweep voltammetry (LSV), more precise in testing anodic oxidation potential-resolved, since the single step potentials are probed individually. On the contrary, for LSV with its constantly changing potential, the 'history' has a much higher impact, since the degradation products and formed passive layers of all applied potentials accumulate on the surface. The reducing of the formed passive film at the base potential between the steps on one hand reconditions the surface to some extent, and on the other hand can provide additional information on the surface chemistry.

7.2 Materials and Methods

Chemicals and Sample preparation

All the alloys were designed equimolarly and synthesized by vacuum-arc melting with a water-cooled bowl mould. These alloys were NiMn, NiCo, NiFe, NiCr, NiCrMn, NiCrFe, NiMnFe, NiCoFe, NiCoCr, NiCoMn, NiCoCrFe, NiCoFeMn, NiCoCrMn, NiCoCrFeMn. All the alloys were flipped and remelted at least four times, and finally remelted into rectangular shape in a water-cooled rectangular mould. Homogenization treatment was conducted at 1100 °C for 6 h followed by water-quenching in order to get rid of interdendritic structure. However, homogenization treatment of NiMn alloy was conducted at 1000 °C because its melting point is below 1100 °C [238]. Then, all the alloys except NiMn alloy were cold-rolled to 70% and recrystallized at 1100 °C for 1 h followed by water-quenching to get uniform grain size around 100 to 200 μm . Cold-rolling could not be applied to NiMn alloy because of the complex second phase precipitation [238].

Eventually, all the alloys were line-cut into small samples of dimension $10\times 10\times 1$ mm for experiment. Alloy NBA600 was obtained from VDM-Metals, NBACr5 was provided by Hauke Springer (MPI f. Eisenforschung, Düsseldorf). Metals were prior

experiment ground with P2500 sand paper and polished with diamond paste down to $0.1 \mu\text{m}$, then cleaned in ethanol in an ultrasonic bath and then used without any further preconditioning.

Electrochemistry

A Biologic VSP-300 potentiostat (Biologic, France) or a PalmSens 4 (PalmSens BV, NL) were used for electrochemical measurements. All electrochemical experiments were performed with a Ag|AgCl-Electrode (in 3 M KCl, Multichannel Systems, DE) as reference electrode. The counter electrode is made from platinum. Normal Pulse Voltammetry was conducted starting from a base potential of -0.5 V to an upper potential of 1.5 V . Pulses with a step height of 50 mV and a pulse width of 30 s are applied in periods of 90 s .

7.3 Results

Normal Pulse Voltammetry Characterization: As indicated in **Fig. 7.1**, the alloys were polarized starting from $-0.5 \text{ V}_{\text{vs. Ag|AgCl}}$ with a step-wise ascending pulse profile with 30 s pulse length (all profiles are shown in the appendix **Fig. A.3.1**, p. **A11 ff.**). Depending on the applied voltages, the jump of potential may be accompanied by dissolution of material, with the online flow-cell ICP-MS detection elementally resolving the dissolution current.

At low applied pulse potentials the surface indicates no significant dissolution of material (see left part of **Fig. 7.1**). With progressively increasing the step polarization over an alloy and element dependent threshold, the dissolution profiles exhibit an increase of dissolution current (middle part of **Fig. 7.1**). In general, jumping back to the base potential instantly stops the dissolution. The subsequently observed decay of the dissolution profile results from the diffusion broadening in the flow system[92].

For quantitative analysis the dissolution per step was integrated as indicated by the shaded areas in **Fig. 7.1** exemplary for the pulse at $+0.55 \text{ V}$. Taking the whole range of the period including the base potential makes sure to cover the

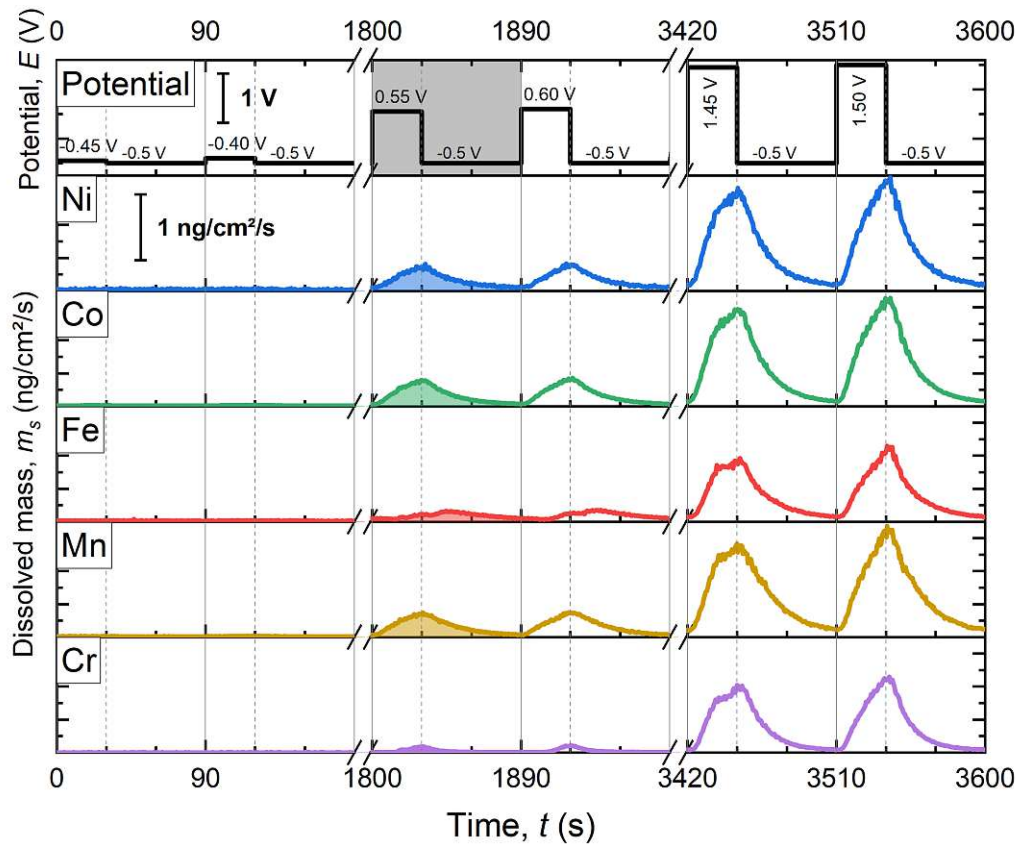


Figure 7.1: Detail of normal pulse voltammetry experiment on HEA alloy (NiCoCrFeMn) in neutral 1 mM NaCl solution. Shaded areas indicate exemplary limits for integration per period. Two periods cut from the beginning, middle and end of the experiment are shown. In the sequence the base potential is -0.5 V and the highest polarization is +1.5 V with the increment per step of +0.05 V.

complete material loss released during the pulse, and over the total dissolution sequence.

Fig. 7.2 shows the total dissolution currents integrated over all pulses of a sequence for all measured alloys, as function of the Cr, Fe and Mn potentials. In the further discussion we will hence reference the observed dissolution pattern of all alloys (see appendix A.3.1 for all data) to the binary alloy NiCo, which is at the origin of the plots in **Fig. 7.2**, and we discuss the behaviour in terms of adding the other functional elements. For this reference alloy data indicates that Ni and Co dissolve perfectly congruent, in 1:1 ratio, without any passive film formation (see also the

the studied alloys show very mild dissolution rates at this potential, particularly on the Cr-Fe plane, where we observe a clear trend of passivity increasing with the rise of Cr and Fe co-mixing level. Alloys containing less than 20% of both Cr and Fe exhibit relatively higher dissolution rates, e.g. NiCo, NBACr5 and NBA600.

Further, when mixing Cr with Mn, we observe a clear increase of dissolution rate with higher Mn content (as shown in the Cr-Mn plane). Here, the increasing of the Cr content does not in general passivate the alloy as can be seen in comparing NiCrMn (33% Cr) and NiCoCrMn (25% Cr), where the former shows a more significant dissolution rate than NiCoCrMn. Additionally, NiCrMn (33% Cr) shows in comparison with NiCoMn (0% Cr) a similar dissolution rate, suggesting that Cr is not functioning effectively as a passive film former in the presence of Mn.

At +1.0 V:

For all alloys containing Cr at this polarization, passivity built up by the chromium oxide is expected to deteriorate. This is also visible in **Fig. A.3.1** (page A10), which indicates that the Cr-dissolution rate starts to increase to bulk ratio at increasingly higher potentials.

At this potential most of the alloys on the Cr-Fe plane are showing increasing dissolution rate compared to +0.5 V polarization, with the alloys with less Cr and Fe content exhibiting higher dissolution rates. Alloys containing Mn develop increasing dissolution rates, except for NiFeMn, which still exhibits comparably low dissolution rates.

For the binary alloys, NiCr starts to show a weakening of its passivity due to the chromium oxide breakdown, while NiFe still remains at a extremely low dissolution rate. As expected, NiMn shows a progressive increase of dissolution rate, and indicates no effective passive film formation.

At +1.5 V:

At this polarization, most of the low or no Cr containing alloys develop very high dissolution rates. Interestingly, even it is well-known that Cr passive layer can break down at this polarization, alloys on the Cr-Fe plane are still showing significantly lower dissolution rate than most of other Mn-containing alloys. Here, alloy NiCoFeMn shows again the highest dissolution rate among all studied alloys.

It is worth mentioning, that the passivity of the NiCoCrFeMn alloy seems balanced by all the alloyed functional materials, which is not as good as Cr-Fe mixed alloys but significantly better than the Mn-alloyed samples and the reference sample (NiCo).

7.4 Discussion

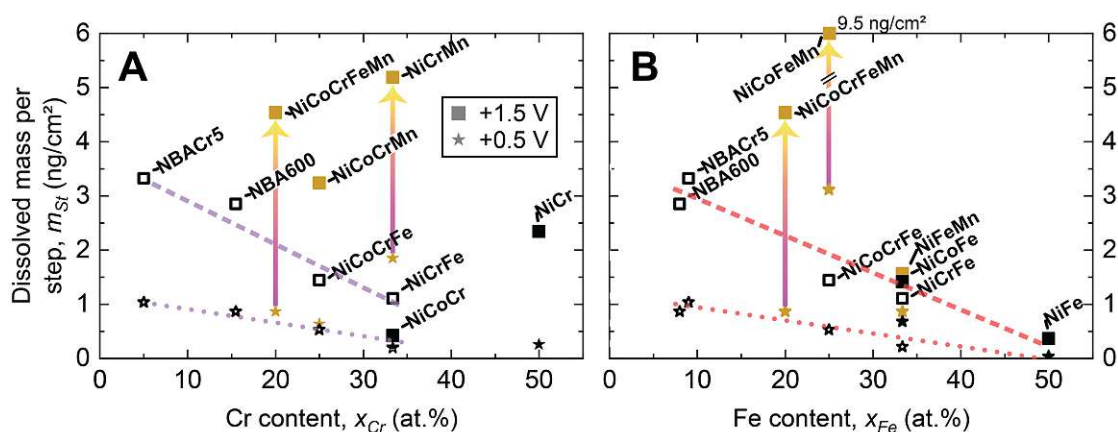


Figure 7.3: Dissolved mass per step for specific potentials (0.5, 1.0 and 1.5 V) against their concentration in Cr (A) and Fe (B).

Influence of Cr, Fe and Mn Although Fig. 7.2 provides us an overview of dissolution tendency of all studied alloys, it is not easy to intuitively extract the influence from individual elements. To visualize the role of the centrally important principal elements in an alloy, a simplified 2D overview with the dissolved mass of tested alloys plotted against atomic ratio of A) Cr and B) Fe at +1.5 V is shown in Fig. 7.3.

Here, the studied alloys are grouped into categories according to their principal elemental composition: All Mn-containing alloys are highlighted by yellow markers, Cr and Fe co-alloyed substrates have empty markers, and alloys containing solely Fe or Cr (besides Ni and Co) are shown with filled markers. The vertical arrows show the evolution of the mass loss of selected Mn-containing alloys from +0.5 pointing to +1.5 V. Two indicating trend lines (dashed) are plotted to show the trend of dissolved mass as a function of the concentration of the element of interest

at +0.5 (thin dash line) and +1.5 V (thick dash line), respectively.

For all Cr-Fe alloyed samples in **Fig. 7.3 A** (empty markers), we find a linear relationship between rising Cr concentration and a lowering of dissolution for both the low and high step potentials. As indicated by the dashed trend lines, the slope is related with the magnitude of the anodic polarization applied.

For low polarization of +0.5 V, this linear relationship is applicable to nearly all the Cr-Fe and Cr containing alloys. However, such proportionality seems invalid to NiCr (marked with black filled markers) at high anodic polarization. Here we observe that the mass loss of NiCr at +1.5 V is comparable to NBA600 with a Cr-content of 15.5%, suggesting the extra 34.5% Cr is not further stabilizing the alloy. In a sharp contrast, the similar Cr-only containing alloy NiCoCr (also marked in black) exhibits a considerably improved transient passivity. It also shows lower dissolution rates compared to the Cr-Fe containing alloys over the studied polarization range.

Surprisingly, for the NiCoCr the NPV profile shows, that the break-down potential for Cr in this alloy is shifted by +0.25 V towards more anodic potentials compared to the other Cr-Fe containing alloys (see SI A.3.1). This suggests a formation of a significantly stabilized chromium oxide structure, such as spinel $(NiCo)CrO_4$.

Our result indicate that - without the participation of Fe or Co - Cr itself is not able to form an effective transient passive film at higher potentials. This correlation is in line with the reported behaviour of pure chromium oxide passive film property by Tranchida et al. where it exhibits weaker passivity compared to stainless steel at high anodic polarization[195]. Adding Co may increase passivity without the presence of Fe and Mn (see NiCoCr). Again, this is in line with the formation of a thin film of the very stable spinel cobalt chromite $(CoCr_2O_4)$, which results in the significant anodic shift of the Cr breakdown potential. It has also been reported in literature that the oxide of NiCoCrFeMn may form a by spinel structure[223], which is consistent with the observed anodic stabilization of the oxide in this work.

As can be further seen in **Fig. 7.2**, the transient passive film stability is further

deteriorated by the addition of Mn (brown markers). Interestingly, the influence of Mn depends on both the applied polarization as well as the co-alloyed metals. For +0.5 V the impairing effect of the Mn is not yet clear for the alloys with only 20-25% Mn, namely NiCoCrFeMn and NiCoCrMn. Here we observe that the dissolution rates of both NiCoCrFeMn and NiCoCrMn are still in accordance with the trend seen for Cr-Fe containing alloys. Among all Cr-containing alloys at this potential, NiCrMn shows the highest dissolution rate.

It clearly pictures the metal-metal interactions across Co, Cr, Fe and Mn, that alloying Cr together with either Co and/or Fe can provide good passivity at +0.5 V polarization whether or not Mn is present. Without the participation of Co or Fe, the passivity of Cr deteriorates even at low polarization with the addition of Mn. At potentials higher than +0.5 V, the passivity imposed by Co, Fe and Cr is significantly deteriorated by Mn (see again yellow square data points in **Fig. 7.3 A**).

A similar analysis as a function of the Fe composition is shown in **Fig. 7.3 B**, where potential-dependent trend lines for +0.5 (stars) and +1.5 V polarisation (squares) are indicated. Here we again observe a decreasing trend of mass loss in all Cr-Fe containing alloys with the increase of Fe concentration. In addition, most other Cr-free Fe-containing alloys also fit well on these trend lines apart from two Mn containing alloys: NiCoCrFeMn and NiCoFeMn. Our results suggest the formation of a Fe containing passive film lowering dissolution, which shows positive synergy with Cr. As such, data suggests that Fe forms an insoluble layer that limits dissolution at high potentials, where the chromium oxide fails to provide any passivity. This, however, does not imply a general good corrosion resistance, as the insoluble iron oxide is not necessarily forming a well adhering passive film in most cases.

The three studied Mn-Fe containing alloys exhibit in each case a different behaviour. Firstly, NiFeMn shows exactly the same dissolution trend as other Fe-containing alloys for both low and high anodic polarization. Secondly, NiCoFeMn shows completely opposite behaviour compared to NiFeMn, which exhibits highest dissolution rate at +0.5 V among all the studied samples, and further develops

to 9.5 ng/cm² at +1.5 V. Interestingly, the dissolution behaviour of NiCoCrFeMn exhibits a potential dependency similar to NiFeMn at +0.5 V, but then for +1.5 V shows significant higher mass dissolved.

In a short summary, we conclude for the influence of Cr and Fe a strong correlation of dissolution rate and iron content, while for Cr such a correlation is only limited to the Cr-Fe-containing alloys. Addition of Mn in general deteriorates the passivity in most of Cr related alloys (**Fig. 7.3 A**) at high polarization, however we did not find direct Mn-Fe correlation.

Although the amount of total dissolved mass is a good indicator for the transient passivity of the alloys, it can not clearly explain the difference in passivation mechanisms between alloys. Scaling the total dissolved mass over a whole sequence down to individual pulses (as indicated in **Fig. 7.1**, shaded areas), we found a clear change in dissolution pattern across all studied alloys between the anodic step pulse and reconditioning potentials. During the period of a single step, the majority of the integrated mass is collected from the dissolution during the applied step potential, which is later labelled as "anodic peak". Switching from the step potential back to the recondition potential, most of the cases exhibit a logarithmic decay profile due to the diffusion broadening during the transportation. However, the dissolution profiles clearly indicate that particular cases (Ni-Cr containing alloys as e.g. NiCoCrFe, NiCoCrFeMn, NiCrFe) exhibit a clear active Fe dissolution during the recondition phase, which is labelled as "cathodic peak". In addition, this cathodic dissolution peak shows a pronounced shift in response to the level of the previously applied anodic polarization, likely due to kinetic effects of the dissolution (noted as shifted in **Fig. 7.4**).

Fe dissolution profiles **Fig. 7.4** displays the stacked dissolution profile in selected NPV pulse periods of elements of interest to correlate the elemental mass lost with applied step polarizations. We particularly discuss three Fe containing MPEAs of **A**) NiCoFeMn, **B**) NiCoCrFe and **C**) NiCoCrFeMn, which show very distinct dissolution behaviours as observed in **Fig. 7.3 B**.

Panel **A**_{Ni} exemplary uses Ni in NiCoFeMn alloy to demonstrate the typical anodic peak profile, which generally applies for all other elements in this alloy including

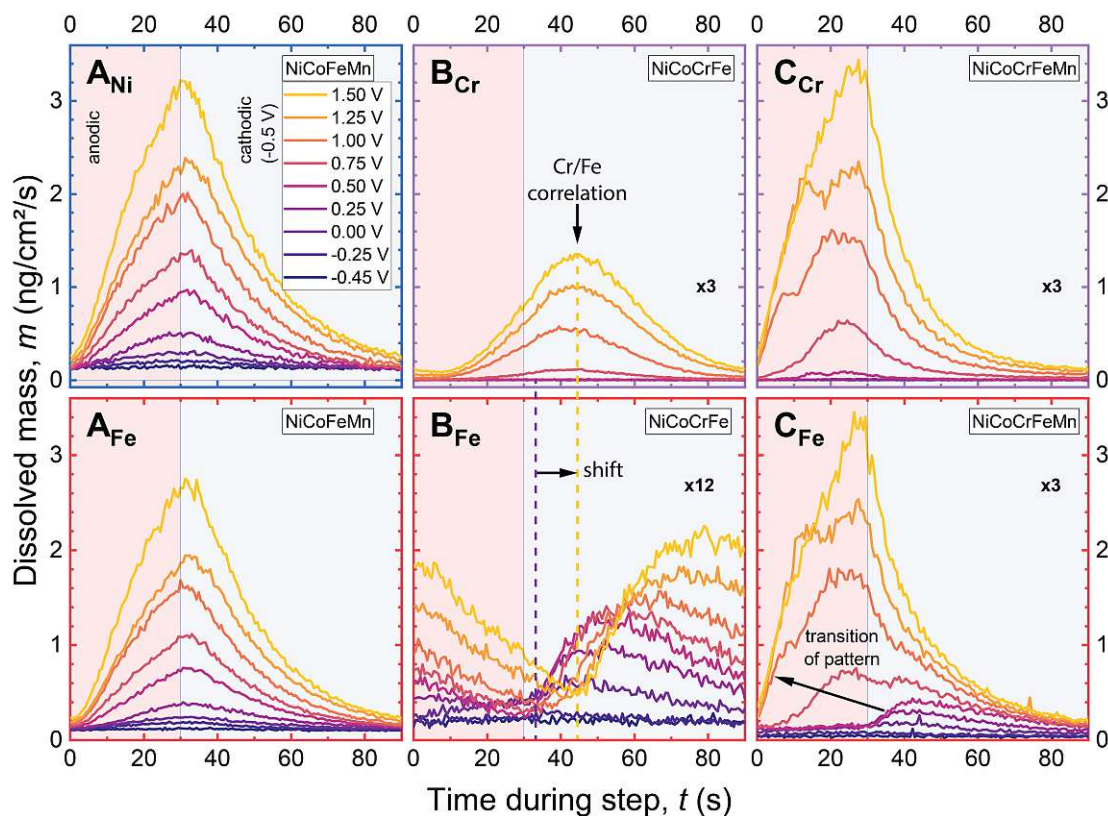


Figure 7.4: Elemental dissolution behaviour of Ni, Cr, Fe for A) NiCoFeMn, B) NiCoCrFe and C) NiCoCrFeMn for selected step potentials. Anodic polarization (red shading) at rising potentials is followed by reconditioning at -0.5 V.

Fe as shown in Panel **A_{Fe}**. A cathodic peak profile is observed for NiCoCrFe as shown in panel **B_{Fe}**, where a very steep increase of dissolution rate is observed upon application of the recondition potential of -0.5 V. However, the dissolution immediately drops with the application of the reconditioning potential, indicating the origin of the reaction may not be related to the decomposition of bulk material. Further, in panel **Fig. 7.4 B_{Cr}** we also notice that the dissolution profile of Cr in NiCoCrFe does not directly correlate with the application of the potential from anodic to cathodic polarisation potential-dependent, while it exhibits a very clear delay in onset of dissolution as well as a peaking around 10 s after switching from anodic to cathodic polarization. Based on the continuous dissolution profile it appears that Cr undergoes an electrochemically induced growth of a passive film followed by its chemical dissolution.

This behaviour generally applies to all Cr-Fe containing alloys without Mn, suggesting that a Cr passive film grows in a steady-state process with ongoing dissolution. Panel B_{Fe} in **Fig. 7.4** further indicates a correlation between the Fe and Cr dissolution behaviour. In contrast to NiCoFeMn (panel A_{Fe}) the cathodic Fe peak for NiCoCrFe (panel B_{Fe}) coincides with the polarization switch to low potentials, where no Cr dissolution is yet observed. As soon as the Cr dissolution sets in, the cathodic Fe peak delays, as indicated by the dashed line. Interestingly, with the significant Cr dissolution the cathodic iron onset aligns with the onset of the Fe dissolution. The magnitude of the Fe cathodic peak shift coincides with the delay of dissolution peak of Cr, where the onset of Fe cathodic dissolution is well-aligned with the peak position of Cr (seen in **Fig. 7.4** B_{Cr}).

Moreover, the Fe dissolution pattern of NiCoCrFeMn shown in **Fig. 7.4** C_{Fe} is a hybrid case between NiCoFeMn and NiCoCrFe. Here, the dissolution behaviour of Fe indicates a cathodic peak when no significant Cr dissolution occurs (C_{Cr}), which is similar to NiCoCrFe for potentials below +0.7 V. Congruently with the Cr dissolution, the anodic peak increases significantly with increasing anodic step potentials, which is similar to NiCoCrMn.

Precisely, participation of Mn effectively changes the Fe dissolution pattern from cathodic to anodic dissolution. In addition, Cr simultaneously breaks down with Fe under high polarisation, rendering the passivating elements electrochemically unstable, due to the presence of Mn. As such, this data strongly suggests that Mn inhibits the formation of an insoluble passive film.

For a better overview we summarize in **Fig. 7.5** the observed Fe dissolution patterns of all studied alloys in categories. Here, we assigned each Fe dissolution pattern to one of five categories labelled with different colors as shown at the top panels. The main line-chart displays the patterns found at each applied step potential over the whole studied polarization range. The graph on the left shows the composition of Fe, Cr and Mn with Ni/NiCo as background matrix in studied alloys, with the order from top to bottom from Fe-Mn over Mn-Cr, Cr to Fe only.

The alloys on the top containing Mn only, besides Fe and Ni/Co, exhibit solely

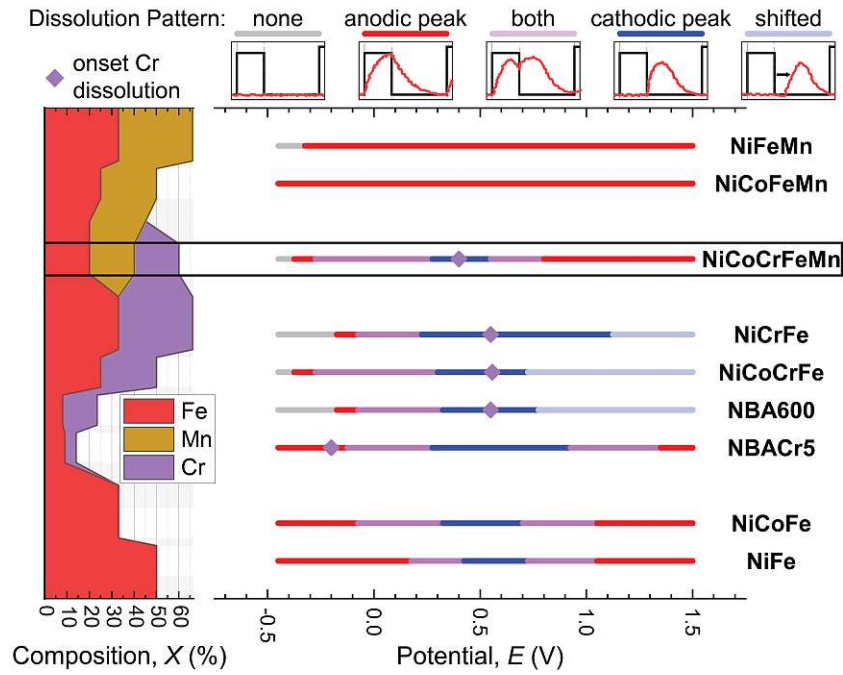


Figure 7.5: Distribution of the various Fe dissolution phenomena observed over the step potential range of -0.5 to $+1.5$ V during NPV, sorted by the presence of Cr and Mn. Anodic and cathodic peak indicate a clear onset of dissolution with the sudden change of potential towards more positive or negative potentials, respectively. The label 'both' is assigned for pulses where anodically and cathodically dissolved Fe could be detected simultaneously. Label 'none' indicate that no dissolution is detected. The left graph shows the composition of the alloys in Fe, Cr and Mn with Ni and/or Co co-alloyed.

"anodic peak" dissolution of Fe over the whole range of applied potential. As soon as Cr is present (i.e. in NiCoCrFeMn), the Fe dissolution pattern at a given range of step polarization is altered from pure "anodic peak" to "cathodic peak". The first transition from anodic to cathodic peak is around -0.2 V, where the dissolution rate is significantly reduced compared to NiCoFeMn in the same region. This indicates a clear Cr dependent passivity in low polarization being introduced to the Fe-Mn containing alloy. However, the break-down of Cr at higher anodic polarization triggers the second transition from cathodic back to the anodic peak around +0.45 V, where the dissolution rate becomes higher again.

Adding Cr is very crucial in stabilizing the Fe from anodic dissolution. As shown in the middle of the main panel, the 4 studied Cr-Fe containing alloys are all showing very good transient passivity in anodic polarization. Only when Cr content is below the critical value, i.e. NBACr5, the anodic transient passivity can be deteriorated. This is expressed in the transition from cathodic back to the anodic peak with rising anodic step polarization.

In addition, dissolution of Cr can significantly delay the cathodic peak of Fe in all Cr-Fe containing alloys beside NBACr5. As marked "shifted" in the panel, it is a very unique feature that is only found in Cr-Fe containing alloys with sufficient Cr content, whereas NBACr5 with only 5% of Cr shows no shift of cathodic peak but anodic peak at high anodic polarization.

Comparing the Cr break-down potential between NBACr5 and NiCoCrFeMn, NBACr5 exhibits an extremely early onset of Cr dissolution already at -0.2 V, which is far deviated from the prediction of the Pourbaix diagram at the given pH of 7. This feature indicates Cr is not able to form a thermodynamically stable oxide when its concentration in an alloy is below 10%. Similarly, NiCoCrFeMn shows a negative shift of about 0.1 V of the Cr dissolution onset potential comparing to other Cr-Fe alloys (typically around +0.55 V), suggesting Mn changes the thermodynamic stability of the Cr passive layer.

At the very bottom, we compare also the Fe dissolution behaviour of alloys containing only Fe and matrix metals (Ni and Co). Both NiCoFe and NiFe show a very similar trend with a region of cathodic peaks around +0.5 V and further

transition to the anodic peak feature.

In summary, our data suggests that addition of Cr can generally and significantly improve an alloy's stability at high anodic polarization. This confirms the synergistic stabilizing effect of Fe and Cr in the passive film. In contrast, Mn can completely eradicate its anodic stability over the whole range of the studied alloys. Cr can only stabilise a Mn containing alloy at low potentials before Cr dissolution becomes apparent.

7.5 Conclusion

In this work, we systematically demonstrate a bottom-up approach to resolve metal-metal correlations of complex alloy systems. Combining with a material library of equimolar binary up to quinary alloys of Ni, Co, Cr, Fe and Mn, we have successfully identified the influence of individual added principal elements on the electrochemical properties and corrosion resistivity of alloys.

Among the five studied principal elements, we find Cr, Mn and Fe to play decisive roles on the material's anti-corrosion property. For our system we summarize the identified alloying properties of the studied principal elements as following:

- A high chromium content in itself does not necessarily lead to a stable transient passive film.
- An increase of the manganese concentration weakens the corrosion resistance of the alloy significantly.
- The cathodic dissolution of the transiently formed passive film provides a detailed view on the surface chemistry of passive films formed during active polarization.
- Chromium oxide does not effectively grow at high potentials above 1.2 V, and Fe oxide replaces Cr as passivating element under these conditions.
- There are hints that suggest the formation of a spinel-type compound for NiFeCr and NiCoCr

The unique utilisation of NPV in an ICP-flow cell provides a direct view into surface chemistry during passive film formation and corrosion inhibition. The established experimental procedure may prove useful for the characterisation of other alloys and material libraries. With the elementally resolved breakdown potentials, indirect information about surface composition and passive layer stability is achieved. The method, when applied to a variety of material classes has the potential to provide insightful datasets also for machine learning algorithms.

Chapter 8

Conclusion and Outlook

The here reported conclusions are of general nature, the more specific ones related to the individually studied material systems are already addressed at the end of the former chapters.

With many surface sensitive techniques being bound to ultra high vacuum conditions solid|liquid interfaces are poorly accessible. In the present work, we successfully designed and enhanced electrochemical cells to *in situ* probe materials at the solid|liquid interface regarding their stability. We implemented electrochemical Atomic Force Microscopy (EC-AFM) as well as electrochemical flow cells with downstream Inductively Coupled Plasma Mass Spectrometry (ICP-MS) detection. The two techniques complementary, but also individually, provide useful insights on the processes happening at the solid|liquid boundary. In this work we studied passive film quality, repassivation, stability of corrosion protection layers, (photo-)electrochemical catalyst degradation and stabilisation.

AFM and ICP-MS results were supplemented with classical *ex situ* methods of surface science like XPS and XRF, as well as with computational results for an integrated picture of surfaces.

EC-AFM A new design for an EC-AFM cell was suggested with a plate-plate electrode geometry. With an evenly potential and current distribution in an actual experimental setup it performs very well during corrosion. The design has been

tested on topics relevant to corrosion, namely on anodic detachment of protective thin films and the metal oxide film quality during active-passive cycles.

The method, while already well established, still offers potential for development: One example might be the extension to chemical force microscopy. There, instead of the usually imaging force distance curves are recorded with the AFM being chemically modified. With this approach the potential-dependent adhesion of organic molecules on metallic and oxidic surfaces can be probed. This can prove useful for coating technologies. Further, the implementation of light irradiation into the AFM-cell should facilitate to further understand photocorrosion also spatially resolved.

Electrochemical ICP-MS flow cells An electrochemical flow cell setup for material degradation studies with ICP-MS was established in the group as a powerful tool to investigate electrochemical processes as corrosion, corrosion protection and (photo)-catalysis. With elementally and time resolved dissolution rates the solution side of degradation processes is accessible. With its extremely low detection limit ICP-MS is capable to access already the very initial steps of material degradation. The approach used is essential for a efficient design of stable materials.

Specifically, in the present work the implementation of a photo-electrochemical flow cell for ICP was developed independently in parallel with other working groups[17–20]. This work showed that ICP-MS with UV irradiation can be useful to test materials for their photocorrosion resistance, broadening the applicability of the method, and also taking surface orientation into account by the use of single crystals. A general challenge for flow cells has been identified. With the use of O-rings a crevice former is introduced into the system, especially problematic for materials that are prone to crevice corrosion. With an adaption of the sample design towards embedded samples side-effects originating from the crevice could be restricted.

The electrochemical flow cells were utilized for material systems relevant for anodic corrosion, passive film formation and stability, photo-induced corrosion and adhesion of organic layers.

The ICP-MS based methodology still has the potential of development to allow for even wider applications:

- ICP-MS elementally resolves the dissolved ions. By combination with suitable chromatographic techniques the method might be extended to also provide information on chemical speciation, or oxidation state of the ions dissolved, that might help to gain more mechanistic insights in degradation processes.
- Since ICP-MS can easily differentiate between isotopes, atom labelling can be employed to observe e.g. exchange reactions, or with spatial isotope labels provide locally resolved data.
- Also the extension towards non-aqueous electrochemistry with adaption of the sample introduction system of the used ICP-MS system is possible, paving the way to study under realistic conditions e.g. battery systems.

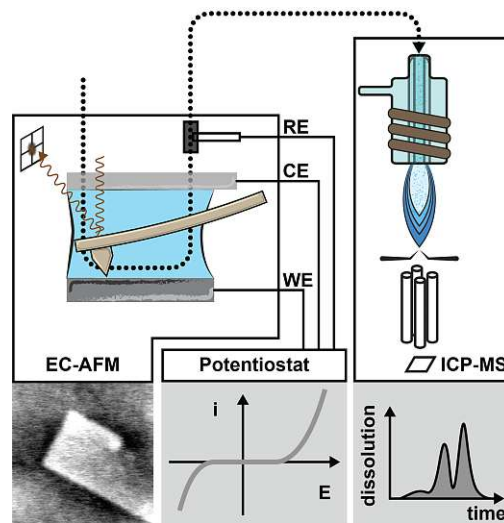


Figure 8.1: Future setup with EC-AFM and ICP-MS combined, yielding topographic, electrochemical and solution-side elemental dissolution rates almost in real time.

Altogether, the work presented here shows a variety of applications of the usage of two *in situ* techniques to study stability of solid|liquid interfaces. The techniques supplement each other in their explanatory power and pave the way to gain complementary knowledge about fundamental processes on electrochemical active

solid|liquid interfaces. The established experimental setups enrich the tools available in the group of Applied Interface Physics. This thesis has laid the ground for the next logical step to take (as shown in **Fig. 8.1**): A direct combination of the two experimental setups enables to obtain both spatially and elementally resolved information, parallel and in real time.

Bibliography

- [1] R. Knight, L. J. Pyrak-Nolte, L. Slater, E. Atekwana, A. Endres, J. Geller, D. Lesmes, S. Nakagawa, A. Revil, M. M. Sharma, and C. Straley, “Geophysics at the interface: Response of geophysical properties to solid-fluid, fluid-fluid, and solid-solid interfaces,” *Reviews of Geophysics*, vol. 48, no. 4, 2010.
- [2] H.-J. Butt, B. Cappella, and M. Kappl, “Force measurements with the atomic force microscope: Technique, interpretation and applications,” *Surface Science Reports*, vol. 59, no. 1-6, pp. 1–152, 2005.
- [3] D. Quéré, “Wetting and Roughness,” *Annual Review of Materials Research*, vol. 38, no. 1, pp. 71–99, 2008.
- [4] F. Zaera, “Surface chemistry at the liquid/solid interface,” *Surface Science*, vol. 605, no. 13-14, pp. 1141–1145, 2011.
- [5] Y. Kawahara, “High temperature corrosion mechanisms and effect of alloying elements for materials used in waste incineration environment,” *Corrosion Science*, vol. 44, no. 2, pp. 223–245, 2002.
- [6] G. Koch, “Cost of corrosion,” in *Trends in Oil and Gas Corrosion Research and Technologies*, pp. 3–30, Elsevier, 2017.
- [7] M. Salmeron, “From Surfaces to Interfaces: Ambient Pressure XPS and Beyond,” *Topics in Catalysis*, vol. 61, no. 20, pp. 2044–2051, 2018.
- [8] G. S. Frankel, T. Li, and J. R. Scully, “Perspective—Localized Corrosion:

Passive Film Breakdown vs Pit Growth Stability,” *Journal of The Electrochemical Society*, vol. 164, no. 4, pp. C180–C181, 2017.

- [9] S. Manne, H. J. Butt, S. A. C. Gould, and P. K. Hansma, “Imaging metal atoms in air and water using the atomic force microscope,” *Applied Physics Letters*, vol. 56, no. 18, pp. 1758–1759, 1990.
- [10] B. J. Cruickshank, A. A. Gewirth, R. M. Rynders, and R. C. Alkire, “In Situ Observations of Shape Evolution during Copper Dissolution Using Atomic Force Microscopy,” *Journal of The Electrochemical Society*, vol. 139, no. 10, pp. 2829–2832, 1992.
- [11] A. A. Gewirth and H. Siegenthaler, eds., *Nanoscale Probes of the Solid/Liquid Interface*. Dordrecht: Springer Netherlands, 1995.
- [12] L. Gross, F. Mohn, N. Moll, P. Liljeroth, and G. Meyer, “The chemical structure of a molecule resolved by atomic force microscopy,” *Science (New York, N.Y.)*, vol. 325, no. 5944, pp. 1110–1114, 2009.
- [13] K. Ogle, “Atomic Emission Spectroelectrochemistry: Real-Time Rate Measurements of Dissolution, Corrosion, and Passivation,” *CORROSION*, vol. 75, no. 12, pp. 1398–1419, 2019.
- [14] S. Cherevko and K. Mayrhofer, “On-Line Inductively Coupled Plasma Spectrometry in Electrochemistry: Basic Principles and Applications,” in *Encyclopedia of interfacial chemistry : surface science and electrochemistry* (K. .-a. Wandelt, ed.), pp. 326–335, Oxford: Elsevier, 2018.
- [15] R. Thomas, *Practical Guide to ICP-MS: A Tutorial for Beginners, Third Edition*. CRC Press, 2013.
- [16] P. Marcus, *Corrosion mechanisms in theory and practice*, vol. 26 of *Corrosion technology*. Boca Raton: CRC Press, 3rd ed. ed., 2012.
- [17] J. Knöppel, S. Zhang, F. D. Speck, K. J. Mayrhofer, C. Scheu, and S. Cherevko, “Time-resolved Analysis of Dissolution Phenomena in Photoelectrochemistry – A Case Study of WO₃ Photocorrosion,” *Electrochemistry Communications*, vol. 96, pp. 53–56, 2018.

- [18] O. Kasian, S. Geiger, T. Li, J.-P. Grote, K. Schweinar, S. Zhang, C. Scheu, D. Raabe, S. Cherevko, B. Gault, and K. J. J. Mayrhofer, “Degradation of Iridium Oxides via Oxygen Evolution from the Lattice: Correlating Atomic Scale Structure with Reaction Mechanisms,” *Energy & Environmental Science*, vol. 12, no. 12, pp. 3548–3555, 2019.
- [19] S. Zhang, M. Rohloff, O. Kasian, A. M. Mingers, K. J. J. Mayrhofer, A. Fischer, C. Scheu, and S. Cherevko, “Dissolution of BiVO₄ Photoanodes Revealed by Time-Resolved Measurements under Photoelectrochemical Conditions,” *The Journal of Physical Chemistry C*, vol. 123, no. 38, pp. 23410–23418, 2019.
- [20] J. Knöppel, A. Kormányos, B. Mayerhöfer, A. Hofer, M. Bierling, J. Bachmann, S. Thiele, and S. Cherevko, “Photocorrosion of WO₃ Photoanodes in Different Electrolytes,” *ACS Physical Chemistry Au*, 2021.
- [21] M. Pourbaix, *Thermodynamics of Dilute Aqueous Solutions: Graphical Representation of the Role of pH and Potential*. PhD thesis, Delft University of Technology, Delft, 1945.
- [22] M. Pourbaix, “Applications of electrochemistry in corrosion science and in practice,” *Corrosion Science*, vol. 14, no. 1, pp. 25–82, 1974.
- [23] H. E. Townsend, “Potential-pH diagrams at elevated temperature for the system Fe-H₂O,” *Corrosion Science*, vol. 10, no. 5, pp. 343–358, 1970.
- [24] M. Pourbaix, *Atlas of electrochemical equilibria in aqueous solutions*. Houston: NACE International, 1974.
- [25] K. Wang, J. Han, A. Y. Gerard, J. R. Scully, and B.-C. Zhou, “Potential-pH diagrams considering complex oxide solution phases for understanding aqueous corrosion of multi-principal element alloys,” *npj Materials Degradation*, vol. 4, no. 1, 2020.
- [26] P. Marcus and V. Maurice, “Atomic level characterization in corrosion studies,” *Philosophical transactions. Series A, Mathematical, physical, and engineering sciences*, vol. 375, no. 2098, 2017.

- [27] G. Binnig, H. Rohrer, C. Gerber, and E. Weibel, "Tunneling through a controllable vacuum gap," *Applied Physics Letters*, vol. 40, no. 2, pp. 178–180, 1982.
- [28] G. Binnig, C. F. Quate, and C. Gerber, "Atomic force microscope," *Physical Review Letters*, vol. 56, no. 9, pp. 930–933, 1986.
- [29] G. Binnig and H. Rohrer, "Scanning tunneling microscopy—from birth to adolescence," *Reviews of Modern Physics*, vol. 59, no. 3, pp. 615–625, 1987.
- [30] D. M. Eigler and E. K. Schweizer, "Positioning single atoms with a scanning tunnelling microscope," *Nature*, vol. 344, no. 6266, pp. 524–526, 1990.
- [31] R. Sonnenfeld and P. K. Hansma, "Atomic-resolution microscopy in water," *Science (New York, N. Y.)*, vol. 232, no. 4747, pp. 211–213, 1986.
- [32] K. Itaya and E. Tomita, "Scanning tunneling microscope for electrochemistry - a new concept for the in situ scanning tunneling microscope in electrolyte solutions," *Surface Science*, vol. 201, no. 3, pp. L507–L512, 1988.
- [33] J. Wiechers, T. Twomey, D. M. Kolb, and R. J. Behm, "An in-situ scanning tunneling microscopy study of au (111) with atomic scale resolution," *Journal of Electroanalytical Chemistry and Interfacial Electrochemistry*, vol. 248, no. 2, pp. 451–460, 1988.
- [34] P. Lustenberger, H. Rohrer, R. Christoph, and H. Siegenthaler, "Scanning tunneling microscopy at potential controlled electrode surfaces in electrolytic environment," *Journal of Electroanalytical Chemistry and Interfacial Electrochemistry*, vol. 243, no. 1, pp. 225–235, 1988.
- [35] T. Fries, K. Oster, and K. Wandelt, "In-situ stress investigations on thin copper films with the STM," *Advanced Materials*, vol. 6, no. 6, pp. 473–476, 1994.
- [36] M. Krufft, B. Wohlmann, C. Stuhlmann, and K. Wandelt, "Chloride adsorption on Cu(111) electrodes in dilute HCl solutions," *Surface Science*, vol. 377-379, pp. 601–604, 1997.
- [37] M. Wilms, P. Broekmann, M. Krufft, C. Stuhlmann, and K. Wandelt, "STM

investigation of step orientation and surface dynamics of Cu(111) in hydrochloric acid electrolyte,” *Applied Physics A: Materials Science & Processing*, vol. 66, no. 7, pp. S473–S475, 1998.

- [38] G. Barati, V. Solokha, K. Wandelt, K. Hingerl, and C. Cobet, “Chloride-induced morphology transformations of the Cu(110) surface in dilute HCl,” *Langmuir : the ACS journal of surfaces and colloids*, vol. 30, no. 48, pp. 14486–14493, 2014.
- [39] K. Gentz and K. Wandelt, “Electrochemical scanning tunneling microscopy,” *Chimia*, vol. 66, no. 1-2, pp. 44–51, 2012.
- [40] V. Maurice and P. Marcus, “Scanning Tunneling Microscopy and Atomic Force Microscopy,” in *Analytical Methods In Corrosion Science and Engineering* (P. Marcus and F. B. Mansfeld, eds.), pp. 133–168, CRC Press, 2005.
- [41] S. Manne, P. K. Hansma, J. Massie, V. B. Elings, and A. A. Gewirth, “Atomic-resolution electrochemistry with the atomic force microscope: copper deposition on gold,” *Science (New York, N.Y.)*, vol. 251, no. 4990, pp. 183–186, 1991.
- [42] D. D. Sneddon and A. A. Gewirth, “In situ characterization of halide adsorption and Ag-halide growth on Ag(111) electrodes using atomic force microscopy,” *Surface Science*, vol. 343, no. 3, pp. 185–200, 1995.
- [43] N. Ikemiya, T. Kubo, and S. Hara, “In situ AFM observations of oxide film formation on Cu(111) and Cu (100) surfaces under aqueous alkaline solutions,” *Surface Science*, vol. 323, no. 1-2, pp. 81–90, 1995.
- [44] M. G. Walls, A. Ponthieux, B. Rondot, and R. A. Owen, “In situ observation of the oxidation and reduction processes on Fe–Cr alloys,” *Journal of Vacuum Science & Technology A*, vol. 14, no. 3, pp. 1362–1367, 1996.
- [45] L. Chen and D. Guay, “Selected Dissolution of Aluminum Initiated by Atomic Force Microscope Tip–Surface Interaction,” *Journal of The Electrochemical Society*, vol. 141, no. 4, pp. L43–L45, 1994.

- [46] H. Chen, Z. Qin, M. He, Y. Liu, and Z. Wu, “Application of Electrochemical Atomic Force Microscopy (EC-AFM) in the Corrosion Study of Metallic Materials,” *Materials*, vol. 13, no. 3, 2020.
- [47] K. W. Shinato, F. Huang, and Y. Jin, “Principle and application of atomic force microscopy (AFM) for nanoscale investigation of metal corrosion,” *Corrosion Reviews*, vol. 38, no. 5, pp. 423–432, 2020.
- [48] J.-e. Qu, X.-P. Guo, H.-R. Wang, and J.-Y. Huang, “Corrosion behavior of pure aluminum in FeCl₃ solution,” *Transactions of Nonferrous Metals Society of China*, vol. 16, no. 6, pp. 1460–1466, 2006.
- [49] P. Schmutz and G. S. Frankel, “Influence of Dichromate Ions on Corrosion of Pure Aluminum and AA2024–T3 in NaCl Solution Studied by AFM Scratching,” *Journal of The Electrochemical Society*, vol. 146, no. 12, pp. 4461–4472, 1999.
- [50] S. Moore, R. Burrows, L. Picco, T. L. Martin, S. J. Greenwell, T. B. Scott, and O. D. Payton, “A study of dynamic nanoscale corrosion initiation events using HS-AFM,” *Faraday Discussions*, vol. 210, no. 0, pp. 409–428, 2018.
- [51] X. F. Yang and J. E. Castle, “Using in situ AFM to investigate corrosion and passivation of duplex stainless steels,” *Surface and Interface Analysis*, vol. 33, no. 10-11, pp. 894–899, 2002.
- [52] R. Jia, S. Yu, D. Li, T. Zhang, F. Wang, and C. Zhong, “Study on the effect of mischmetal (La,Ce) on the micro-galvanic corrosion of AZ91 alloy using multiscale methods,” *Journal of Alloys and Compounds*, vol. 778, pp. 427–438, 2019.
- [53] M. Valtiner, G. N. Ankah, A. Bashir, and F. U. Renner, “Atomic force microscope imaging and force measurements at electrified and actively corroding interfaces: challenges and novel cell design,” *The Review of scientific instruments*, vol. 82, no. 2, p. 023703, 2011.
- [54] M. A. Amin, S. S. Abd El-Rehim, F. D. A. Aarão Reis, and I. S. Cole,

“Metastable and stable pitting events at zinc passive layer in alkaline solutions,” *Ionics*, vol. 20, no. 1, pp. 127–136, 2014.

- [55] J. Li, H. Huang, M. Fielden, J. Pan, L. Ecco, C. Schellbach, G. Delmas, and P. M. Claesson, “Towards the mechanism of electrochemical activity and self-healing of 1 wt% PTSA doped polyaniline in alkyd composite polymer coating: combined AFM-based studies,” *RSC Advances*, vol. 6, no. 23, pp. 19111–19127, 2016.
- [56] J. Li, L. Ecco, A. Ahniyaz, and J. Pan, “Probing electrochemical mechanism of polyaniline and CeO₂ nanoparticles in alkyd coating with in-situ electrochemical-AFM and IRAS,” *Progress in Organic Coatings*, vol. 132, pp. 399–408, 2019.
- [57] G. H. Simon, C. S. Kley, and B. Roldan Cuenya, “Potential-Dependent Morphology of Copper Catalysts During CO₂ Electroreduction Revealed by In Situ Atomic Force Microscopy,” *Angewandte Chemie International Edition*, vol. 60, no. 5, pp. 2561–2568, 2021.
- [58] X.-R. Liu, X. Deng, R.-R. Liu, H.-J. Yan, Y.-G. Guo, D. Wang, and L.-J. Wan, “Single nanowire electrode electrochemistry of silicon anode by in situ atomic force microscopy: solid electrolyte interphase growth and mechanical properties,” *ACS applied materials & interfaces*, vol. 6, no. 22, pp. 20317–20323, 2014.
- [59] X. Deng, F. Galli, and M. T. M. Koper, “In Situ Electrochemical AFM Imaging of a Pt Electrode in Sulfuric Acid under Potential Cycling Conditions,” *Journal of the American Chemical Society*, vol. 140, no. 41, pp. 13285–13291, 2018.
- [60] D. Liu, Z. Shadike, R. Lin, K. Qian, H. Li, K. Li, S. Wang, Q. Yu, M. Liu, S. Ganapathy, X. Qin, Q.-H. Yang, M. Wagemaker, F. Kang, X.-Q. Yang, and B. Li, “Review of Recent Development of In Situ/Operando Characterization Techniques for Lithium Battery Research,” *Advanced Materials*, vol. 31, no. 28, p. e1806620, 2019.
- [61] C. Shen, S. Wang, Y. Jin, and W.-Q. Han, “In Situ AFM Imaging of Solid

Electrolyte Interfaces on HOPG with Ethylene Carbonate and Fluoroethylene Carbonate-Based Electrolytes,” *ACS applied materials & interfaces*, vol. 7, no. 45, pp. 25441–25447, 2015.

- [62] I. Khalakhan, A. Choukourov, M. Vorokhta, P. Kúš, I. Matolínová, and V. Matolín, “In situ electrochemical AFM monitoring of the potential-dependent deterioration of platinum catalyst during potentiodynamic cycling,” *Ultramicroscopy*, vol. 187, pp. 64–70, 2018.
- [63] T. Morawietz, M. Handl, C. Oldani, K. A. Friedrich, and R. Hiesgen, “Quantitative in Situ Analysis of Ionomer Structure in Fuel Cell Catalytic Layers,” *ACS applied materials & interfaces*, vol. 8, no. 40, pp. 27044–27054, 2016.
- [64] J. H. J. Wijten, L. D. B. Mandemaker, T. C. van Eeden, J. E. Dubbeld, and B. M. Weckhuysen, “In Situ Study on Ni-Mo Stability in a Water-Splitting Device: Effect of Catalyst Substrate and Electric Potential,” *ChemSusChem*, vol. 13, no. 12, pp. 3172–3179, 2020.
- [65] T. Wade, J. F. Garst, and J. L. Stickney, “A simple modification of a commercial atomic force microscopy liquid cell for in situ imaging in organic, reactive, or air sensitive environments,” *Review of Scientific Instruments*, vol. 70, no. 1, pp. 121–124, 1999.
- [66] E. J. Wanless, T. J. Senden, A. M. Hyde, T. J. Sawkins, and G. A. Heath, “A new electrochemical cell for atomic force microscopy,” *Review of Scientific Instruments*, vol. 65, no. 4, pp. 1019–1020, 1994.
- [67] F. Hausen, J. A. Zimmet, and R. Bennewitz, “Surface structures and frictional properties of Au(100) in an electrochemical environment,” *Surface Science*, vol. 607, pp. 20–24, 2013.
- [68] C. Delacourt, P. L. Ridgway, V. Srinivasan, and V. Battaglia, “Measurements and Simulations of Electrochemical Impedance Spectroscopy of a Three-Electrode Coin Cell Design for Li-Ion Cell Testing,” *Journal of The Electrochemical Society*, vol. 161, no. 9, pp. A1253–A1260, 2014.
- [69] S. Klink, E. Madej, E. Ventosa, A. Lindner, W. Schuhmann, and F. La Man-

tia, “The importance of cell geometry for electrochemical impedance spectroscopy in three-electrode lithium ion battery test cells,” *Electrochemistry Communications*, vol. 22, pp. 120–123, 2012.

- [70] A. Kreta, M. Gaberšček, and I. Muševič, “Time-resolved in situ electrochemical atomic force microscopy imaging of the corrosion dynamics of AA2024–T3 using a new design of cell,” *Journal of Materials Research*, vol. 36, no. 1, pp. 79–93, 2021.
- [71] Daniel Pröfrock and Andreas Prange, “Inductively Coupled Plasma-Mass Spectrometry (ICP-MS) for Quantitative Analysis in Environmental and Life Sciences: A Review of Challenges, Solutions, and Trends,” *Applied Spectroscopy*, vol. 66, no. 8, pp. 843–868, 2012.
- [72] J. L. Fernández-Turiel, J. F. Llorens, F. López-Vera, C. Gómez-Artola, I. Morell, and D. Gimeno, “Strategy for water analysis using ICP-MS,” *Fredericus’ Journal of Analytical Chemistry*, vol. 368, no. 6, pp. 601–606, 2000.
- [73] L. Poirier, J. Nelson, D. Leong, L. Berhane, P. Hajdu, and F. Lopez-Linares, “Application of ICP-MS and ICP-OES on the Determination of Nickel, Vanadium, Iron, and Calcium in Petroleum Crude Oils via Direct Dilution,” *Energy & Fuels*, vol. 30, no. 5, pp. 3783–3790, 2016.
- [74] S. C. Wilschefski and M. R. Baxter, “Inductively Coupled Plasma Mass Spectrometry: Introduction to Analytical Aspects,” *The Clinical Biochemist Reviews*, vol. 40, no. 3, pp. 115–133, 2019.
- [75] S. E. Long and R. D. Snook, “Electrochemical pre-concentration technique for use with inductively coupled plasma atomic-emission spectrometry. Part I,” *The Analyst*, vol. 108, no. 1292, p. 1331, 1983.
- [76] D. A. Ogaram and R. D. Snook, “Electrochemical pre-concentration technique for use with inductively coupled plasma atomic-emission spectroscopy. Part II,” *The Analyst*, vol. 109, no. 12, p. 1597, 1984.
- [77] Bergamin F. H., F. J. Krug, E. Zagatto, E. C. Arruda, and C. A. Coutinho,

“On-line electrolytic dissolution of alloys in flow-injection analysis,” *Analytica Chimica Acta*, vol. 190, pp. 177–184, 1986.

- [78] J. E. Castle and J. H. Qiu, “A co-ordinated study of the passivation of alloy steels by plasma source mass spectrometry and x-ray photoelectron spectroscopy—II. growth kinetics of the passive film,” *Corrosion Science*, vol. 29, no. 5, pp. 605–616, 1989.
- [79] J. E. Castle and J. H. Qiu, “A co-ordinated study of the passivation of alloy steels by plasma source mass spectrometry and x-ray photoelectron spectroscopy—1. characterization of the passive film,” *Corrosion Science*, vol. 29, no. 5, pp. 591–603, 1989.
- [80] V. Shkirskiy, P. Maciel, J. Deconinck, and K. Ogle, “On The Time Resolution of the Atomic Emission Spectroelectrochemistry Method,” *Journal of The Electrochemical Society*, vol. 163, no. 3, pp. C37–C44, 2016.
- [81] N. Homazava, A. Ulrich, M. Trottmann, and U. Krähenbühl, “Micro-capillary system coupled to ICP-MS as a novel technique for investigation of micro-corrosion processes,” *Journal of Analytical Atomic Spectrometry*, vol. 22, no. 9, p. 1122, 2007.
- [82] N. Homazava, A. Ulrich, and U. Krähenbühl, “Spatially and time-resolved element-specific in situ corrosion investigations with an online hyphenated microcapillary flow injection inductively coupled plasma mass spectrometry set-up,” *Spectrochimica Acta Part B: Atomic Spectroscopy*, vol. 63, no. 7, pp. 777–783, 2008.
- [83] N. Homazava, A. Shkabko, D. Logvinovich, U. Krähenbühl, and A. Ulrich, “Element-specific in situ corrosion behavior of Zr–Cu–Ni–Al–Nb bulk metallic glass in acidic media studied using a novel microcapillary flow injection inductively coupled plasma mass spectrometry technique,” *Intermetallics*, vol. 16, no. 9, pp. 1066–1072, 2008.
- [84] A. W. Hassel and M. M. Lohrengel, “The scanning droplet cell and its application to structured nanometer oxide films on aluminium,” *Electrochimica Acta*, vol. 42, no. 20-22, pp. 3327–3333, 1997.

- [85] A. Ulrich, N. Ott, A. Tournier-Fillon, N. Homazava, and P. Schmutz, “Investigation of corrosion behavior of biodegradable magnesium alloys using an online-micro-flow capillary flow injection inductively coupled plasma mass spectrometry setup with electrochemical control,” *Spectrochimica Acta Part B: Atomic Spectroscopy*, vol. 66, no. 7, pp. 536–545, 2011.
- [86] N. Ott, P. Schmutz, C. Ludwig, and A. Ulrich, “Local, element-specific and time-resolved dissolution processes on a Mg–Y–RE alloy – Influence of inorganic species and buffering systems,” *Corrosion Science*, vol. 75, pp. 201–211, 2013.
- [87] N. Ott, A. Beni, A. Ulrich, C. Ludwig, and P. Schmutz, “Flow microcapillary plasma mass spectrometry-based investigation of new Al–Cr–Fe complex metallic alloy passivation,” *Talanta*, vol. 120, pp. 230–238, 2014.
- [88] S. O. Klemm, A. A. Topalov, C. A. Laska, and K. J. Mayrhofer, “Coupling of a high throughput microelectrochemical cell with online multielemental trace analysis by ICP-MS,” *Electrochemistry Communications*, vol. 13, no. 12, pp. 1533–1535, 2011.
- [89] S. O. Klemm, J.-C. Schauer, B. Schuhmacher, and A. W. Hassel, “A microelectrochemical scanning flow cell with downstream analytics,” *Electrochimica Acta*, vol. 56, no. 11, pp. 4315–4321, 2011.
- [90] S. O. Klemm, A. Karschin, A. K. Schuppert, A. A. Topalov, A. M. Mingers, I. Katsounaros, and K. J. J. Mayrhofer, “Time and Potential Resolved Dissolution Analysis of Rhodium using a Microelectrochemical Flow Cell Coupled to an ICP-MS,” *Journal of Electroanalytical Chemistry*, vol. 677–680, pp. 50–55, 2012.
- [91] J. Klemm, S. O. Klemm, M. J. Duarte, L. Rossrucker, K. Mayrhofer, and F. U. Renner, “Multi-element-resolved electrochemical corrosion analysis. Part I. Dissolution behavior and passivity of amorphous Fe₅₀Cr₁₅Mo₁₄C₁₅B₆,” *Corrosion Science*, vol. 89, pp. 59–68, 2014.
- [92] K. Ogle and S. Weber, “Anodic Dissolution of 304 Stainless Steel Using

Atomic Emission Spectroelectrochemistry,” *Journal of The Electrochemical Society*, vol. 147, no. 5, pp. 1770–1780, 2000.

- [93] P. Zhou, M. J. Hutchison, J. W. Erning, J. R. Scully, and K. Ogle, “An in situ kinetic study of brass dezincification and corrosion,” *Electrochimica Acta*, vol. 229, pp. 141–154, 2017.
- [94] Y. Xie, D. M. Artymowicz, P. P. Lopes, A. Aiello, D. Wang, J. L. Hart, E. Anber, M. L. Taheri, H. Zhuang, R. C. Newman, and K. Sieradzki, “A percolation theory for designing corrosion-resistant alloys,” *Nature Materials*, pp. 1–5, 2021.
- [95] T. N. Vu, M. Mokaddem, P. Volovitch, and K. Ogle, “The anodic dissolution of zinc and zinc alloys in alkaline solution. II. Al and Zn partial dissolution from 5% Al–Zn coatings,” *Electrochimica Acta*, vol. 74, pp. 130–138, 2012.
- [96] M. Mokaddem, P. Volovitch, and K. Ogle, “The anodic dissolution of zinc and zinc alloys in alkaline solution. I. Oxide formation on electrogalvanized steel,” *Electrochimica Acta*, vol. 55, no. 27, pp. 7867–7875, 2010.
- [97] H. Luo, Z. Li, A. M. Mingers, and D. Raabe, “Corrosion behavior of an equiatomic CoCrFeMnNi high-entropy alloy compared with 304 stainless steel in sulfuric acid solution,” *Corrosion Science*, vol. 134, pp. 131–139, 2018.
- [98] Y. Lou, C. Dai, W. Chang, H. Qian, L. Huang, C. Du, and D. Zhang, “Microbiologically influenced corrosion of FeCoCrNiMo0.1 high-entropy alloys by marine *Pseudomonas aeruginosa*,” *Corrosion Science*, vol. 165, p. 108390, 2020.
- [99] P. Volovitch, I. Gazizzullin, F. Ruel, and K. Ogle, “An atomic emission spectroelectrochemical study of corrosion inhibition: The effect of hexamethylenetetramine on the reaction of mild steel in HCl,” *Corrosion Science*, vol. 53, no. 4, pp. 1362–1368, 2011.
- [100] K. Ogle, S. Morel, and N. Meddahi, “An electrochemical study of the delam-

ination of polymer coatings on galvanized steel,” *Corrosion Science*, vol. 47, no. 8, pp. 2034–2052, 2005.

- [101] S. Cherevko, A. A. Topalov, A. R. Zeradjanin, I. Katsounaros, and K. J. J. Mayrhofer, “Gold dissolution: towards understanding of noble metal corrosion,” *RSC Advances*, vol. 3, no. 37, p. 16516, 2013.
- [102] S. Cherevko, A. R. Zeradjanin, G. P. Keeley, and K. J. J. Mayrhofer, “A Comparative Study on Gold and Platinum Dissolution in Acidic and Alkaline Media,” *Journal of The Electrochemical Society*, vol. 161, no. 12, pp. H822–H830, 2014.
- [103] S. Cherevko, “Stability and dissolution of electrocatalysts: Building the bridge between model and “real world” systems,” *Current Opinion in Electrochemistry*, vol. 8, pp. 118–125, 2018.
- [104] O. Kasian, S. Geiger, K. J. Mayrhofer, and S. Cherevko, “Electrochemical On-line ICP-MS in Electrocatalysis Research,” *The Chemical Record*, 2018.
- [105] P. Jovanovič, V. S. Šelih, M. Šala, and N. Hodnik, “In situ electrochemical dissolution of platinum and gold in organic-based solvent,” *npj Materials Degradation*, vol. 2, no. 1, pp. 1–4, 2018.
- [106] N. Hodnik, P. Jovanovič, A. Pavlišič, B. Jozinović, M. Zorko, M. Bele, V. S. Šelih, M. Šala, S. Hočevar, and M. Gaberšček, “New Insights into Corrosion of Ruthenium and Ruthenium Oxide Nanoparticles in Acidic Media,” *The Journal of Physical Chemistry C*, vol. 119, no. 18, pp. 10140–10147, 2015.
- [107] M. Gatalo, P. Jovanovič, U. Petek, M. Šala, V. S. Šelih, F. Ruiz-Zepeda, M. Bele, N. Hodnik, and M. Gaberšček, “Comparison of Pt–Cu/C with Benchmark Pt–Co/C: Metal Dissolution and Their Surface Interactions,” *ACS Applied Energy Materials*, vol. 2, no. 5, pp. 3131–3141, 2019.
- [108] J. D. Henderson, X. Li, D. W. Shoesmith, J. J. Noël, and K. Ogle, “Molybdenum surface enrichment and release during transpassive dissolution of Ni-based alloys,” *Corrosion Science*, vol. 147, pp. 32–40, 2019.
- [109] S. Cherevko, A. A. Topalov, I. Katsounaros, and K. J. Mayrhofer, “Electro-

chemical dissolution of gold in acidic medium,” *Electrochemistry Communications*, vol. 28, pp. 44–46, 2013.

- [110] D. Dworschak, C. Brunnhofer, and M. Valtiner, “Photocorrosion of ZnO Single Crystals during Electrochemical Water Splitting,” *ACS Applied Materials & Interfaces*, vol. 12, no. 46, pp. 51530–51536, 2020.
- [111] M. Fekete, W. Riedel, A. F. Patti, and L. Spiccia, “Photoelectrochemical Water Oxidation by Screen Printed ZnO Nanoparticle Films: Effect of pH on Catalytic Activity and Stability,” *Nanoscale*, vol. 6, no. 13, pp. 7585–7593, 2014.
- [112] A. Hakimian, S. McWilliams, and A. Ignaszak, “ZnO Synthesized Using Bipolar Electrochemistry: Structure and Activity,” *Materials*, vol. 12, no. 3, p. 535, 2019.
- [113] J. Jiang, Y. Wang, W. Ren, Y. Xie, and Y. Chen, “Surface Modification of ZnO Microrod Arrays Films by Ion-Exchange Approach and their Photoelectrochemical Performances,” *International Journal of Hydrogen Energy*, vol. 43, no. 30, pp. 13931–13938, 2018.
- [114] V. Srikant and D. R. Clarke, “On the Optical Band Gap of Zinc Oxide,” *Journal of Applied Physics*, vol. 83, no. 10, pp. 5447–5451, 1998.
- [115] L. G. da Trindade, G. B. Minervino, A. B. Trench, M. H. Carvalho, M. Assis, M. S. Li, A. J. de Oliveira, E. C. Pereira, T. M. Mazzo, and E. Longo, “Influence of Ionic Liquid on the Photoelectrochemical Properties of ZnO Particles,” *Ceramics International*, vol. 44, no. 9, pp. 10393–10401, 2018.
- [116] H. N. Hieu, N. M. Vuong, and D. Kim, “Optimization of CdS/ZnO Electrode for Use in Photoelectrochemical Cell,” *Journal of The Electrochemical Society*, vol. 160, no. 11, pp. H852–H857, 2013.
- [117] S. Ida, K. Yamada, T. Matsunaga, H. Hagiwara, T. Ishihara, T. Taniguchi, M. Koinuma, and Y. Matsumoto, “Photoelectrochemical Hydrogen Production from Water Using p-Type $CaFe_2O_4$ and n-Type ZnO,” *Electrochemistry*, vol. 79, no. 10, pp. 797–800, 2011.

- [118] N. Kislov, J. Lahiri, H. Verma, D. Y. Goswami, E. Stefanakos, and M. Batzill, “Photocatalytic Degradation of Methyl Orange over Single Crystalline ZnO: Orientation Dependence of Photoactivity and Photostability of ZnO,” *Langmuir*, vol. 25, no. 5, pp. 3310–3315, 2009.
- [119] H. Mandal, S. Shyamal, P. Hajra, B. Samanta, P. Fageria, S. Pande, and C. Bhattacharya, “Improved Photoelectrochemical Water Oxidation using Wurtzite ZnO Semiconductors Synthesized through Simple Chemical Bath Reaction,” *Electrochimica Acta*, vol. 141, pp. 294–301, 2014.
- [120] D. Yolaçan and N. Demirci Sankir, “Enhanced Photoelectrochemical and Photocatalytic Properties of 3D-hierarchical ZnO Nanostructures,” *Journal of Alloys and Compounds*, vol. 726, pp. 474–483, 2017.
- [121] A. R. Marder, “The Metallurgy of Zinc-coated Steel,” *Progress in Materials Science*, vol. 45, no. 3, pp. 191–271, 2000.
- [122] P. Spathis and I. Poulios, “The Corrosion and Photocorrosion of Zinc and Zinc Oxide Coatings,” *Corrosion Science*, vol. 37, no. 5, pp. 673–680, 1995.
- [123] X. G. Zhang, *Corrosion and Electrochemistry of Zinc*. New York and London: Plenum, 1996.
- [124] M. Valtiner, S. Borodin, and G. Grundmeier, “Stabilization and Acidic Dissolution Mechanism of Single-Crystalline ZnO(0001) Surfaces in Electrolytes Studied by In-Situ AFM Imaging and Ex-Situ LEED,” *Langmuir*, vol. 24, no. 10, pp. 5350–5358, 2008.
- [125] M. Valtiner, S. Borodin, and G. Grundmeier, “Preparation and Characterisation of Hydroxide Stabilised ZnO(0001)–Zn–OH Surfaces,” *Physical Chemistry Chemical Physics*, vol. 9, no. 19, pp. 2406–2412, 2007.
- [126] M. Valtiner, M. Todorova, G. Grundmeier, and J. Neugebauer, “Temperature Stabilized Surface Reconstructions at Polar ZnO(0001),” *Physical Review Letters*, vol. 103, no. 6, p. 065502, 2009.
- [127] M. Valtiner, X. Torrelles, A. Pareek, S. Borodin, H. Gies, and G. Grundmeier, “In Situ Study of the Polar ZnO(0001)–Zn Surface in Alkaline Elec-

trolytes,” *The Journal of Physical Chemistry C*, vol. 114, no. 36, pp. 15440–15447, 2010.

- [128] G. Kresse, O. Dulub, and U. Diebold, “Competing Stabilization Mechanism for the Polar ZnO(0001)-Zn Surface,” *Physical Review B*, vol. 68, no. 24, p. 245409, 2003.
- [129] N. J. Nicholas, W. Ducker, and G. V. Franks, “Differential Etching of ZnO Native Planes under Basic Conditions,” *Langmuir*, vol. 28, no. 13, pp. 5633–5641, 2012.
- [130] U. Diebold, L. Koplitz, and O. Dulub, “Atomic-Scale Properties of Low-Index ZnO Surfaces,” *Applied Surface Science*, vol. 237, no. 1-4, pp. 336–342, 2004.
- [131] O. Dulub, U. Diebold, and G. Kresse, “Novel Stabilization Mechanism on Polar Surfaces: ZnO(0001)-Zn,” *Physical Review Letters*, vol. 90, no. 1, p. 016102, 2003.
- [132] B. Meyer and D. Marx, “Density-functional Study of the Structure and Stability of ZnO Surfaces,” *Physical Review B*, vol. 67, no. 3, p. 035403, 2003.
- [133] N. J. Nicholas, G. V. Franks, and W. A. Ducker, “The Mechanism for Hydrothermal Growth of Zinc Oxide,” *CrystEngComm*, vol. 14, no. 4, pp. 1232–1240, 2012.
- [134] N. R. D’Amico, G. Cantele, and D. Ninno, “First-Principles Calculations of Clean and Defected ZnO Surfaces,” *The Journal of Physical Chemistry C*, vol. 116, no. 40, pp. 21391–21400, 2012.
- [135] W. Göpel and U. Lampe, “Influence of Defects on the Electronic Structure of Zinc Oxide Surfaces,” *Physical Review B*, vol. 22, no. 12, pp. 6447–6462, 1980.
- [136] M. Tayebi, A. Tayyebi, Z. Masoumi, and B.-K. Lee, “Photocorrosion Suppression and Photoelectrochemical (PEC) Enhancement of ZnO via Hybridization with Graphene Nanosheets,” *Applied Surface Science*, vol. 502, p. 144189, 2020.

- [137] A. Serrà, Y. Zhang, B. Sepúlveda, E. Gómez, J. Nogués, J. Michler, and L. Philippe, “Highly Active ZnO-based Biomimetic Fern-like Microleaves for Photocatalytic Water Decontamination using Sunlight,” *Applied Catalysis B: Environmental*, vol. 248, pp. 129–146, 2019.
- [138] A. Tayyebi, T. Soltani, B.-K. Lee, M. Outokesh, and M. Tayebi, “Novel Visible Light Photocatalytic and Photoelectrochemical (PEC) Activity of Carbon-doped Zinc Oxide/Reduced Graphene Oxide: Supercritical Methanol Synthesis with Enhanced Photocorrosion Suppression,” *Journal of Alloys and Compounds*, vol. 723, pp. 1001–1010, 2017.
- [139] M. Najam Khan, M. Al-Hinai, A. Al-Hinai, and J. Dutta, “Visible Light Photocatalysis of Mixed Phase Zinc Stannate/Zinc Oxide Nanostructures Precipitated at Room Temperature in Aqueous Media,” *Ceramics International*, vol. 40, no. 6, pp. 8743–8752, 2014.
- [140] B. Beverskog and I. Puigdomenech, “Revised Pourbaix Diagrams for Zinc at 25–300 °C,” *Corrosion Science*, vol. 39, no. 1, pp. 107–114, 1997.
- [141] M. Nyberg, M. A. Nygren, L. G. M. Pettersson, D. H. Gay, and A. L. Rohl, “Hydrogen Dissociation on Reconstructed ZnO Surfaces,” *The Journal of Physical Chemistry*, vol. 100, no. 21, pp. 9054–9063, 1996.
- [142] T. Becker, St. Hövel, M. Kunat, C. Boas, U. Burghaus, and C. Wöll, “Interaction of Hydrogen with Metal Oxides: the Case of the Polar ZnO(0001) Surface,” *Surface Science*, vol. 486, no. 3, pp. L502–L506, 2001.
- [143] D. Dworschak, H.-W. Cheng, C.-S. Ku, C.-Y. Chiang, C.-H. Lin, and M. Valtiner, “Comparison of Elemental Resolved non-confined and restricted electrochemical degradation of Nickel Base Alloys,” *Corrosion Science*, p. 109629, 2021.
- [144] S. J. Rosenberg, *Nickel and its alloys*. Washington: National Bureau of Standards, 1968.
- [145] A. F. Rowcliffe, L. K. Mansur, D. T. Hoelzer, and R. K. Nanstad, “Perspec-

tives on radiation effects in nickel-base alloys for applications in advanced reactors,” *Journal of Nuclear Materials*, vol. 392, no. 2, pp. 341–352, 2009.

- [146] M. B. Henderson, D. Arrell, R. Larsson, M. Heobel, and G. Marchant, “Nickel based superalloy welding practices for industrial gas turbine applications,” *Science and Technology of Welding and Joining*, vol. 9, no. 1, pp. 13–21, 2004.
- [147] S. Y. Persaud, B. Langelier, A. Korinek, S. Ramamurthy, G. A. Botton, and R. C. Newman, “Characterization of initial intergranular oxidation processes in alloy 600 at a sub-nanometer scale,” *Corrosion Science*, vol. 133, pp. 36–47, 2018.
- [148] J. R. Hayes, J. J. Gray, A. W. Szmodis, and C. A. Orme, “Influence of Chromium and Molybdenum on the Corrosion of Nickel-Based Alloys,” *CORROSION*, vol. 62, no. 6, pp. 491–500, 2006.
- [149] A. C. Lloyd, J. J. Noël, S. McIntyre, and D. W. Shoesmith, “Cr, Mo and W alloying additions in Ni and their effect on passivity,” *Electrochimica Acta*, vol. 49, no. 17-18, pp. 3015–3027, 2004.
- [150] N. Ebrahimi, P. Jakupi, J. J. Noël, and D. W. Shoesmith, “The Role of Alloying Elements on the Crevice Corrosion Behavior of Ni-Cr-Mo Alloys,” *CORROSION*, vol. 71, no. 12, pp. 1441–1451, 2015.
- [151] S. Y. Persaud and R. C. Newman, “A Review of Oxidation Phenomena in Ni Alloys Exposed to Hydrogenated Steam Below 500°C,” *CORROSION*, vol. 72, no. 7, pp. 881–896, 2016.
- [152] N. Ebrahimi, M. C. Biesinger, D. W. Shoesmith, and J. J. Noël, “The influence of chromium and molybdenum on the repassivation of nickel-chromium-molybdenum alloys in saline solutions: Influence of Cr and Mo on the Repassivation of Ni-Cr-Mo Alloys,” *Surface and Interface Analysis*, vol. 49, no. 13, pp. 1359–1365, 2017.
- [153] H.-H. Huang, “Effect of chemical composition on the corrosion behavior of

Ni-Cr-Mo dental casting alloys,” *Journal of Biomedical Materials Research*, vol. 60, no. 3, pp. 458–465, 2002.

- [154] J. Zhang, Y. Chen, and M. A. Brook, “Facile functionalization of PDMS elastomer surfaces using thiol-ene click chemistry,” *Langmuir*, vol. 29, no. 40, pp. 12432–12442, 2013.
- [155] N. Ebrahimi, J. J. Noël, M. A. Rodríguez, and D. W. Shoesmith, “The self-sustaining propagation of crevice corrosion on the hybrid BC1 Ni–Cr–Mo alloy in hot saline solutions,” *Corrosion Science*, vol. 105, pp. 58–67, 2016.
- [156] S. Voyshnis, A. Seyeux, S. Zanna, B. Martin-Cabanas, T. Couvant, and P. Marcus, “Oxide layer growth on nickel-base alloy surfaces in high temperature water and in O₂ studied by ToF-SIMS with isotopic tracers,” *Corrosion Science*, vol. 145, pp. 212–219, 2018.
- [157] A. C. Lloyd, J. J. Noël, D. W. Shoesmith, and N. S. McIntyre, “The open-circuit ennoblement of alloy C-22 and other Ni–Cr–Mo alloys,” *JOM*, vol. 57, no. 1, pp. 31–35, 2005.
- [158] P. Jakupi, J. J. Noël, and D. W. Shoesmith, “The evolution of crevice corrosion damage on the Ni–Cr–Mo–W alloy-22 determined by confocal laser scanning microscopy,” *Corrosion Science*, vol. 54, pp. 260–269, 2012.
- [159] G. Pajonk and H. Bubert, “Influence of Pickling High Alloyed CrNi-Steels and Nickel Base Alloys with Citric Acid on the Composition of their Tarnish Oxides,” *Microchimica Acta*, vol. 133, no. 1-4, pp. 289–293, 2000.
- [160] X. Li and K. Ogle, “The Passivation of Ni–Cr–Mo Alloys: Time Resolved Enrichment and Dissolution of Cr and Mo during Passive-Active Cycles,” *Journal of The Electrochemical Society*, vol. 166, no. 11, pp. C3179–C3185, 2019.
- [161] A. K. Schuppert, A. A. Topalov, I. Katsounaros, S. O. Klemm, and K. J. J. Mayrhofer, “A Scanning Flow Cell System for Fully Automated Screening of Electrocatalyst Materials,” *Journal of The Electrochemical Society*, vol. 159, no. 11, pp. F670–F675, 2012.

- [162] K. S. Kim and N. Winograd, “X-ray photoelectron spectroscopic studies of nickel-oxygen surfaces using oxygen and argon ion-bombardment,” *Surface Science*, vol. 43, no. 2, pp. 625–643, 1974.
- [163] M. C. Biesinger, B. P. Payne, A. P. Grosvenor, L. W. Lau, A. R. Gerson, and R. S. Smart, “Resolving surface chemical states in XPS analysis of first row transition metals, oxides and hydroxides: Cr, Mn, Fe, Co and Ni,” *Applied Surface Science*, vol. 257, no. 7, pp. 2717–2730, 2011.
- [164] J. Baltrusaitis, B. Mendoza-Sanchez, V. Fernandez, R. Veenstra, N. Dukstiene, A. Roberts, and N. Fairley, “Generalized molybdenum oxide surface chemical state XPS determination via informed amorphous sample model,” *Applied Surface Science*, vol. 326, pp. 151–161, 2015.
- [165] C. R. Clayton and Y. C. Lu, “Electrochemical and XPS evidence of the aqueous formation of Mo₂O₅,” *Surface and Interface Analysis*, vol. 14, no. 1-2, pp. 66–70, 1989.
- [166] A. P. Grosvenor, M. C. Biesinger, R. S. Smart, and N. S. McIntyre, “New interpretations of XPS spectra of nickel metal and oxides,” *Surface Science*, vol. 600, no. 9, pp. 1771–1779, 2006.
- [167] M. Volmer, M. Stratmann, and H. Viehhaus, “Electrochemical and electron spectroscopic investigations of iron surfaces modified with thiols,” *Surface and Interface Analysis*, vol. 16, no. 1-12, pp. 278–282, 1990.
- [168] J.-J. Velasco-Vélez, L. J. Falling, D. Bernsmeier, M. J. Sear, P. C. J. Clark, T.-S. Chan, E. Stotz, M. Hävecker, R. Kraehnert, A. Knop-Gericke, C.-H. Chuang, D. E. Starr, M. Favaro, and R. V. Mom, “A comparative study of electrochemical cells for in situ x-ray spectroscopies in the soft and tender x-ray range,” *Journal of Physics D: Applied Physics*, vol. 54, no. 12, p. 124003, 2021.
- [169] S. Pletincx, S. Abrahami, J. Mol, T. Hauffman, and H. Terryn, “Advanced (In Situ) Surface Analysis of Organic Coating/Metal Oxide Interactions for Corrosion Protection of Passivated Metals,” in *Encyclopedia of interfacial chemistry*, pp. 1–17, San Diego: Elsevier Science, 2018.

- [170] M. A. Khillah, H. Mikhail, A. Abu-El Soud, and Z. M. Hanafi, “Magnetic susceptibility of molybdenum trioxide, dioxide and some suboxides,” *Czechoslovak Journal of Physics*, vol. 30, no. 9, pp. 1039–1045, 1980.
- [171] N. Cabrera and N. F. Mott, “Theory of the oxidation of metals,” *Reports on Progress in Physics*, vol. 12, no. 1, pp. 163–184, 1949.
- [172] L. F. Lin, C. Y. Chao, and D. D. Macdonald, “A Point Defect Model for Anodic Passive Films: II . Chemical Breakdown and Pit Initiation,” *Journal of The Electrochemical Society*, vol. 128, no. 6, pp. 1194–1198, 1981.
- [173] L. Zha, H. Li, and N. Wang, “In Situ Electrochemical Study of the Growth Kinetics of Passive Film on TC11 Alloy in Sulfate Solution at 300 °C/10 MPa,” *Materials*, vol. 13, no. 5, 2020.
- [174] Z. Wang, E.-M. Paschalidou, A. Seyeux, S. Zanna, V. Maurice, and P. Marcus, “Mechanisms of Cr and Mo Enrichments in the Passive Oxide Film on 316L Austenitic Stainless Steel,” *Frontiers in Materials*, vol. 6, 2019.
- [175] R. G. Kelly and J. S. Lee, “Localized Corrosion: Crevice Corrosion,” in *Encyclopedia of interfacial chemistry*, pp. 291–301, San Diego: Elsevier Science, 2018.
- [176] M. Nie, J. A. Wharton, A. Cranny, N. R. Harris, R. J. K. Wood, and K. R. Stokes, “Characterisation of Crevice and Pit Solution Chemistries Using Capillary Electrophoresis with Contactless Conductivity Detector,” *Materials*, vol. 6, no. 10, pp. 4345–4360, 2013.
- [177] T. Kaji, T. Sekiai, I. Muto, Y. Sugawara, and N. Hara, “Visualization of Solution Chemistry inside Crevice by pH and pCl Sensing Plates,” *ECS Transactions*, vol. 41, no. 25, pp. 205–216, 2019.
- [178] N. J. Laycock, J. Stewart, and R. C. Newman, “The initiation of crevice corrosion in stainless steels,” *Corrosion Science*, vol. 39, no. 10-11, pp. 1791–1809, 1997.
- [179] C. Merola, H.-W. Cheng, D. Dworschak, C.-S. Ku, C.-Y. Chiang, F. U. Renner, and M. Valtiner, “Nanometer Resolved Real Time Visualization of

Acidification and Material Breakdown in Confinement,” *Advanced Materials Interfaces*, vol. 6, no. 10, p. 1802069, 2019.

- [180] N. Sridhar, “Local Corrosion Chemistry—A Review,” *CORROSION*, vol. 73, no. 1, pp. 18–30, 2017.
- [181] K. Lutton Cwalina, C. R. Demarest, A. Y. Gerard, and J. R. Scully, “Revisiting the effects of molybdenum and tungsten alloying on corrosion behavior of nickel-chromium alloys in aqueous corrosion,” *Current Opinion in Solid State and Materials Science*, vol. 23, no. 3, pp. 129–141, 2019.
- [182] N. Sridhar and D. S. Dunn, “Effect of Applied Potential on Changes in Solution Chemistry Inside Crevices on Type 304L Stainless Steel and Alloy 825,” *CORROSION*, vol. 50, no. 11, 1994.
- [183] B. T. Lu, J. L. Luo, and Y. C. Lu, “A Mechanistic Study on Lead-Induced Passivity-Degradation of Nickel-Based Alloy,” *Journal of The Electrochemical Society*, vol. 154, no. 8, p. C379, 2007.
- [184] S. J. Rosenberg, *Nickel and its alloys*. National Bureau of Standards, 1968.
- [185] A. Rowcliffe, L. Mansur, D. Hoelzer, and R. Nanstad, “Perspectives on radiation effects in nickel-base alloys for applications in advanced reactors,” *Journal of Nuclear Materials*, vol. 392, pp. 341–352, July 2009.
- [186] S. Persaud, B. Langelier, A. Korinek, S. Ramamurthy, G. Botton, and R. Newman, “Characterization of initial intergranular oxidation processes in alloy 600 at a sub-nanometer scale,” *Corrosion Science*, vol. 133, pp. 36–47, Apr. 2018.
- [187] N. Ebrahimi, P. Jakupi, J. Noël, and D. Shoesmith, “The Role of Alloying Elements on the Crevice Corrosion Behavior of Ni-Cr-Mo Alloys,” *CORROSION*, vol. 71, pp. 1441–1451, Sept. 2015.
- [188] S. Persaud and R. Newman, “A Review of Oxidation Phenomena in Ni Alloys Exposed to Hydrogenated Steam Below 500°C,” *Corrosion*, vol. 72, pp. 881–896, July 2016.
- [189] V. Maurice and P. Marcus, “Current developments of nanoscale insight into

corrosion protection by passive oxide films,” *Current Opinion in Solid State and Materials Science*, vol. 22, no. 4, pp. 156–167, 2018.

- [190] A. Galtayries, A. Machet, P. Jolivet, P. Scott, M. Foucault, P. Combrade, and P. Marcus, “Kinetics of passivation of nickel-base alloys (Alloy 600 and Alloy 690) in high temperature water,” in *Passivation of metals and semi-conductors, and properties of thin oxide layers* (P. Marcus and V. Maurice, eds.), pp. 403–409, Amsterdam and Oxford: Elsevier, 2006.
- [191] S. Marcelin, B. Ter-Ovanesian, and B. Normand, “Electronic properties of passive films from the multi-frequency Mott–Schottky and power-law coupled approach,” *Electrochemistry Communications*, vol. 66, pp. 62–65, 2016.
- [192] Y. Mito, M. Ueda, and T. Ohtsuka, “Photo-luminescence from passive oxide films on nickel and chromium by photo-excitation of UV light,” *Corrosion Science*, vol. 51, no. 7, pp. 1540–1544, 2009.
- [193] H. Tsuchiya, S. Fujimoto, O. Chihara, and T. Shibata, “Semiconductive behavior of passive films formed on pure Cr and Fe–Cr alloys in sulfuric acid solution,” *Electrochimica Acta*, vol. 47, no. 27, pp. 4357–4366, 2002.
- [194] C. Y. Chao, L. F. Lin, and D. D. Macdonald, “A Point Defect Model for Anodic Passive Films: I . Film Growth Kinetics,” *Journal of The Electrochemical Society*, vol. 128, no. 6, pp. 1187–1194, 1981.
- [195] G. Tranchida, M. Clesi, F. Di Franco, F. Di Quarto, and M. Santamaria, “Electronic properties and corrosion resistance of passive films on austenitic and duplex stainless steels,” *Electrochimica Acta*, vol. 273, pp. 412–423, 2018.
- [196] Y. Shi, L. Collins, N. Balke, P. Liaw, and B. Yang, “In-situ electrochemical-afm study of localized corrosion of $\text{Al}_x\text{CoCrFeNi}$ high-entropy alloys in chloride solution,” *Applied Surface Science*, vol. 439, 05 2018.
- [197] X. Deng, F. Galli, and M. Koper, “In situ electrochemical afm imaging of a pt electrode in sulfuric acid under potential cycling conditions,” *Journal of the American Chemical Society*, vol. 140, 09 2018.
- [198] V. Maurice, T. Nakamura, L. Klein, and P. Marcus, “7 - Initial stages of

localised corrosion by pitting of passivated nickel surfaces studied by scanning tunnelling microscopy (STM) and atomic force microscopy (AFM),” in *Local Probe Techniques for Corrosion Research* (R. Oltra, V. Maurice, R. Akid, and P. Marcus, eds.), European Federation of Corrosion (EFC) Series, pp. 71–83, Woodhead Publishing, 2007.

- [199] B. Beverskog and I. Puigdomenech, “Revised pourbaix diagrams for iron at 25–300 °C,” *Corrosion Science*, vol. 38, pp. 2121–2135, Dec. 1996.
- [200] O. Azzaroni, M. Cipollone, M. E. Vela, and R. C. Salvarezza, “Protective Properties of Dodecanethiol Layers on Copper Surfaces: The Effect of Chloride Anions in Aqueous Environments,” *Langmuir*, vol. 17, no. 5, pp. 1483–1487, 2001.
- [201] W. Possart, “Adhesion and Interphases: The Basic Ideas in Brief,” in *Adhesive joints* (W. Possart and M. Brede, eds.), pp. 1–42, Weinheim: Wiley-VCH, 2019.
- [202] P. Thissen, M. Valtiner, and G. Grundmeier, “Stability of phosphonic acid self-assembled monolayers on amorphous and single-crystalline aluminum oxide surfaces in aqueous solution,” *Langmuir : the ACS journal of surfaces and colloids*, vol. 26, no. 1, pp. 156–164, 2010.
- [203] G. Grundmeier, C. Reinartz, M. Rohwerder, and M. Stratmann, “Corrosion properties of chemically modified metal surfaces,” *Electrochimica Acta*, vol. 43, no. 1-2, pp. 165–174, 1998.
- [204] C. Vericat, M. E. Vela, G. Benitez, P. Carro, and R. C. Salvarezza, “Self-assembled monolayers of thiols and dithiols on gold: new challenges for a well-known system,” *Chemical Society Reviews*, vol. 39, no. 5, pp. 1805–1834, 2010.
- [205] L. Srisombat, A. C. Jamison, and T. R. Lee, “Stability: A key issue for self-assembled monolayers on gold as thin-film coatings and nanoparticle protectants,” *Colloids and Surfaces A: Physicochemical and Engineering Aspects*, vol. 390, no. 1-3, pp. 1–19, 2011.

- [206] M. Grandbois, M. Beyer, M. Rief, H. Clausen-Schaumann, and H. E. Gaub, “How strong is a covalent bond?,” *Science (New York, N.Y.)*, vol. 283, no. 5408, pp. 1727–1730, 1999.
- [207] Y.-F. Liu, Y.-C. Yang, and Y.-L. Lee, “Assembly behavior and monolayer characteristics of OH-terminated alkanethiol on Au(111): in situ scanning tunneling microscopy and electrochemical studies,” *Nanotechnology*, vol. 19, no. 6, p. 065609, 2008.
- [208] T. Kakiuchi, M. Iida, N. Gon, D. Hobarra, S.-i. Imabayashi, and K. Niki, “Miscibility of Adsorbed 1-Undecanethiol and 11-Mercaptoundecanoic Acid Species in Binary Self-Assembled Monolayers on Au(111),” *Langmuir*, vol. 17, no. 5, pp. 1599–1603, 2001.
- [209] G. Corthey, A. A. Rubert, G. A. Benitez, M. H. Fonticelli, and R. C. Salvarezza, “Electrochemical and X-ray Photoelectron Spectroscopy Characterization of Alkanethiols Adsorbed on Palladium Surfaces,” *The Journal of Physical Chemistry C*, vol. 113, no. 16, pp. 6735–6742, 2009.
- [210] H. Wano and K. Uosaki, “In Situ, Real-Time Monitoring of the Reductive Desorption Process of Self-Assembled Monolayers of Hexanethiol on Au(111) Surfaces in Acidic and Alkaline Aqueous Solutions by Scanning Tunneling Microscopy,” *Langmuir*, vol. 17, no. 26, pp. 8224–8228, 2001.
- [211] M. E. Vela, H. Martin, C. Vericat, G. Andreasen, A. Hernández Creus, and R. C. Salvarezza, “Electrodesorption Kinetics and Molecular Interactions in Well-Ordered Thiol Adlayers On Au(111),” *The Journal of Physical Chemistry B*, vol. 104, no. 50, pp. 11878–11882, 2000.
- [212] Y. Chen, C. Yang, and F.-B. Wang, “Electrochemical assessment of electrochemical oxidation stability of self-assembled monolayers on gold and preparation of binary self-assembled monolayers on gold,” *Electrochimica Acta*, vol. 55, no. 12, pp. 3951–3956, 2010.
- [213] S. N. Ovchinnikova and A. Z. Medvedev, “Desorption of octanethiol from gold electrode surface during its electrochemical cleaning,” *Russian Journal of Electrochemistry*, vol. 51, no. 4, pp. 287–293, 2015.

- [214] L. Jiang, P. Volovitch, M. Wolpers, and K. Ogle, “Activation and inhibition of Zn–Al and Zn–Al–Mg coatings on steel by nitrate in phosphoric acid solution,” *Corrosion Science*, vol. 60, pp. 256–264, 2012.
- [215] M. Hegner, P. Wagner, and G. Semenza, “Ultralarge atomically flat template-stripped Au surfaces for scanning probe microscopy,” *Surf. Sci.*, vol. 291, pp. 39–46, Jul 1993.
- [216] L. Chai and J. Klein, “Large Area, Molecularly Smooth (0.2 nm rms) Gold Films for Surface Forces and Other Studies,” *Langmuir*, vol. 23, no. 14, pp. 7777–7783, 2007.
- [217] A. Shaheen, J. M. Sturm, R. Ricciardi, J. Huskens, C. J. Lee, and F. Bijk-erk, “Characterization of Self-Assembled Monolayers on a Ruthenium Sur-face,” *Langmuir : the ACS journal of surfaces and colloids*, vol. 33, no. 25, pp. 6419–6426, 2017.
- [218] B. Moores, J. Simons, S. Xu, and Z. Leonenko, “AFM-assisted fabrication of thiol SAM pattern with alternating quantified surface potential,” *Nanoscale Research Letters*, vol. 6, no. 1, p. 185, 2011.
- [219] S. Xu, S. J. N. Cruchon-Dupeyrat, J. C. Garno, G.-Y. Liu, G. Kane Jennings, T.-H. Yong, and P. E. Laibinis, “In situ studies of thiol self-assembly on gold from solution using atomic force microscopy,” *The Journal of Chemical Physics*, vol. 108, no. 12, pp. 5002–5012, 1998.
- [220] J.-W. Yeh, S.-K. Chen, S.-J. Lin, J.-Y. Gan, T.-S. Chin, T.-T. Shun, C.-H. Tsau, and S.-Y. Chang, “Nanostructured High-Entropy Alloys with Multiple Principal Elements: Novel Alloy Design Concepts and Outcomes,” *Advanced Engineering Materials*, vol. 6, no. 5, pp. 299–303, 2004.
- [221] C.-Y. Cheng, Y.-C. Yang, Y.-Z. Zhong, Y.-Y. Chen, T. Hsu, and J.-W. Yeh, “Physical metallurgy of concentrated solid solutions from low-entropy to high-entropy alloys,” *Current Opinion in Solid State and Materials Science*, vol. 21, no. 6, pp. 299–311, 2017.
- [222] Y. J. Li, A. Savan, A. Kostka, H. S. Stein, and A. Ludwig, “Accelerated

atomic-scale exploration of phase evolution in compositionally complex materials,” *Materials Horizons*, vol. 5, no. 1, pp. 86–92, 2018.

- [223] J. Dąbrowa, M. Stygar, A. Mięka, A. Knapik, K. Mroczka, W. Tejchman, M. Danielewski, and M. Martin, “Synthesis and microstructure of the (co, cr, fe, mn, ni) 3o_4 high entropy oxide characterized by spinel structure,” *Materials Letters*, vol. 216, pp. 32–36, 2018.
- [224] C. Schwanke, H. S. Stein, L. Xi, K. Sliozberg, W. Schuhmann, A. Ludwig, and K. M. Lange, “Correlating oxygen evolution catalysts activity and electronic structure by a high-throughput investigation of ni $1\text{-yz fe y cr z o x}$,” *Scientific reports*, vol. 7, no. 1, pp. 1–7, 2017.
- [225] A. Sarkar, L. Velasco, D. Wang, Q. Wang, G. Talasila, L. de Biasi, C. Kübel, T. Brezesinski, S. S. Bhattacharya, H. Hahn, *et al.*, “High entropy oxides for reversible energy storage,” *Nature communications*, vol. 9, no. 1, pp. 1–9, 2018.
- [226] Y. Yuan, Y. Wu, H. Luo, Z. Wang, X. Liang, Z. Yang, H. Wang, X. Liu, and Z. Lu, “Superconducting $\text{Ti}_{15}\text{Zr}_{15}\text{Nb}_{35}\text{Ta}_{35}$ High-Entropy Alloy With Intermediate Electron-Phonon Coupling,” *Frontiers in Materials*, vol. 5, 2018.
- [227] J.-W. Yeh, “Alloy design strategies and future trends in high-entropy alloys,” *Jom*, vol. 65, no. 12, pp. 1759–1771, 2013.
- [228] Y. Y. Chen, T. Duval, U. D. Hung, J. W. Yeh, and H. C. Shih, “Microstructure and electrochemical properties of high entropy alloys—a comparison with type-304 stainless steel,” *Corrosion Science*, vol. 47, no. 9, pp. 2257–2279, 2005.
- [229] K.-Y. Tsai, M.-H. Tsai, and J.-W. Yeh, “Sluggish diffusion in Co–Cr–Fe–Mn–Ni high-entropy alloys,” *Acta Materialia*, vol. 61, no. 13, pp. 4887–4897, 2013.
- [230] Y. Zhang, K. Jin, H. Xue, C. Lu, R. J. Olsen, L. K. Beland, M. W. Ullah, S. Zhao, H. Bei, D. S. Aidhy, G. D. Samolyuk, L. Wang, M. Caro, A. Caro, G. M. Stocks, B. C. Larson, I. M. Robertson, A. A. Correa, and W. J. Weber,

“Influence of chemical disorder on energy dissipation and defect evolution in advanced alloys,” *Journal of Materials Research*, vol. 31, no. 16, pp. 2363–2375, 2016.

- [231] Q. Ye, K. Feng, Z. Li, F. Lu, R. Li, J. Huang, and Y. Wu, “Microstructure and corrosion properties of CrMnFeCoNi high entropy alloy coating,” *Applied Surface Science*, vol. 396, pp. 1420–1426, 2017.
- [232] Z. Han, W. Ren, J. Yang, A. Tian, Y. Du, G. Liu, R. Wei, G. Zhang, and Y. Chen, “The corrosion behavior of ultra-fine grained conifecrmn high-entropy alloys,” *Journal of Alloys and Compounds*, vol. 816, p. 152583, 2020.
- [233] A. M. Panindre, Y. Khalifa, C. D. Taylor, and G. S. Frankel, “Corrosion of Ni-Fe-Cr-Mo-W-X Multi-Principal Element Alloys,” *Journal of The Electrochemical Society*, vol. 168, no. 3, p. 031513, 2021.
- [234] K. H. Kim, S. H. Lee, N. D. Nam, and J. G. Kim, “Effect of cobalt on the corrosion resistance of low alloy steel in sulfuric acid solution,” *Corrosion Science*, vol. 53, no. 11, pp. 3576–3587, 2011.
- [235] N. Birbilis, S. Choudhary, J. R. Scully, and M. L. Taheri, “A perspective on corrosion of multi-principal element alloys,” *npj Materials Degradation*, vol. 5, no. 1, 2021.
- [236] H. Stein, M. Suta, and J. George, “Die Materialsynthesemaschine,” *Nachrichten aus der Chemie*, vol. 68, no. 12, pp. 66–69, 2020.
- [237] E. Soedarmadji, H. S. Stein, S. K. Suram, D. Guevarra, and J. M. Gregoire, “Tracking materials science data lineage to manage millions of materials experiments and analyses,” *npj Computational Materials*, vol. 5, no. 1, 2019.
- [238] H. Baker and H. Okamoto, “ASM handbook. vol. 3. Alloy Phase Diagrams,” *ASM International, Materials Park, Ohio 44073-0002, USA, 1992. 501, 1992.*

List of Figures

1.1	Processes on electrified solid-liquid interfaces	6
2.1	POURBAIX diagram of the system $Fe - H_2O$. Reprinted with permission from [23].	9
2.2	Principle of AFM	11
2.3	Rendering of EC-AFM setup	15
2.4	Cut through the EC-AFM setup used	16
2.5	Schematic of an ICP-MS	18
2.6	Electrochemical flow cell with downstream ICP-detection	20
2.7	Time resolution of flow cells with ICP-MS detection	24
2.8	Design of the ICP-MS flow cell	24
3.1	Photocorrosion Study with ICP-MS flow cells	29
3.2	Schematic of ICP-MS flow cell for testing of photocorrosion	31
3.3	Dissolution rates of polar and nonpolar ZnO	34
3.4	Surfaces structures of ZnO	35
3.5	<i>In situ</i> AFM topographies of dissolving ZnO	39
3.6	Ion and electric current of ZnO 0001 during pulsed UV illumination	40
4.1	Schematics of the ICP-MS flow cell and resulting corrosion patterns	45
4.2	Anodic dissolution of Cr5, alloy 600, and Mo1 with and without crevice	50
4.3	Anodic dissolution ratios	51
4.4	Repassivation profiles after 5 and 40 min of anodic dissolution	52
4.5	Surface composition and selected XP spectra	55
4.6	XRF characterisation	57

5.1	Tafel-Plot of Alloy 600 and the used electrochemical cells	65
5.2	Time-resolved, integrated and relative dissolution profiles of passive-active cycles	69
5.3	AFM of (pre-)conditioning-anodic dissolution sequences	72
6.1	Testing of SAMs as corrosion inhibitors	79
6.2	Thiols used for SAM films	83
6.3	<i>Ex situ</i> AFM topographies of SAMs on Au	83
6.4	<i>In situ</i> AFM topographies of SAMs on Au	85
6.5	LSV on SAM covered Au: EC and ICP-MS data	86
7.1	Detail of NPV experiment on NiCoCrFeMn	95
7.2	3D scatter plot (Fe, Cr and Mn axes) of total dissolved mass at indicated step potentials	96
7.3	Dissolved mass per step as function of Cr and Fe concentration	98
7.4	Elemental dissolution rates for selected alloys and elements	102
7.5	Map of the observed Fe dissolution pattern per step potential and alloy	104
8.1	Future setup with EC-AFM and ICP-MS combined, yielding topographic, electrochemical and solution-side elemental dissolution rates almost in real time.	110
A.1.2	Electronic current during polarization of ZnO	A2
A.2.1	Polarization curves for all NBAs	A3
A.2.2	Integrated mass release during repassivation	A4
A.2.3	XPS core level spectra of alloy 600 after passivation and repassivation	A5
A.2.4	XPS core level spectra of alloy Mo1 after passivation and repassivation	A6
A.2.5	XPS core level spectra of alloy Cr5 after passivation and repassivation	A7
A.2.6	XPS core level spectra of alloy 600 at 1.0 V	A8
A.2.7	XPS core level spectra of alloy Mo1 at 1.0 V	A9
A.3.1	Elemental dissolution ratios during NPV for all alloys	A10
A.3.1	Dissolution of alloys during NPV	A11
A.4.1	Topographies of SAMs on Gold during different stages of the anodic polarisation experiment	A15

List of Tables

4.1	Bulk composition (weight ratios) and abbreviations for all NBAs used.	46
5.1	Root mean square (RMS) values and their relative change of images shown in Fig. 5.3	71

List of publications

In preparation

- [D. Dworschak](#), K.-K. Tseng, J.-W. Yeh, H.-W. Cheng, M. Valtiner, "Bottom-up Characterization of Electrochemical Passivity from Simple Binary Alloys to High Entropy Alloys" (2021)
- [D. Dworschak](#), M. Bishara, H.-W. Cheng, M. Valtiner, "Combining AFM imaging and elementally resolved spectro-electrochemistry for understanding stability and quality of passive films formed on Alloy 600" (2021)

Submitted

- [D. Dworschak](#), C. Brunnhofer, M. Valtiner, "Complementary electrochemical ICP-MS flow cell and in-situ AFM study of the anodic desorption of molecular adhesion promoters", Applied Surface Science (2021)
- P. Bilotto, A. M. Imre, [D. Dworschak](#), L. L. E. Mears, M. Valtiner, "Visualization of ion|surface binding and in situ evaluation of surface interaction free energies via competitive adsorption isotherms", ACS Physical Chemistry Au (2021)

Accepted/Published

- [D. Dworschak](#), H.-W. Cheng, C.-S. Ku, C.-Y. Chiang, C.-H. Lin, M. Valtiner, "[Comparison of Elemental Resolved non-confined and restricted electrochemical degradation of Nickel Base Alloys](#)", Corrosion Science, (2021), *in press*
- [D. Dworschak](#), C. Brunnhofer, M. Valtiner, "Photocorrosion of ZnO Single Crystals during Electrochemical Water Splitting", [ACS Appl. Mater. Interfaces](#) **12** (46), 51530 (2020)
- G. Tiétcha, L. L. E. Mears, [D. Dworschak](#), M. Roth, I. Klüppel, M. Valtiner, "Adsorption and Diffusion Moderated by Polycationic Polymers during Electrodeposition of Zinc". [ACS Appl. Mater. Interfaces](#) **12** (26), 29928 (2020)

- A. S. Racz, D. Dworschak, M. Valtiner, M. Menyhard, Scratching resistance of SiC-rich nano-coatings produced by noble gas ion mixing. [Surface and Coatings Technology](#) **386**, 125475 (2020)
- C. Merola, H.-W. Cheng, D. Dworschak, C.-S. Ku, C.-Y. Chiang, F. U. Renner, M. Valtiner, "Nanometer Resolved Real Time Visualization of Acidification and Material Breakdown in Confinement" [Adv. Mater. Interfaces](#) **6** (10), 1802069 (2019)

Copyright clearances

RightsLink Printable License

18.05.21, 22:15

ELSEVIER LICENSE TERMS AND CONDITIONS

May 18, 2021

This Agreement between Mr. Dominik Dworschak ("You") and Elsevier ("Elsevier") consists of your license details and the terms and conditions provided by Elsevier and Copyright Clearance Center.

License Number	5072081389704
License date	May 18, 2021
Licensed Content Publisher	Elsevier
Licensed Content Publication	Corrosion Science
Licensed Content Title	Potential-pH diagrams at elevated temperature for the system Fe-H ₂ O
Licensed Content Author	H.E. Townsend
Licensed Content Date	Jan 1, 1970
Licensed Content Volume	10
Licensed Content Issue	5

[Print This Page](#)

Die approbierte gedruckte Originalversion dieser Dissertation ist an der TU Wien Bibliothek verfügbar.
The approved original version of this doctoral thesis is available in print at TU Wien Bibliothek.

From: support@services.acs.org
To: [Dworschak, Dominik](#)
Subject: Regarding Incident 4322025 Reuse Permission Request
Date: Monday, 3 May 2021 17:30:07
Attachments: [Image-9471548b0bb2534280ec13437e894be06bbfe38812.png](#)



Dear Dominik Dworschak,

Your permission requested is granted and there is no fee for this reuse.

In your planned reuse, you must cite the ACS article as the source, add this direct link: <https://pubs.acs.org/doi/10.1021/acsami.0c15508> and include a notice to readers that further permission related to the material excerpted should be directed to the ACS.

Please do not hesitate to contact me if you need any further assistance.

Regards,
Jawwad Saeed
ACS Customer Services & Information
<https://help.acs.org>

Incident Information:

Incident #: 4322025
Date Created: 2021-05-03T04:39:57
Priority: 3
Customer: Dominik Dworschak
Title: Reuse Permission Request
Description: Dear Sir or Madam,
I would like to ask for permission to reuse the entire article <https://pubs.acs.org/doi/10.1021/acsami.0c15508> ('Photocorrosion of ZnO Single Crystals during Electrochemical Water Splitting') for my PhD thesis titled "A holistic approach on real-time analysis of electrified solid-liquid interfaces".
Thanks for answering my request.
Kind regards,
Dominik Dworschak

Dominik Dworschak
Applied Interface Physics

Institute of Applied Physics
Vienna University of Technology
Wiedner Hauptstraße 8-10/ E134
A-1040 Wien
Austria

eMail: dworschak@iap.tuwien.ac.at
phone: +43-1-58801-13443



Home



Help



Email Support



Sign in



Create Account



Comparison of Elemental Resolved non-confined and restricted electrochemical degradation of Nickel Base Alloys

Author: Dominik Dworschak, Hsiu-Wei Cheng, Ching-Shun Ku, Ching-Yu Chiang, Chia-Hsien Lin, Markus Valtiner

Publication: Corrosion Science

Publisher: Elsevier

Date: Available online 25 June 2021

© 2021 Published by Elsevier Ltd.

Journal Author Rights

Please note that, as the author of this Elsevier article, you retain the right to include it in a thesis or dissertation, provided it is not published commercially. Permission is not required, but please ensure that you reference the journal as the original source. For more information on this and on your other retained rights, please visit: <https://www.elsevier.com/about/our-business/policies/copyright#Author-rights>

BACK

CLOSE WINDOW

© 2021 Copyright - All Rights Reserved | [Copyright Clearance Center, Inc.](#) | [Privacy statement](#) | [Terms and Conditions](#)
Comments? We would like to hear from you. E-mail us at customercare@copyright.com

Curriculum Vitae

Dominik Dworschak

Ziegelofengasse 27/7/1 • 1050 Wien • Österreich
Tel. +43 670 6076278 • E-Mail: dominik.dworschak@online.de



Lebenslauf

Persönliche Angaben

geboren am 10. Juni 1994 in Dillingen/Donau
Familienstand ledig
Nationalität deutsch

Ausbildung

10/2017 bis vsl. 06/2021 **Doktorat der technischen Wissenschaften/Technische Physik**
Technische Universität Wien
• Schwerpunkt Analytische Chemie, Methodenentwicklung

12/2015 bis 09/2017 **Studium Master Chemie**
Technische Universität Bergakademie Freiberg
• Schwerpunkt Physikalische Chemie
• Spezialisierung Grenzflächenchemie
Titel der Masterarbeit:
„Korrosionsuntersuchungen an Einkristallen mit AFM und ICP-MS“ (Note 1,0) Abschlussnote 1,4

10/2012 bis 11/2015 **Studium Bachelor Chemie**
Technische Universität Bergakademie Freiberg
• Schwerpunkt Physikalische Chemie

Praktische Erfahrung

Seit 10/2017 **Institut für Angewandte Physik; TU Wien**
Projektassistent
Drittmittelanwerbung verschiedenen Industriepartner aus Metall- und Halbleiterindustrie
Betreuung von Studienarbeiten

06/2016 - 09/2016 **Institut für Physikalische Chemie I, II; TU Freiberg**
Praktikumsbetreuung, Konzipierung eines Praktikums

10/2015 - 11/2015 **Universitätsbibliothek Georgius Agricola; TU Freiberg**
Recherchearbeiten

Qualifikationen

Deutsch Muttersprache Englisch verhandlungssicher
Python (statistische) Datenauswertung und Darstellung
Origin Pro Darstellung wissenschaftlicher Daten

Publikationen

- „Viele Quellen anzapfen“ in: Nachrichten aus der Chemie Nr. 11/2015, S.1086-1088, **2015**.
- „Scratching resistance of SiC-rich nano-coatings produced by noble gas ion mixing“ in: Surface Coatings Technology, 386, 125475-1 – 125475-7, **2020**.
- „Adsorption and Diffusion Moderated by Polycationic Polymers during Electrode-position of Zinc“ in: ACS Applied Materials & Interfaces, 12, 26, 29928–29936, **2020**.
- „Photocorrosion of ZnO Single Crystals during Electrochemical Water Splitting“ in: ACS Applied Materials & Interfaces, 12, 46, 51530–51536, **2020**.

Wien, Juni 2021

Appendices

A.1 Electrochemistry of Zinc Oxide dissolution

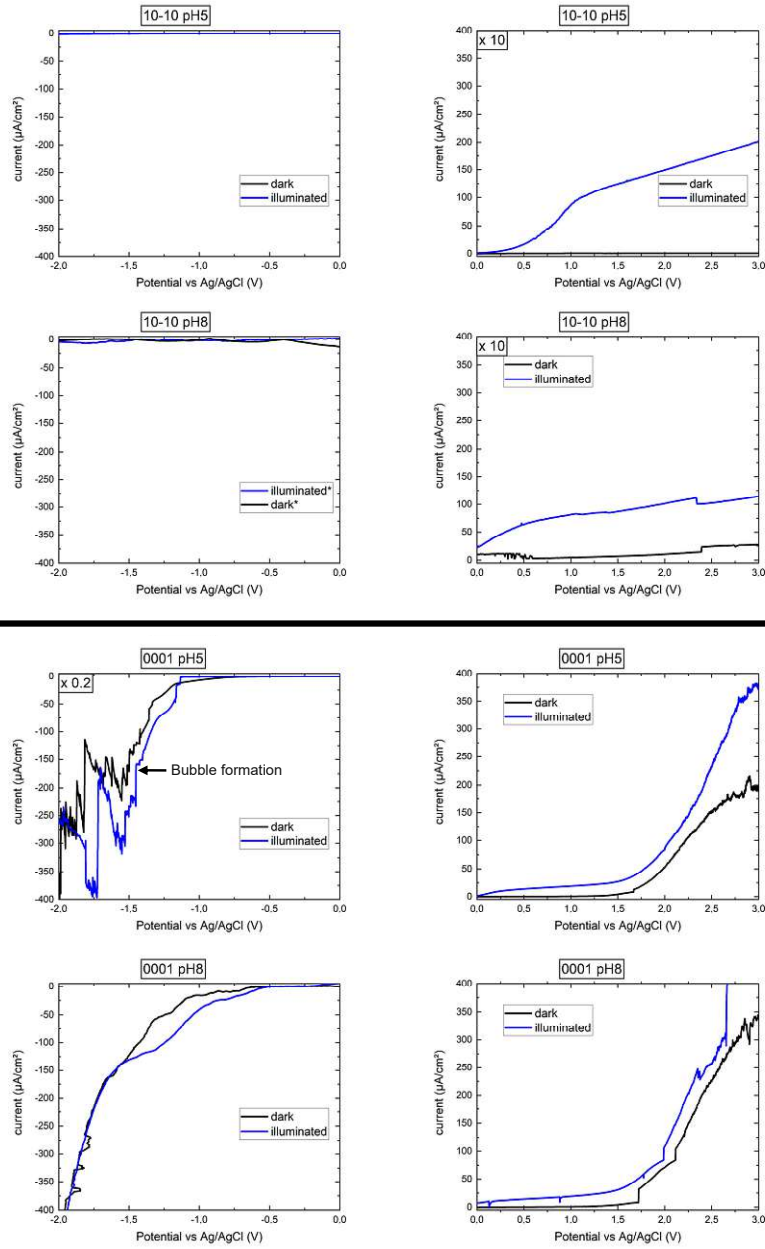


Figure A.1.2: Electric currents of experiments shown in Fig. 3.3 and 3.4. Currents marked with a star (*) were smoothed using a Savitzky-Golay-Filter.

A.2 Comparison of non-confined and restricted electrochemical degradation of Nickel Base Alloys

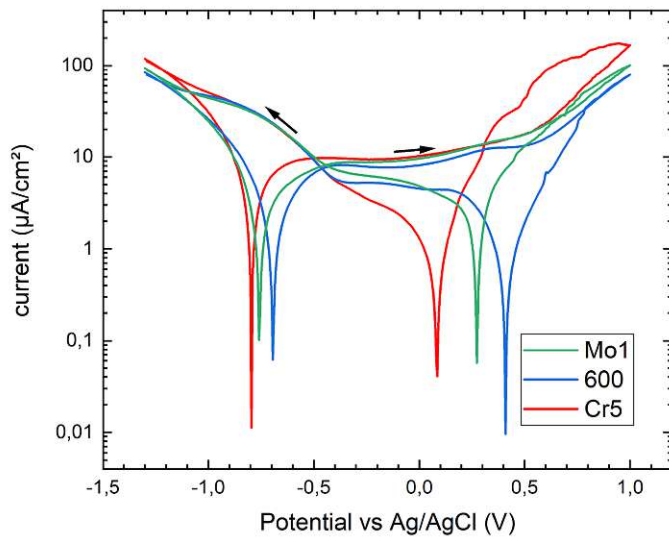


Figure A.2.1: Polarization curves recorded for all alloys used in 1 mM NaCl solution at 1 mV/s. During repassivation, at 0.2V which was used for ICP-MS studies as repassivation/preconditioning potential, all alloys are repassivated, with Cr5 showing the highest passive current. At transpassive conditions at 1V Cr5 shows the highest corrosion current, followed by Mo1 and alloy 600, which is in line with ICP-MS data (see main manuscript for details).

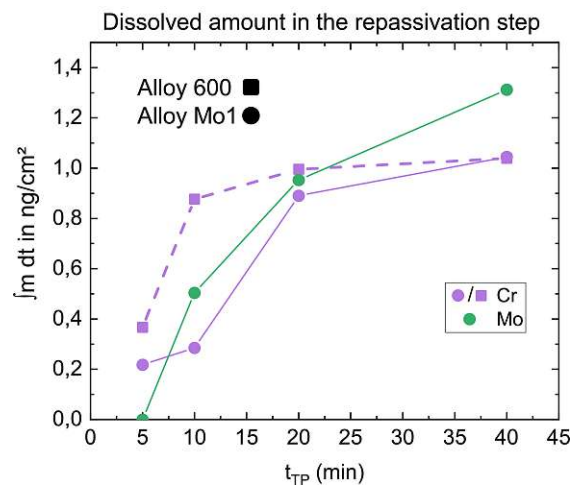


Figure A.2.2: Integrated mass release during repassivation as a function of increasing time during transpassive dissolution. The data is corrected for diffusion broadening, [92] and sums up material release during repassivation at 0.2V after 40 minutes of transpassive corrosion for alloy 600 (squares) and alloy Mo1 (points), respectively.

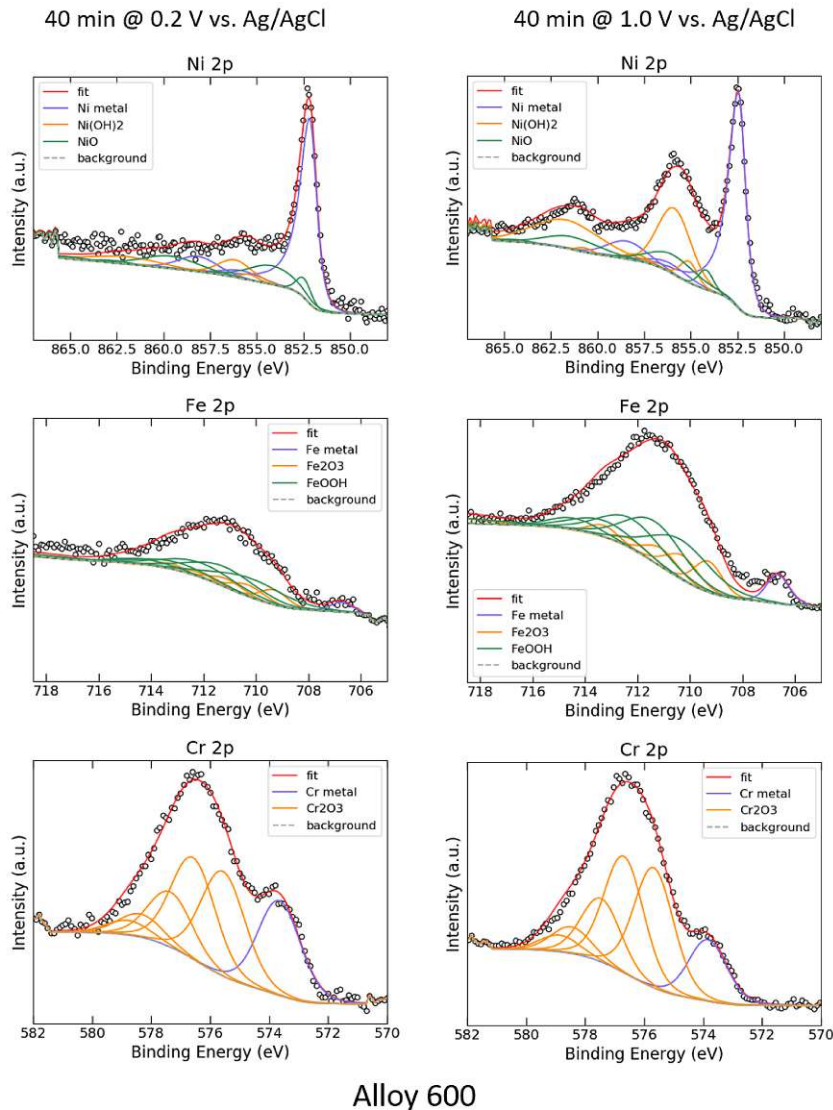


Figure A.2.3: XPS core level spectra of alloy 600 after passivation and repassivation. The data can be well fit using standard tabulated peak positions of reference materials (NIST database) and multiplet splitting as indicated and described in the methods section. Please note that spectra are shown in arbitrary units to enhance visibility of fittings, the quantitative peak analysis is summarized in the main part. (Left) Ni 2p, Fe 2p and Cr 2p spectra are shown after 40 minutes polarization under passive conditions at 0.2V. The nickel spectra show almost exclusively metallic signal, and only very small amounts of hydroxide and oxide were found. The iron spectrum indicates FeO(OH) and minor amounts of Fe₂O₃, and the chromium spectrum can be fit well with a metallic and a single component Cr₂O₃ component. (Right) Ni 2p, Fe 2p and Cr 2p spectra are shown after 40 minutes polarization under transpassive conditions at 1V. The nickel spectra indicate more hydroxide and oxide with respect to the metallic peak. The iron spectrum indicates FeO(OH) and minor amounts of Fe₂O₃, and the chromium spectrum can be fit well with a metallic and a single Cr₂O₃ component.

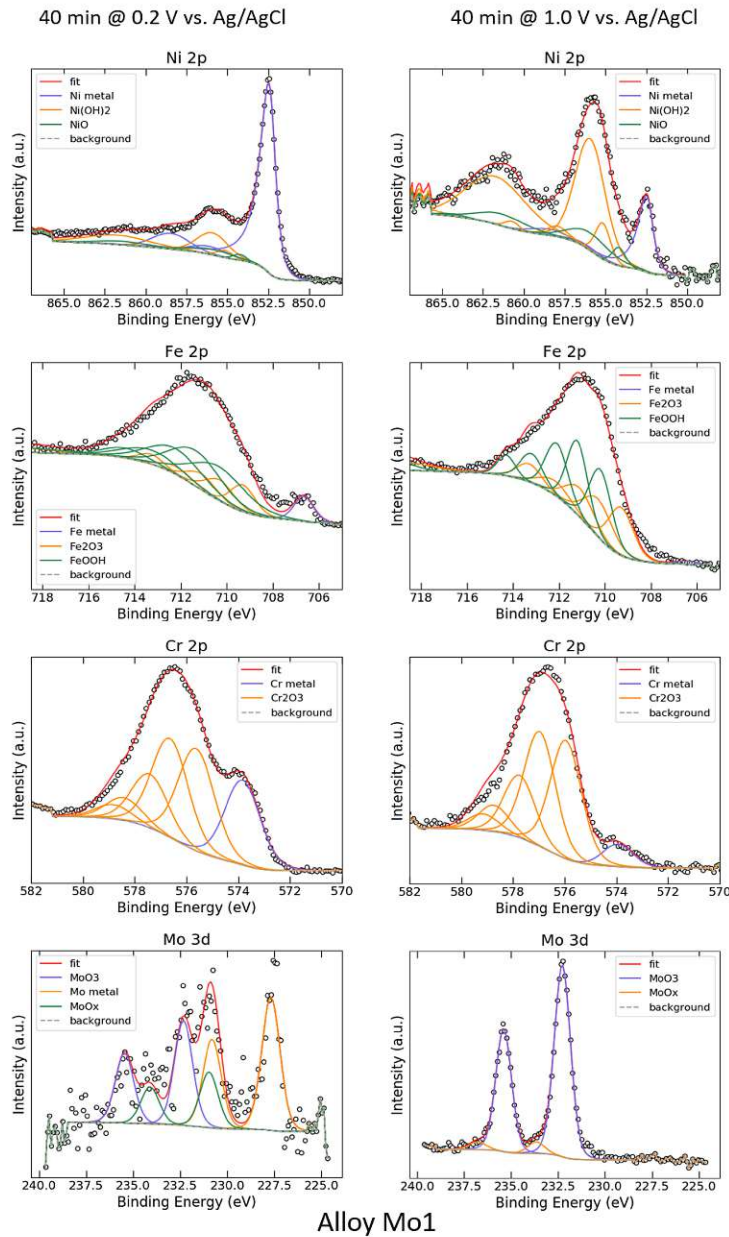


Figure A.2.4: XPS core level spectra of alloy Mo1 after passivation and repassivation. The data can be well fit using standard tabulated peak positions of reference materials (NIST database) and multiplet splitting as indicated and described in the methods section. Please note that spectra are shown in arbitrary units to enhance visibility of fittings, the quantitative peak analysis is summarized in the main part. (Left) Ni 2p, Fe 2p, Cr 2p and Mo 3d spectra are shown after 40 minutes polarization under passive conditions at 0.2V. The nickel spectra show a strong metallic signal, and only very small amounts of hydroxide and oxide were found. The iron spectrum indicates FeO(OH) and minor amounts of Fe₂O₃, and the chromium spectrum can be fit well with a metallic and a single component Cr₂O₃ component. Molybdenum spectra indicate a metallic, a Mo(IV) and a Mo(VI) component. (Right) Ni 2p, Fe 2p, Cr 2p and Mo 3d spectra are shown after 40 minutes polarization under transpassive conditions at 1V. The nickel spectra show a very weak metallic signal, and hydroxide and oxides were found. The iron spectrum indicates FeO(OH) and minor amounts of Fe₂O₃, and the chromium spectrum can be fit well with a weak metallic and a single Cr₂O₃ component. Molybdenum spectra indicate a strong Mo(VI) component and minor amounts of Mo at higher binding energies, which may correlate with molybdates.

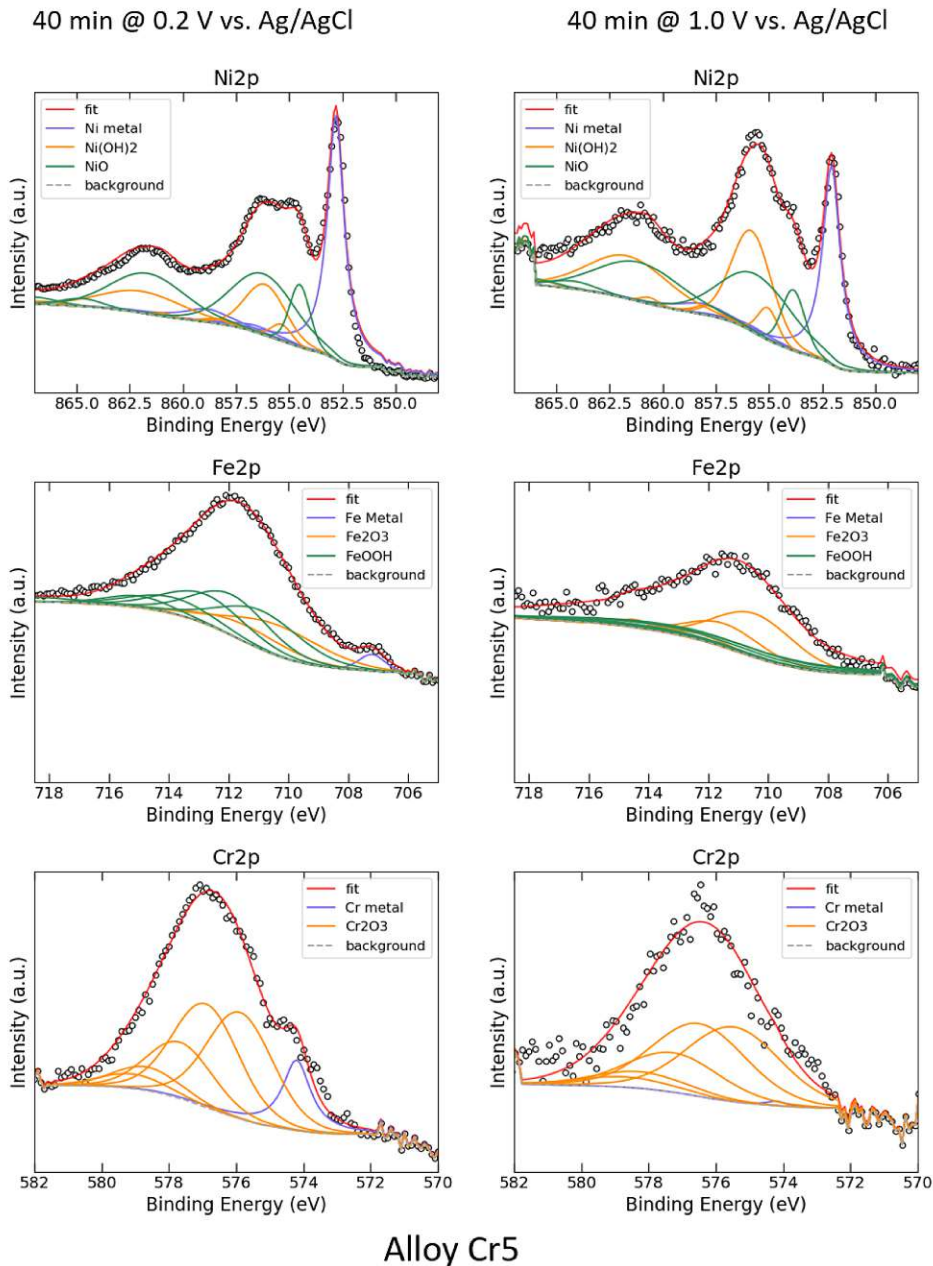


Figure A.2.5: XPS core level spectra of alloy Cr5 after passivation and repassivation. The data can be well fit using standard tabulated peak positions of reference materials (NIST database) and multiplet splitting as indicated and described in the methods section. Please note that spectra are shown in arbitrary units to enhance visibility of fittings, the quantitative peak analysis is summarized in the main part. (Left) Ni 2p, Fe 2p and Cr 2p spectra are shown after 40 minutes polarization under passive conditions at 0.2V. (Right) Ni 2p, Fe 2p and Cr 2p spectra are shown after 40 minutes of polarization under transpassive conditions at 1V.

40 min @ 1.0 V vs. Ag/AgCl
Bulk dissolved – **NBA 600**

40 min @ 1.0 V vs. Ag/AgCl
Crevice region – **NBA 600**

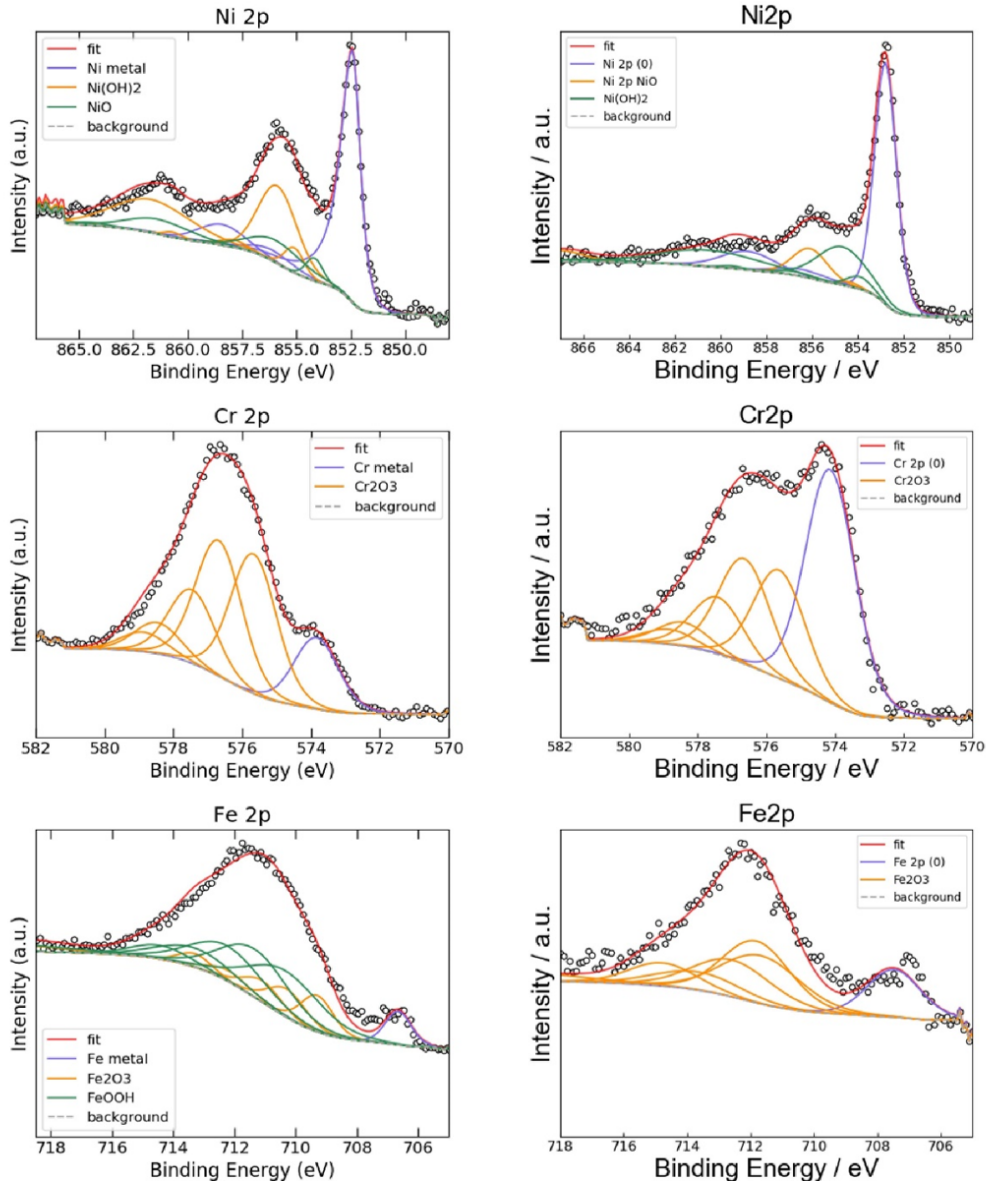


Figure A.2.6: XPS core level spectra of alloy 600 after 40 min of polarisation at 1.0 V vs Ag|AgCl. Comparison of the open area (left) and the crevice region (right).

40 min @ 1.0 V vs. Ag/AgCl
Bulk dissolved – NBA Mo1

40 min @ 1.0 V vs. Ag/AgCl
Crevice region – NBA Mo1

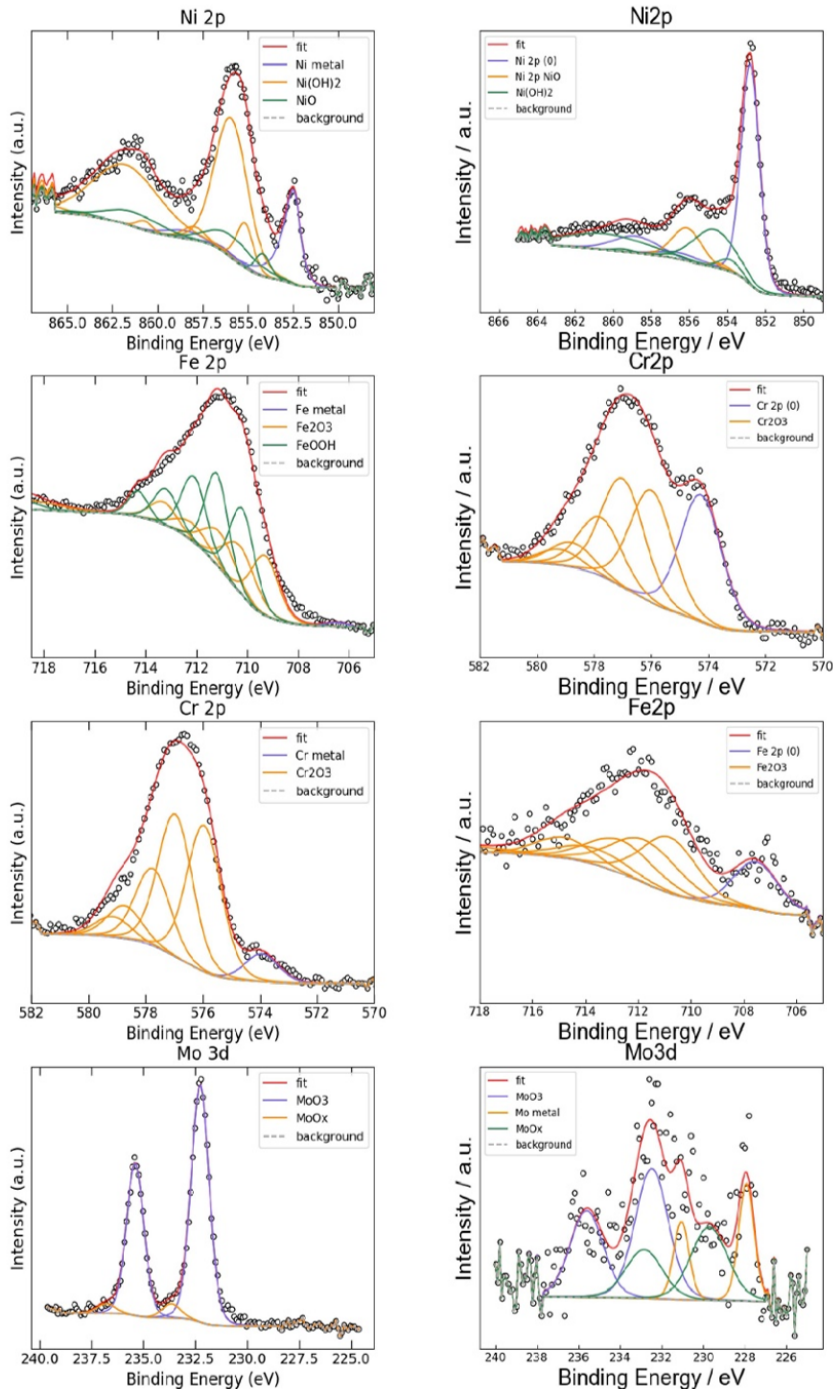


Figure A.2.7: XPS core level spectra of alloy Mo1 after 40 min of polarisation at 1.0 V vs Ag|AgCl. Comparison of the open area (left) and the crevice region (right).

A.3 Anodic dissolution of equimolar alloys of the system (Ni-Co-Cr-Fe-Mn)

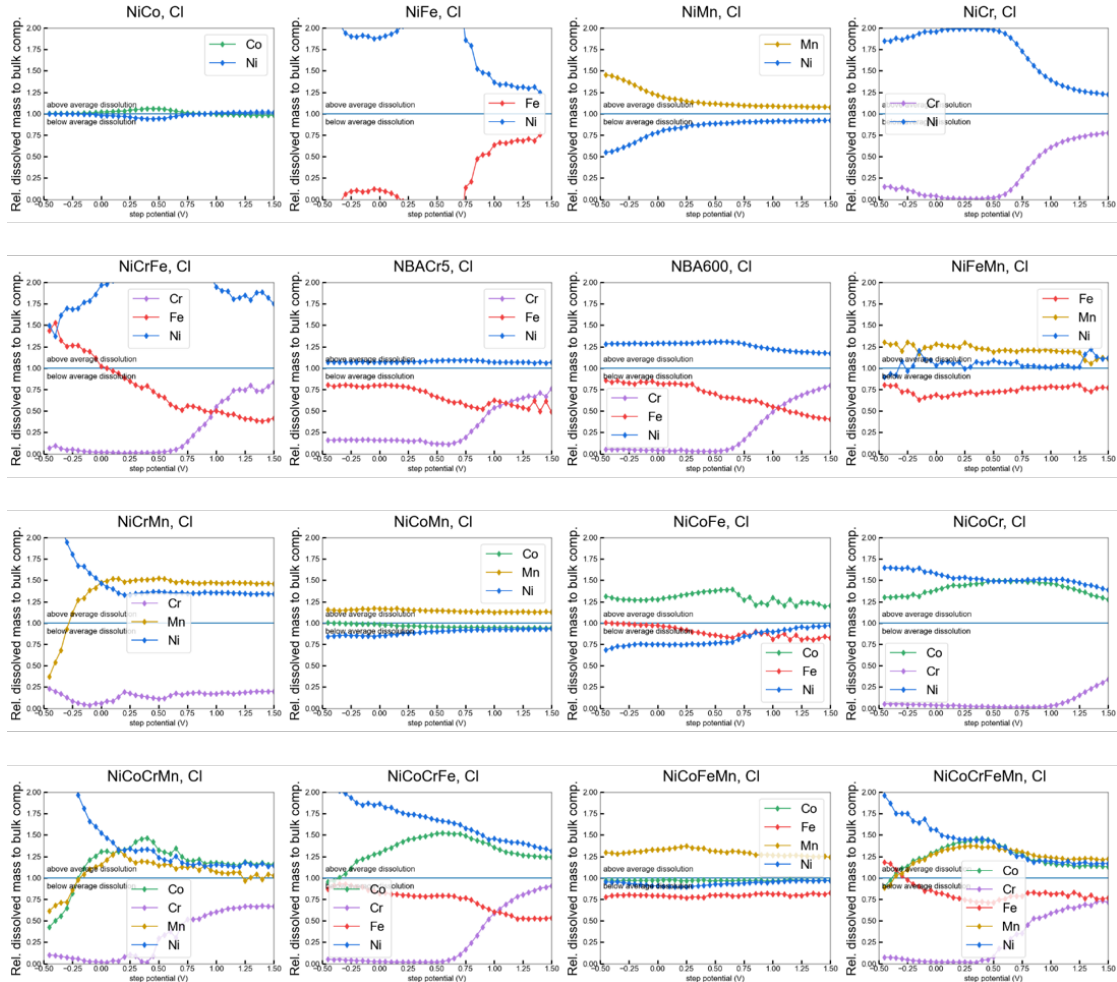


Figure A.3.1: Elemental dissolution ratios compared to bulk concentration for all alloys tested. Chromium Dissolution is for all alloys characterized by no dissolution at low potentials, onset of dissolution roughly around 0.5 V and a subsequent still underrepresented release to solution in respect to its bulk ratio. Nickel is in most of the cases above-average dissolved, with exceptions in NiMn, NiCoFe and NiCoMn. The binary alloys NiCo and NiMn dissolve mostly congruently.

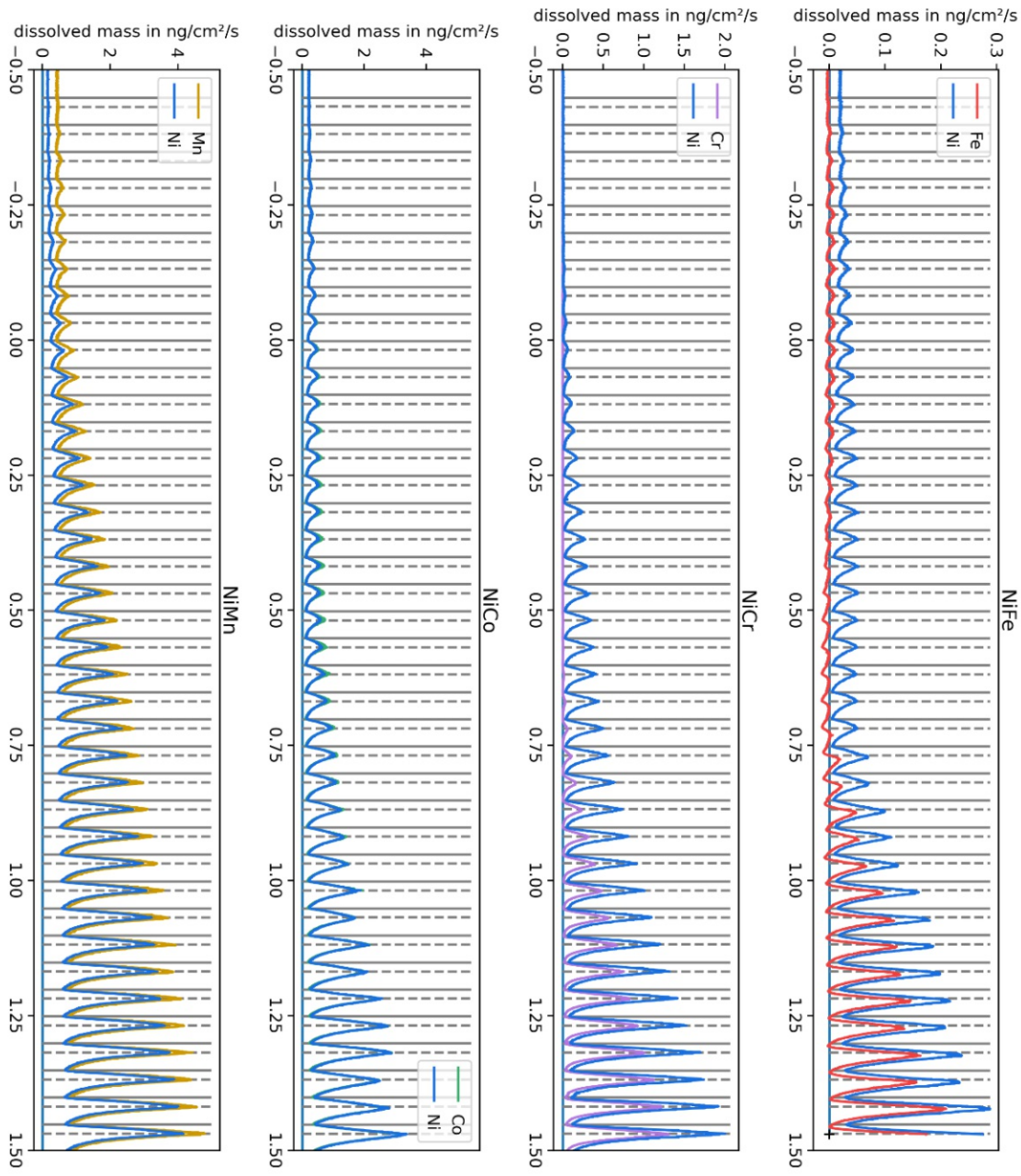
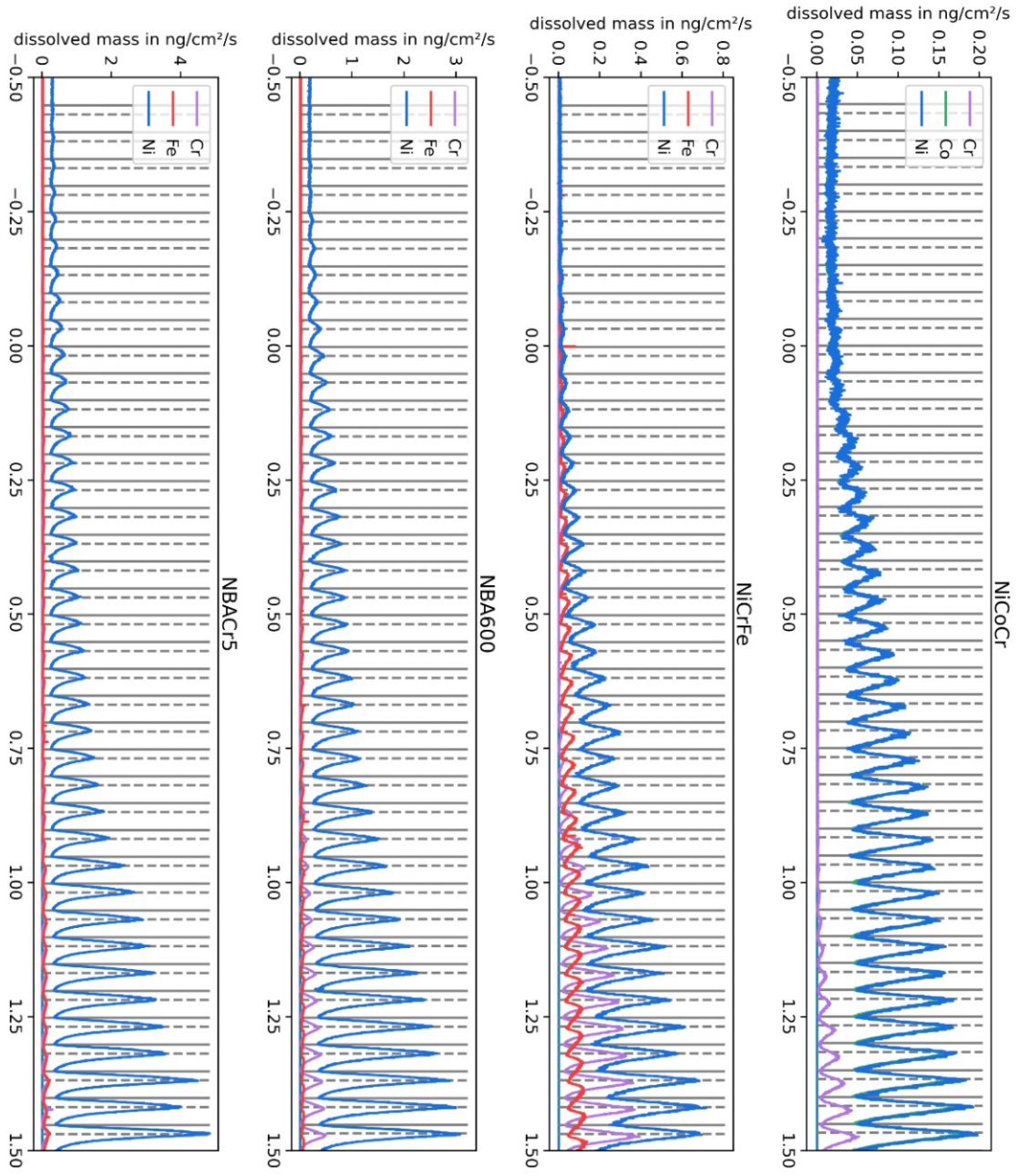
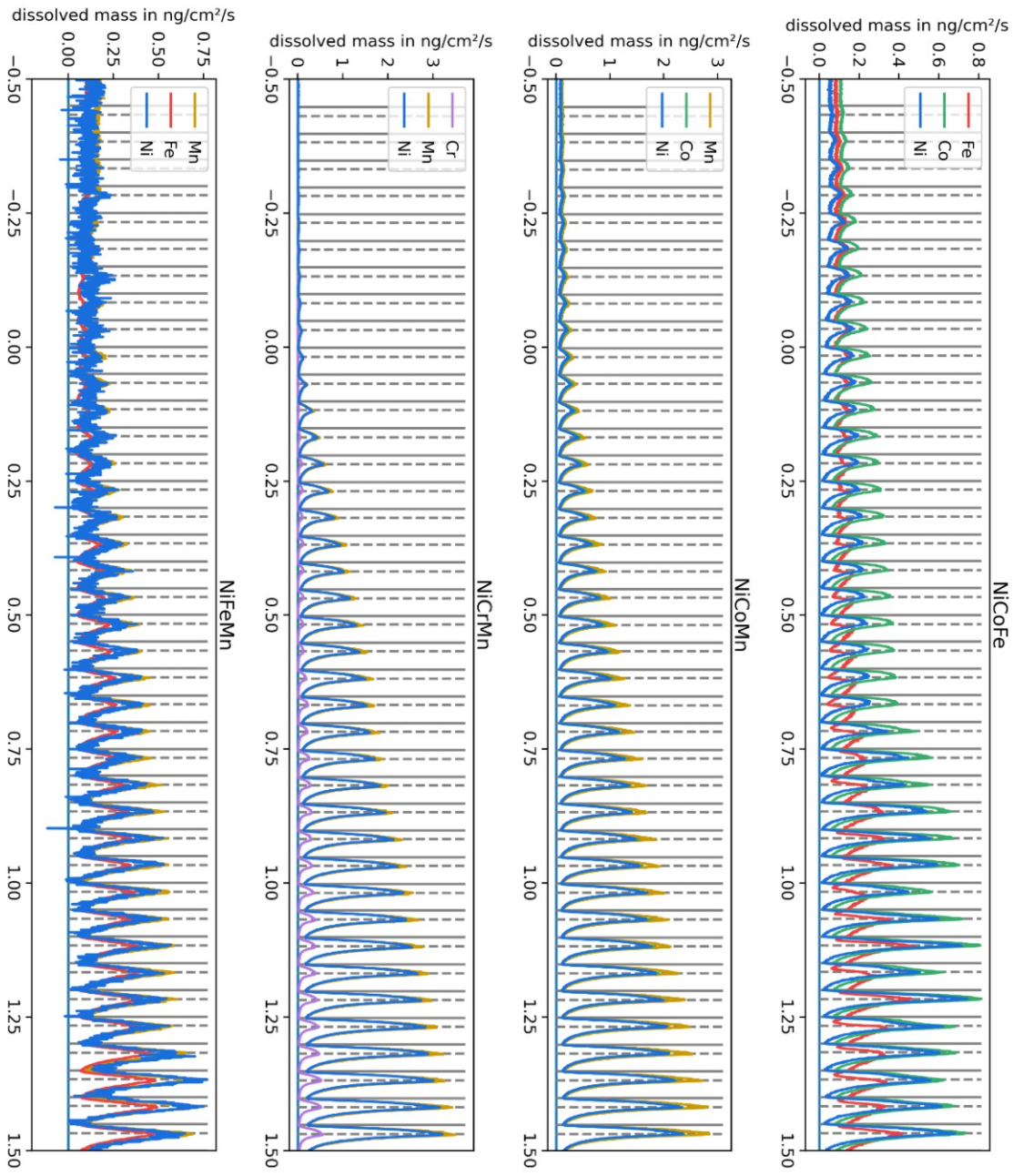


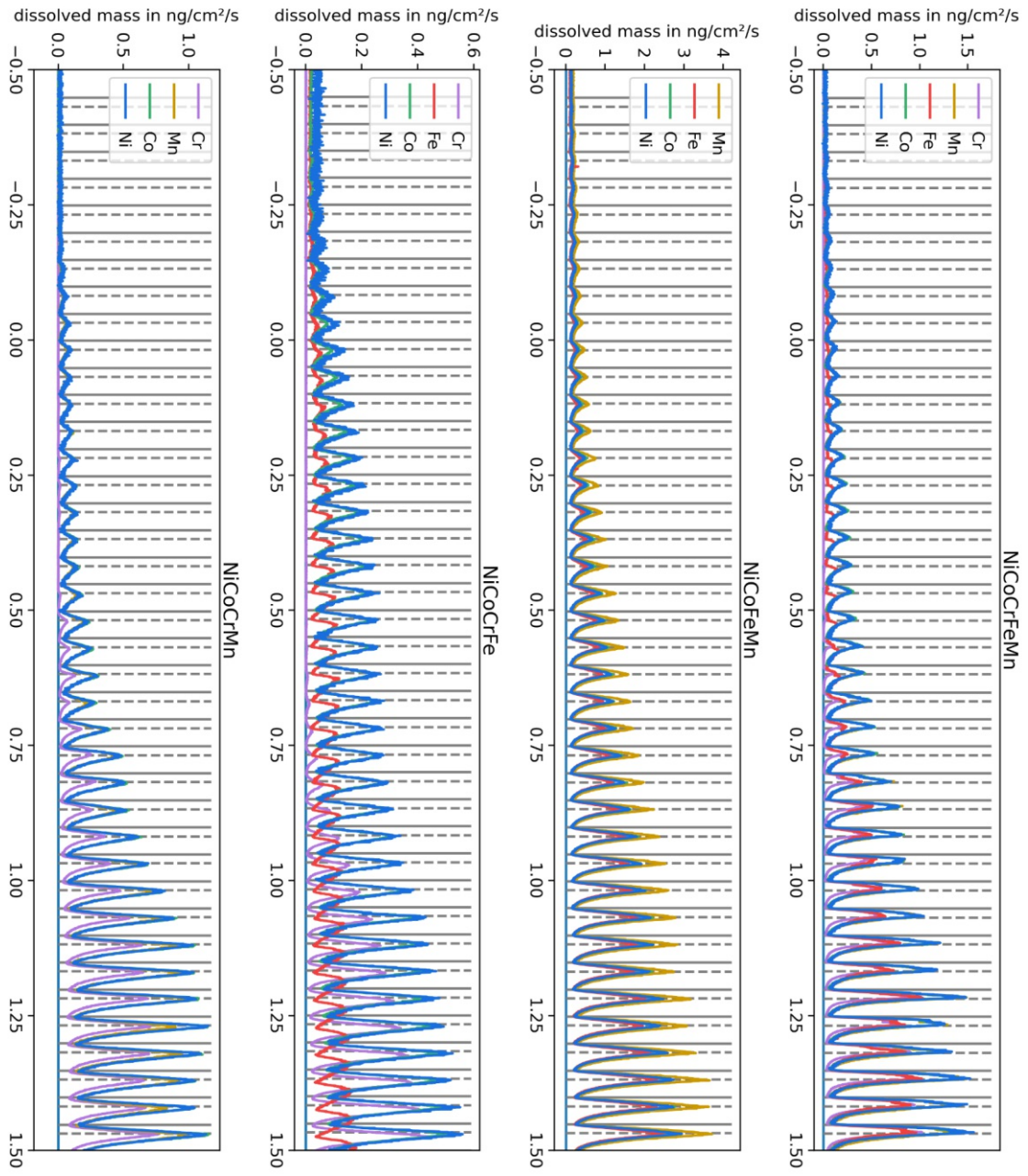
Figure A.3.1: Dissolution of alloys during NPV



Dissolution of alloys during NPV (cont.)



Dissolution of alloys during NPV (cont.)



Dissolution of alloys during NPV (cont.)

A.4 In-situ AFM of SAMs on gold during anodic polarisation

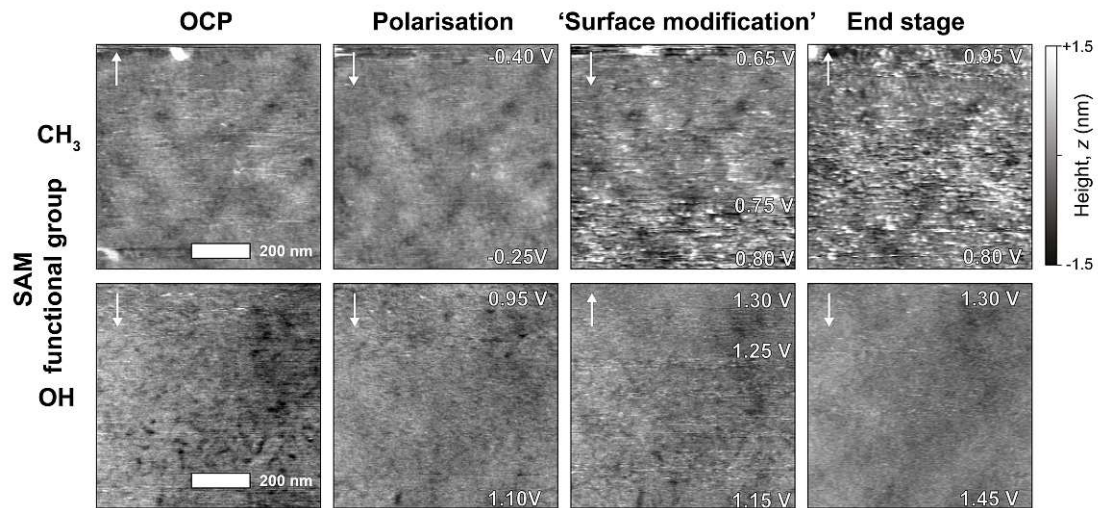


Figure A.4.1: Topographies of SAMs on Gold during different stages of the anodic polarisation experiment